

REPORT ON PROGRESS

Universal many-body response of heavy impurities coupled to a Fermi sea: a review of recent progress

To cite this article: Richard Schmidt *et al* 2018 *Rep. Prog. Phys.* **81** 024401

View the [article online](#) for updates and enhancements.

Related content

- [Polarons, dressed molecules and itinerant ferromagnetism in ultracold Fermi gases](#)
Pietro Massignan, Matteo Zaccanti and Georg M Bruun
- [Comparing and contrasting nuclei and cold atomic gases](#)
N T Zinner and A S Jensen
- [Recent developments in quantum Monte Carlo simulations with applications for cold gases](#)
Lode Pollet

Report on Progress

Universal many-body response of heavy impurities coupled to a Fermi sea: a review of recent progress

Richard Schmidt^{1,2,3} , Michael Knap⁴ , Dmitri A Ivanov^{5,6} ,
Jhih-Shih You¹, Marko Cetina^{7,8,9} and Eugene Demler¹

¹ Department of Physics, Harvard University, Cambridge MA 02138, United States of America

² ITAMP, Harvard-Smithsonian Center for Astrophysics, Cambridge, MA 02138, United States of America

³ Institute of Quantum Electronics, ETH Zürich, CH-8093 Zürich, Switzerland

⁴ Department of Physics, Walter Schottky Institute, and Institute for Advanced Study, Technical University of Munich, 85748 Garching, Germany

⁵ Institute for Theoretical Physics, ETH Zürich, 8093 Zürich, Switzerland

⁶ Department of Physics, University of Zürich, 8057 Zürich, Switzerland

⁷ Institut für Quantenoptik und Quanteninformation (IQOQI), Österreichische Akademie der Wissenschaften, 6020 Innsbruck, Austria

⁸ Institut für Experimentalphysik, Universität Innsbruck, 6020 Innsbruck, Austria

⁹ Joint Quantum Institute and University of Maryland Department of Physics, College Park, Maryland 20742, United States of America

E-mail: richard.schmidt@cfa.harvard.edu

Received 12 January 2017, revised 27 September 2017

Accepted for publication 24 October 2017

Published 5 January 2018



Corresponding Editor Professor Maciej Lewenstein

Abstract

In this report we discuss the dynamical response of heavy quantum impurities immersed in a Fermi gas at zero and at finite temperature. Studying both the frequency and the time domain allows one to identify interaction regimes that are characterized by distinct many-body dynamics. From this theoretical study a picture emerges in which impurity dynamics is universal on essentially all time scales, and where the high-frequency few-body response is related to the long-time dynamics of the Anderson orthogonality catastrophe by Tan relations. Our theoretical description relies on different and complementary approaches: functional determinants give an exact numerical solution for time- and frequency-resolved responses, bosonization provides accurate analytical expressions at low temperatures, and the theory of Toeplitz determinants allows one to analytically predict response up to high temperatures. Using these approaches we predict the thermal decoherence rate of the fermionic system and prove that within the considered model the fastest rate of long-time decoherence is given by $\gamma = \pi k_B T/4$. We show that Feshbach resonances in cold atomic systems give access to new interaction regimes where quantum effects can prevail even in the thermal regime of many-body dynamics. The key signature of this phenomenon is a crossover between different exponential decay rates of the real-time Ramsey signal. It is shown that the physics of the orthogonality catastrophe is experimentally observable up to temperatures $T/T_F \lesssim 0.2$ where it leaves its fingerprint in a power-law temperature dependence of thermal spectral weight and we review how this phenomenon is related to the physics of heavy ions in liquid ^3He and the formation of Fermi polarons. The presented results are in excellent agreement with recent

experiments on LiK mixtures, and we predict several new phenomena that can be tested using currently available experimental technology.

Keywords: quantum impurities, Feshbach resonances, Fermi gas, non-equilibrium dynamics, orthogonality catastrophe, functional determinants

(Some figures may appear in colour only in the online journal)

Contents

1. Introduction.....	2
1.1. Progress towards studying real-time impurity dynamics.....	3
1.2. Outline.....	4
2. Anderson–Fano model with ultracold atoms.....	5
2.1. Feshbach resonances.....	5
2.2. Interaction regimes.....	6
2.3. Anderson–Fano model.....	6
3. Dynamic many-body responses.....	7
3.1. Radio-frequency spectroscopy.....	7
3.1.1. ‘Standard’ RF spectroscopy.....	7
3.1.2. ‘Reverse’ RF spectroscopy.....	8
3.2. Real-time responses.....	8
3.2.1. Ramsey interferometry.....	8
3.2.2. Spin-echo interferometry.....	8
3.3. Functional determinant approach.....	8
4. Universal many-body response: radio-frequency spectra.....	9
4.1. Reverse RF spectra.....	9
4.1.1. From Fermi polarons to the orthogonality catastrophe.....	10
4.1.2. Single-particle interpretation.....	11
4.1.3. Comparison to experiments.....	13
4.2. Standard RF spectra.....	14
5. Universal many-body response: dephasing dynamics.....	14
5.1. Exact numerical solution.....	15
5.2. Analytical results.....	16
5.2.1. Excitation branches.....	16
5.2.2. Temperature independent contributions.....	16
5.2.3. Fermi-surface contributions.....	17
5.2.4. Bosonization.....	17
5.2.5. Toeplitz-determinant approach.....	20
5.3. Universal scaling relations.....	22
5.4. Comparison to experiments.....	22
6. Universal short-time, high-frequency response.....	24
6.1. RF response with finite initial and final state interactions.....	24
6.2. Analytical high-frequency response.....	24
6.2.1. Relation to the long-time evolution.....	25
7. Summary and outlook.....	25
Acknowledgments.....	26
Appendix A Exact single-particle wavefunctions in the two-channel model.....	26
Appendix B Relation between $\mathbf{S}(t)$ and $\mathbf{A}(\omega)$	27
Appendix C Fumi’s theorem.....	27
Appendix D. Technical details on bosonization.....	27
D.1. Fermi-surface contribution.....	27

D.2. Bottom-of-the-band and bound-state contributions.....	28
Appendix E. Asymptotic long-time response.....	29
E.1 Finite temperature.....	29
E.2. Zero temperature.....	30
Appendix F. Bi-exponential crossover.....	31
Appendix G. Subleading branches of Toeplitz determinants.....	31
References.....	32

1. Introduction

Exactly solvable models are a rare commodity in many-body physics [1]. Yet they provide a unique basis to develop a profound understanding of physical systems and can serve as a benchmark for approximate theoretical approaches. Examples include the Ising model [2], one-dimensional systems [3, 4], the Kitaev model [5, 6], or the Dicke model [7] which became paradigms of condensed matter physics and quantum optics.

Heavy impurities interacting with a Fermi gas are another paradigmatic example that is exactly solvable and yet retains the complexity of an interacting many-body system exhibiting rich physics [8, 9]. Most prominently it features the orthogonality catastrophe which defies a simple perturbative description and signals the absence of quasiparticles even at weak interactions, as first investigated by Anderson [10].

The Anderson orthogonality catastrophe manifests itself not only in ground state properties but also in the non-equilibrium dynamics. At long times, the power-law decay of coherence (for a definition see equation (10) and [11–13]) is one of its key manifestations which universally depends only on the scattering phase shift close to the Fermi surface. In contrast, the description of the short-time dynamics, being testament of the short-distance physics, suffers typically from the microscopic unknown. In particular in conventional solid-state systems physics depends on the details of chemical bonding, the core-hole potentials, as well as their screening and relaxation, which leads to highly non-universal short-time dynamics [14, 15].

Here we show that ultracold atoms provide a system where the physics of impurities is universal on essentially all time scales. This special property of cold atoms has its origin in their diluteness and ultra-low temperatures [16], which renders even the few-body physics universal [17]. Specifically, we propose the realization of an Anderson–Fano model [1] which is fully tunable by the use of Feshbach resonances [18].

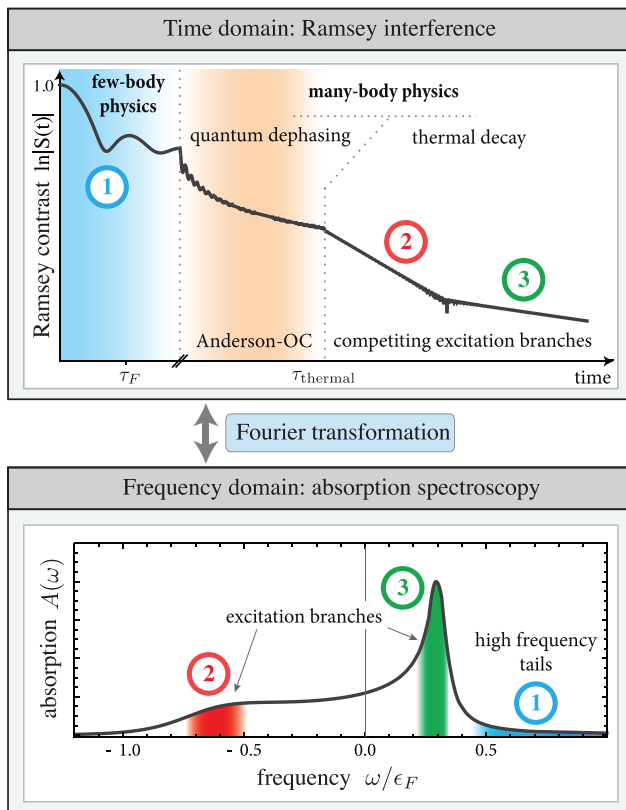


Figure 1. Illustration of universal impurity dynamics. The upper panel shows a sketch of the dephasing dynamics of a fermionic bath interacting with a single localized impurity as function of time. The corresponding many-body overlap $S(t)$, defined in equation (10), see also equation (41), can be measured in Ramsey spectroscopy. It is related by Fourier transformation to the absorption spectrum $A(\omega)$ of the impurity which hence contains equivalent physical information in the frequency domain (lower panel). The short-time dynamics, which is reflected in high-frequency tails of the absorption response, is dominated by few-body physics. At times exceeding the Fermi time scale $\tau_F = \hbar/\epsilon_F$ by $\tau_F = \hbar/\epsilon_F$, with the Fermi energy ϵ_F , many-body physics becomes relevant and the dynamics of the orthogonality catastrophe is manifest in a power-law decay of coherence. Beyond the thermal time scale $\tau_{\text{thermal}} = \hbar/k_B T$, exponential decay takes over. Even in this long-time regime, quantum effects can prevail. They lead to competing exponential decay rates that signal the superposition of various excitation branches visible in the absorption spectrum.

We introduce and review a functional determinant approach [19–22], that allows us not only to provide the exact numerical solution of its full non-equilibrium quench dynamics, but also to derive analytical expressions for the short- and long-time dynamics so that a complete analytical understanding of this paradigm model arises.

From this solution, an overarching picture of universality emerges, reaching from short to long time scales. The dynamics at short times is determined by universal tails of the impurity high-frequency response [23, 24]. Those tails are connected with the long-time dynamics by exact operator identities known as the Tan relations [25–28]. For the long-time, respectively low-frequency, response of the system we derive analytical expressions valid at arbitrary temperatures by a combination of the theory of Toeplitz determinants and bosonization. We find that the physics of impurities can be

universally described in terms of excitation branches which represent collections of relevant many-body states. By using this approach, even the non-equilibrium dynamics beyond the standard Luttinger liquid paradigm [4, 29] finds an analytical description.

Due to the low temperatures and diluteness of cold atomic gases, only short-range s-wave interactions are relevant. These can be tuned [18] and universal regimes reached that are not readily accessible in conventional solid state systems [30]. We identify various interaction regimes exhibiting distinct decoherence dynamics and spectral properties that can be related to dominant excitation branches. The main results are summarized in figure 1. Here we show an illustration of the time- and frequency-resolved response of the system following a quench of the impurity-Fermi-gas interaction. Experimentally the real-time dephasing signal $S(t)$ can be measured using an interferometric Ramsey scheme, while the frequency-resolved response $A(\omega)$ is accessible in absorption spectroscopy. Both signals are related by Fourier transformation and hence provide complementary probes of quantum many-body dynamics.

One finds various regimes of universal real-time dynamics. At ultrashort times dephasing is dominated by few-body physics leading to universal high-frequency tails in the absorption response [23, 24, 31, 32]. Intermediate time scales exhibit strong oscillations signifying the dressing of the impurity by excitations from the full depth of the Fermi sea. These oscillations are a robust and universal feature of short-range, strongly interacting impurity Fermi systems and they govern not only the dynamics of infinitely heavy impurities, but also appear in the case of impurities of finite mass where the dressing by bath excitations leads to the formation of polaronic quasiparticles [31, 32].

At longer times, the dynamics of heavy impurities is governed by the power-law dephasing of the Anderson orthogonality catastrophe which is universally dependent only on the phase shift at the Fermi surface. Even longer times are dominated by exponential decay due to finite temperature. Quite surprisingly, we find that even at times substantially exceeding the thermal time scale $\hbar/k_B T$, the quantum nature of excitation branches still persists. This is reflected in new features of competing dynamics where the robustness of superpositions of excitations branches leads to a crossover between characteristic exponential decays of coherence at very long times.

Remarkably, although there is an enormous scale separation between the many-body regime at long times and the intrinsic few-body short-time dynamics, both regimes are connected by the Tan relations [25–28]. We show that based on these exact relations one can relate the long-time phase evolution of the many-body wave function to the high-frequency tail of the absorption spectrum.

1.1. Progress towards studying real-time impurity dynamics

Recent years have seen an extensive interest in the Fermi polaron problem where one considers a single impurity immersed in a Fermi gas. Quite generally, the interaction between the impurity and the Fermi gas leads to the dressing of the impurity by excitations in the Fermi sea. When

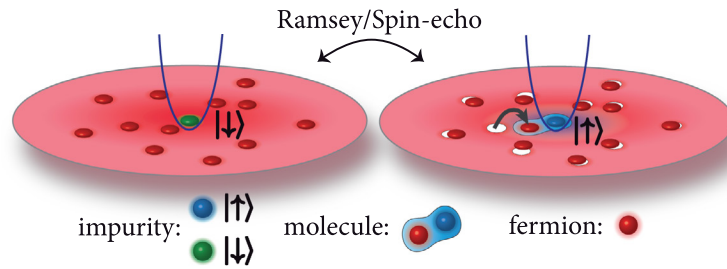


Figure 2. Schematic representation of the model. Left: an impurity atom in the $|\downarrow\rangle$ hyperfine state (green sphere) is decoupled from atoms in the Fermi sea (red spheres). Right: the impurity atom in the $|\uparrow\rangle$ hyperfine state (blue sphere) interacts with the Fermi sea atoms with a strength that is tunable by a Feshbach resonance. The impurity is either of infinite mass or, as illustrated, trapped in a state-dependent, strong, optical potential. When the impurity interacts with the Fermi gas it can bind with an atom from the Fermi sea and form a molecule. The internal hyperfine spin state is addressed using radio-frequency (RF) pulses in RF absorption spectroscopy or Ramsey and spin-echo interferometry.

the mass of the impurity is finite, this dressing by excitations remains quite moderate. In consequence, the new many-body ground state of the system—the ‘dressed impurity’—retains some resemblance to its non-interacting counterpart and one speaks of the formation of a well-defined quasiparticle: the Fermi polaron, characterized by a finite quasiparticle weight Z . In contrast, an infinitely heavy impurity is subject to a much stronger dressing by bath excitations. Here the dressing becomes even so extensive that the system is left in a state orthogonal to its original non-interacting state. Hence the dressed impurity completely loses its quasiparticle nature—its quasiparticle weight vanishes, $Z = 0$ —which signifies the hallmark of the Anderson orthogonality catastrophe [10].

The case of impurities of finite mass has been considered first in the context of the phase diagram of spin-imbalanced Fermi gases [33–37] where the Fermi polaron problem represents the extreme limit of spin imbalance. Special attention was given to the transition from a polaronic to a molecular ground state [37–46], which serves as a benchmark for theoretical approaches ranging from variational wave functions [33, 37, 40, 47], diagrammatic resummation [36, 48–51], $1/N$ expansions [52], quantum Monte Carlo calculations [34, 35], and functional renormalization group [53] to diagrammatic Monte Carlo calculations [38, 39, 54–56]. Using radio-frequency spectroscopy, the ground state properties of the Fermi polaron, including the polaron to molecule transition, were first observed by Schirotzek *et al* [57]; for an experimental study in two dimensions we refer to [58].

Shortly after these observations it was theoretically predicted that the impurity excitation spectrum contains a rich and interesting structure also above the ground state. In particular studies of the impurity spectral function revealed a metastable excitation at positive energies on the ‘repulsive’ side of the Feshbach resonance (i.e. at positive scattering length $a > 0$), separated by a large gap from the ground state [53, 59, 60]. Since this ‘repulsive polaron’ excitation can again be viewed as the extreme limit of a spin-imbalanced Fermi gas, its properties are of significance for studies of the repulsive Fermi gas and the question of a phase transition to itinerant Stoner ferromagnetism [61–66]. For a detailed discussion we refer the reader to the excellent review by Massignan *et al* [46].

The repulsive polaron was experimentally observed in three dimensions for the first time by Kohstall *et al* [67] and also in two-dimensional Fermi gases by Koschorreck *et al* [68] following its theoretical prediction [51, 69]. For a recent experimental study of repulsive polarons in a ${}^6\text{Li}$ Fermi gas using radio-frequency spectroscopy we refer to [70].

While the ground state and zero-temperature properties of Fermi polarons have received much theoretical attention, only recently the study of real-time dynamics of Fermi polarons came into reach of experimental techniques. First experimental steps towards the study of real-time dynamics were taken by Cetina *et al* [71], where the long-time impurity decoherence dynamics following an interaction quench was studied (the results of this work will be discussed in detail in section 5). Very recently, interferometric Ramsey techniques were used to experimentally observe the real-time formation of Fermi polarons for the first time [31]. In the work [31], the functional determinant approach, presented and reviewed in the present report, had been employed for a detailed description of the observed dephasing dynamics (for a detailed discussion of a variational approach to the problem see [32]). With these recent developments the stage it set for the experimental study of impurities in the heavy-mass limit where strong fluctuations lead to intriguing many-body dynamics accompanied by the complete disintegration of Fermi polarons.

It is this real-time dynamics of heavy impurities immersed in a Fermi gas that is at the center of this report. While developing the theoretical description, we will make connections to known results on the excitation spectrum of Fermi polarons wherever applicable. In this respect, this report serves not only to introduce new approaches to the dynamics of heavy impurities in Fermi gases as well as to highlight new directions in the study of such systems, but also to make the connection to previous theoretical work on ground and equilibrium properties of Fermi polarons.

1.2. Outline

The structure of this report builds on the observation that many aspects of the dynamics of impurities can be studied equivalently in the frequency or time domain. Experimentally, the

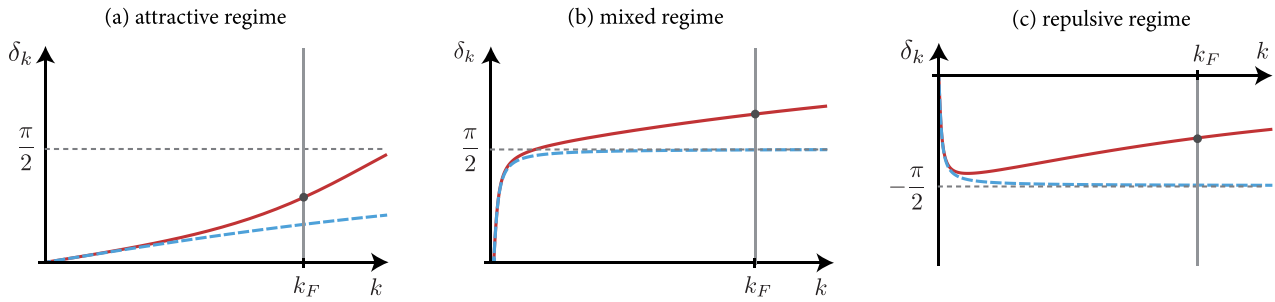


Figure 3. Interaction regimes and scattering phase shift. The figures show the momentum dependence of the scattering phase shift in the three interaction regimes. The various regimes are characterized by the scattering phase shift $\delta_F \equiv \delta_{k=k_F}$ evaluated at the Fermi momentum k_F . The attractive regime (a) is characterized by a negative scattering length $a < 0$ and a positive phase shift δ_F that does not exceed $\pi/2$. In the mixed regime (b) the scattering length remains negative while the positive phase shift at the Fermi surface δ_F exceeds $\pi/2$. The repulsive regime (c) obtains its name from the fact that here single-particle scattering states are shifted upwards in energy (see the detailed discussion in section 4). In this regime the scattering length $a > 0$ and a bound state exists in the single-particle spectrum. The existence of the bound state leads to a jump of the phase shift by π and we adapt the convention of choosing $\delta_k < 0$. Blue dashed lines correspond to a contact-interaction model with $k_F r^* = 0$ and red lines correspond to $k_F r^* = 0.8$. In the contact interaction model the mixed regime cannot be realized. The individual plots are shown for scattering lengths (a) $k_F a = -0.5$, (b) $k_F a = -100$, (c) $k_F a = 100$.

time-resolved impurity Green's function $S(t)$ can be measured using Ramsey interference, while its Fourier transform to the frequency domain $A(\omega)$ is accessible in absorption spectroscopy [31, 72, 73]. While both signals contain in principle the same information, their measurement can present different challenges to experiments. Also, their separate theoretical analysis gives insight to non-equilibrium impurity dynamics from different perspectives. Beyond that, time domain methods also allow one to study observables, such as the spin-echo signal, which have no analogue in frequency space and hence yield information about the many-body system not accessible by frequency-resolved methods. Following this route—after we introduce the two-channel scattering model describing the scattering in the vicinity of a Feshbach resonance and show its equivalence to the Fano–Anderson model in section 2—we introduce the dynamic response functions in the time and frequency domain in section 3.

The radio-frequency absorption response of the system is discussed in detail in section 4. We analyze its universal properties and develop a simple interpretation of spectral features in terms of a single-particle picture. This sets the basis to identify universal excitation branches pertinent for our discussion of the time-resolved response in section 5. Here we first provide a numerically exact solution of the non-equilibrium quench dynamics followed by the discussion of the relevant excitation branches. The identification of these branches allows us to derive analytical formulas for the universal asymptotic long-time dynamics based on bosonization and the theory of Toeplitz determinants. Finally, in section 6, we introduce the Tan relations which relate the long-time phase evolution of the impurity Green's function to high-frequency response. We summarize our findings and discuss future perspectives in section 7.

2. Anderson–Fano model with ultracold atoms

We study a low density of impurity atoms immersed into a Fermi gas of atoms of mass m . As illustrated in figure 2, two hyperfine states of the impurity atoms, which we refer to as $|\downarrow\rangle$

and $|\uparrow\rangle$, respectively, participate in the dynamics. These states are chosen such that only one of them interacts with the Fermi gas while the other does not. In the following, we consider impurities of an infinite mass which are localized in space. Experimentally, this can be achieved by using atomic species with a different polarizability so that only the impurities are trapped by an optical lattice or microtraps while the fermions in the bath remain mobile [16, 74–78].

2.1. Feshbach resonances

In ultracold atoms, the scattering of the bath atoms with the impurity is described by the s-wave scattering amplitude

$$f(k) = \frac{1}{k \cot \delta_k - ik} \approx \frac{1}{-1/a + \frac{1}{2}r_e k^2 - ik} \quad (1)$$

where k is the momentum of the incoming atom, and δ_k is the s-wave scattering phase shift. The second expression in equation (1) represents the effective range expansion of the phase shift which is valid for small scattering momenta k . Here a is the scattering length, and r_e is the so-called effective range. In the expansion also higher-order terms exist which are, however, typically negligible for ultracold atoms. Therefore, the two parameters a and r_e provide an accurate and universal description of the scattering physics [17].

It is one of the great appeals of ultracold gases that the scattering length a , and hence the interaction strength, can be tuned almost at will using Feshbach resonances [18]. Here one makes use of the coupling of the atoms in an open scattering channel to a molecular state in a closed channel, which is energetically accessible only by virtual processes. Due to its magnetic moment the energy $\epsilon_m(B)$ of the closed-channel molecule can be tuned with respect to the open channel by an external magnetic field B .

Depending on the relative detuning $\epsilon_m(B)$ from the scattering threshold at zero energy, the scattering length can be manipulated and at optimal detuning it diverges, $a \rightarrow \infty$, defining the Feshbach resonance. Close to the resonance, where the non-resonant (background) scattering in the open channel can

be neglected, the magnetic-field dependence of the scattering length can be parametrized as [18]

$$a(B) \approx -\frac{\hbar^2}{2\mu_{\text{red}}r^*\delta\mu(B-B_0)}. \quad (2)$$

Here, the reduced mass $\mu_{\text{red}} = mM/(m+M)$ becomes $\mu_{\text{red}} = m$ for the case of an impurity of mass $M = \infty$. Moreover, $\delta\mu$ is the differential magnetic moment of the closed-channel molecule, and B_0 denotes the magnetic field strength at which the scattering length diverges. Most importantly, equation (2) defines the range parameter $r^* > 0$ which determines the character of the Feshbach resonance.

To a good approximation, r^* is related to the effective range as [18]

$$r_e \approx -2r^*. \quad (3)$$

Therefore the range parameter r^* provides the second parameter r_e required to characterize the scattering properties of ultracold atoms to high accuracy. In the following we will use both r^* and r_e interchangeably to describe the momentum dependence of the scattering phase shift δ_k . Note that unlike the scattering length a , the range parameter r^* can typically not be tuned in a practical way [79–81], but is fixed by microscopic molecular details.

2.2. Interaction regimes

The range r^* influences the phase shift δ_k in equation (1) and thus can have a profound effect on the many-body physics. While for contact interactions, where $r^* = 0$, the phase shift is bounded by $|\delta_k| \leq \pi/2$, for finite r^* it can exceed $\pi/2$, see figure 3. This allows one to realize interaction regimes that are not accessible in simple contact-interaction models. The interaction regime are identified by phase shift $\delta_F \equiv \delta_{k=k_F}$ evaluated at the Fermi momentum k_F . One can distinguish three interaction regimes, see figure 3:

- (a) ‘attractive regime’: here $a < 0$ and the phase shift at the Fermi surface $0 < \delta_F < \pi/2$. In this regime the phase shift is positive for all energies, $\delta(E) \equiv \delta_{k=\sqrt{2mE}} > 0$. As discussed in section 4 the term ‘attractive’ is derived from the fact that single-particle scattering states are shifted to lower energies;
- (b) ‘mixed regime’: here $a < 0$ and $\pi/2 < \delta_F < \pi$. In this regime the phase shift is again positive for all energies, $\delta(E) > 0$. Within the two-channel model introduced below it is realized for negative inverse dimensionless scattering lengths $-k_F r^* < 1/k_F a < 0$;
- (c) ‘repulsive regime’: here $a > 0$ which in our convention for the scattering phase implies $\delta(E) < 0$ for all energies. As discussed in section 4 in this case single-particle scattering states are shifted to higher energies motivating the term ‘repulsive’ for this regime.

While the mixed regime (b) cannot be reached in a system with contact interactions, it is accessible in the Anderson–Fano model introduced below. Alternatively, the mixed regime can also be realized using pure open-channel scattering potentials.

Here, according to Levinson’s theorem [82], a phase shift $\delta_F > \pi/2$ is possible when more than one bound state is supported by the interaction potential. Note that the term ‘mixed’ is derived from the observation (discussed in section 4) that the many-body dynamics in this regime shares properties of both the attractive and repulsive regimes.

Following the classification of the various interaction regimes, one can use the value of $k_F r^*$ for a many-body characterization of Feshbach resonances. When $k_F r^* \ll 1$, one speaks of so-called ‘broad’ Feshbach resonance [16]. For those, the physics is universally parametrized by $k_F a$ alone, and Fermi gases close to such a resonance can be described by simple contact interaction models. For broad Feshbach resonances, the realization of the mixed regime requires very large, negative values of $k_F a$.

In contrast, for so-called ‘narrow’ Feshbach resonances, where $k_F r^* \gtrsim 1$, the mixed regime can be realized more easily. In this regime unique dynamics beyond the simple paradigm of contact interactions appears, and one has to employ models beyond contact interactions for their description.

2.3. Anderson–Fano model

In the following we develop a theory which describes the dynamical response of a Fermi gas coupled to an immobile impurity close to a Feshbach resonance of arbitrary ‘width’ as determined by $k_F r^*$. Theoretically, Feshbach resonances can be described with high accuracy by a two-channel model, where the interaction between atoms is mediated by the exchange of a closed-channel molecule [18, 83].

Specifically, for a bath of fermions interacting with a localized impurity, the system is described by the two-channel Hamiltonian

$$H_{2\text{-ch}} = -\int_{\mathbf{r}} \hat{\psi}^\dagger(\mathbf{r}) \frac{\hbar^2 \nabla^2}{2m} \hat{\psi}(\mathbf{r}) + \epsilon_m \hat{\phi}^\dagger \phi + g \int_{\mathbf{r}} \chi(\mathbf{r}) [\hat{\phi}^\dagger \hat{\psi}_\sigma \hat{\psi}(\mathbf{r}) + \text{h.c.}] \quad (4)$$

where the first term describes the free fermions of mass m with creation operators $\hat{\psi}^\dagger(\mathbf{r})$. The second term represents the closed-channel molecule created by $\hat{\phi}^\dagger$ with energy $\epsilon_m(B)$ detuned from the scattering threshold. Furthermore, the impurity, which is localized at $\mathbf{r} = 0$, is created by the operator $\hat{\psi}_\sigma^\dagger$ in the atomic spin state σ in which it interacts with the Fermi sea; see figure 2 where we have chosen $\sigma = \uparrow$.

Like the impurity, the molecule is immobile and hence the corresponding creation operators carry no coordinate dependence. Since their mass is infinite both molecule and impurity also have no kinetic energy term. Finally, the interaction of the impurity with the bath of fermions is described by the third term, where the impurity $\hat{\psi}_\sigma$ and a host atom $\hat{\psi}$ are converted into the molecular state $\hat{\phi}$. Here the form factor $\chi(\mathbf{r})$ determines the shape of the atom-to-molecule coupling and we choose $\chi(\mathbf{r}) = e^{-r/\rho}/4\pi\rho^2 r$ where the range ρ is determined by the van-der-Waals length [84, 85].

For an impurity of infinite mass the molecule creation and impurity annihilation operator can be combined to a new operator $\hat{m}^\dagger = \hat{\phi}^\dagger \hat{\psi}_\sigma$ which allows us to map the two-channel model onto the Fano–Anderson model

$$\hat{H} = \epsilon_m \hat{m}^\dagger \hat{m} + \sum_{\mathbf{k}} \epsilon_{\mathbf{k}} \hat{c}_{\mathbf{k}}^\dagger \hat{c}_{\mathbf{k}} + \frac{g}{\sqrt{V}} \sum_{\mathbf{k}} \chi_{\mathbf{k}} [\hat{m}^\dagger \hat{c}_{\mathbf{k}} + \text{h.c.}]. \quad (5)$$

Here the operators $\hat{c}_{\mathbf{k}}^\dagger$ are the creation operators of fermions with dispersion relation $\epsilon_{\mathbf{k}} = \hbar^2 \mathbf{k}^2 / 2m$ and $\chi_{\mathbf{k}}$ is the Fourier transform of the form factor $\chi(\mathbf{r})$. The Fano–Anderson model has been introduced in solid state physics to describe localized magnetic states in metals [86, 87]. It reappears here in the new context where it can be experimentally studied with the high control of ultracold atoms with tunable model parameters.

The parameters ϵ_m , g , and ρ of the model (5) can be deduced from the scattering properties. Calculating the scattering phase shift from the model (5) we can relate those parameters to experimentally accessible quantities which are the scattering length a , the range parameter r^* , and the van der Waals length l_{vdW} , which determines the range of the underlying atomic interaction potentials [88, 89]. Using the abbreviation $\bar{a} = 4\pi/\Gamma(1/4)^2 l_{\text{vdW}} \approx 0.956 l_{\text{vdW}}$ [18], one finds (for details see appendix A and [31, 84])

$$g^2 = \frac{\hbar^4 \pi}{\mu_{\text{red}}^2 r^{*2}}, \quad \epsilon_m = \frac{\hbar^2}{2\mu_{\text{red}} r^*} \left(\frac{1}{\bar{a}} - \frac{1}{a} \right), \quad \rho = \bar{a}/2. \quad (6)$$

Here we keep the effective mass μ_{red} explicit as these equations apply to arbitrary mass ratios between impurity and bath atoms; for the case of an immobile impurity $\mu_{\text{red}} = m$. Note that the first equation shows that the range parameter r^* controls the strength of the coupling of the atoms to the closed-channel molecule.

The following many-body calculation requires to find the single-particle solutions of Hamiltonian (5). Those are obtained from the ansatz $|\Psi\rangle = \alpha_m |m\rangle + |\psi\rangle$ which takes into account explicitly the molecular state $|m\rangle$ and solves the Schrödinger equation $\hat{H}|\Psi\rangle = E|\Psi\rangle$ [87]. Here α_m is a constant that determines the occupation of the closed-channel molecule $|m\rangle$, and $\psi(r) = \langle r|\psi\rangle = A \sin(kr + \delta_k)/r + B \chi(r)$ represents the open-channel scattering wave function. For the bound state we use the ansatz $A \sinh(\kappa(r-R))/r + B \chi(r)$ for the radial wave function where κ is the binding wave vector and R is the size of a spherical box R . From the solution of the Schrödinger equation we evaluate the unknown coefficients A , B , α_m . Next, we calculate the single-particle eigenenergies, determined through k and κ , from the boundary conditions of atoms being confined in the spherical box of size R . For details we refer to appendix A.

3. Dynamic many-body responses

Information about a many-body system can be obtained from response measurements in both the frequency and time domain. In ultracold atomic systems experimental tools exist to address both domains with high precision. While radio-frequency (RF) spectroscopy gives access to the spectrum

of a many-body Hamiltonian, Ramsey or spin-echo interferometry reveals information about the time-evolution of the many-body wave function. Using functional determinants one can solve numerically the response of the model (5) in both the frequency and time domain at arbitrary temperature without approximations. In this section we introduce some of the responses typically studied in cold atom experiments. These will then be investigated in more detail in the following sections.

3.1. Radio-frequency spectroscopy

Information about the spectrum, and in particular the ground state of the Anderson–Fano model (5), can be obtained experimentally from RF spectroscopy. In such an experiment the impurity is prepared in an initial spin state, $|\sigma\rangle$, where $\sigma \in \{\uparrow, \downarrow\}$. Using a weak RF signal, the spin is then driven into a final state $|\bar{\sigma}\rangle$, orthogonal to $|\sigma\rangle$. Theoretically, the RF signal can be modeled by a monochromatic perturbation $\sim e^{i\omega t} |\bar{\sigma}\rangle \langle \sigma| + \text{h.c.}$ of frequency ω . In linear response theory the absorption is given by Fermi’s golden rule ($\hbar = 1$)

$$A(\omega) = 2\pi\Omega^2 \sum_{i,f} w_i |\langle f|\hat{W}|i\rangle|^2 \delta[\omega - (E_f - E_i)], \quad (7)$$

where the transition operator $\hat{W} = |\bar{\sigma}\rangle \langle \sigma| + \text{h.c.}$ acts only on the spin state of the impurity. Furthermore, Ω is the Rabi frequency which determines the power of the applied RF field. In the following we set $\Omega = 1$. The sum in equation (7) extends over complete sets of initial $|i\rangle$ and final many-body states $|f\rangle$ with energies E_i and E_f . The weights w_i are determined by the initial state density matrix as $w_i = \langle i|\hat{\rho}_i|i\rangle$.

The measured RF signal depends on the specific initial and final states chosen and in the following we will focus on two scenarios. In the ‘*standard RF*’ scheme, the system is driven from the spin state, in which the impurity interacts with the Fermi sea, to a non-interacting spin state. In contrast, in the ‘*reverse RF*’ procedure the impurity is initially in a non-interacting state and then driven to an interacting one [53]. In this section we formally define the two schemes, while their distinct responses are discussed in detail in section 4.

3.1.1. ‘Standard’ RF spectroscopy. In the standard RF scheme, the impurity is prepared in the state $|\uparrow\rangle$ in which it interacts with the Fermi sea. At $T = 0$ the fermions are initially in the many-body ground state $|\psi_{\text{GS}}\rangle$ of the Hamiltonian (5), i.e. $\hat{H}|\psi_{\text{GS}}\rangle = E_{\text{GS}}|\psi_{\text{GS}}\rangle$, where they experience the impurity as a scattering center at $\mathbf{r} = 0$. The initial state, including the impurity state, is then given by $|i\rangle = |\uparrow\rangle \otimes |\psi_{\text{GS}}\rangle$. At finite temperature the fermionic initial ‘state’ is determined by the thermal density matrix $\hat{\rho}_{\text{GS}} \equiv e^{-\beta(\hat{H} - \mu\hat{N})} / Z_{\text{GS}}$, with $\beta = 1/k_{\text{B}}T$ the inverse temperature with k_{B} the Boltzmann constant, which we set to one in the following, \hat{N} is the fermion number, μ their chemical potential, Z_{GS} the partition sum, and \hat{H} is given by equation (5).

In the final state the impurity is in the spin state $|\downarrow\rangle$ which is non-interacting with the Fermi gas. Since then the scattering

center is absent, the system is described by the Hamiltonian \hat{H}_0 , defined by equation (5) with $g = 0$. The sum over the systems' final states can be written in terms of the states $|f\rangle = |\downarrow\rangle \otimes |\psi_n\rangle$ where $|\psi_n\rangle$ denotes the complete set of many-body fermionic eigenstates of \hat{H}_0 , $\hat{H}_0|\psi_n\rangle = E_n^0|\psi_n\rangle$, i.e. $E_f \equiv E_n^0$ in equation (7). Using these definitions and transforming equation (7) to the time domain (for details see appendix B), one arrives at the expression for the 'standard RF absorption spectrum'

$$R(\omega) = 2\text{Re} \int_0^\infty dt e^{i\omega t} \text{Tr}[e^{i\hat{H}t} e^{-i\hat{H}_0 t} \hat{\rho}_{\text{GS}}], \quad (8)$$

which solely contains operators in the fermionic Hilbert space.

The standard RF response of an impurity immersed in a Fermi gas has been measured by Schirotzek *et al* [57]. In this case the impurity was mobile and the ground state of the system $|\psi_{\text{GS}}\rangle \rightarrow |\psi_{\text{pol}}\rangle$ is a well-defined quasiparticle, the Fermi polaron. The Fermi polaron is a well-defined quasiparticle since its state has a finite overlap with the non-interacting ground state $|\psi_0\rangle$ of the system, which defines the quasiparticle weight $Z = |\langle\psi_0|\psi_{\text{pol}}\rangle|^2 > 0$. This is different for an infinitely heavy impurity at zero temperature. In this case the overlap of the interacting ground state $|\psi_{\text{GS}}\rangle$ with the non-interacting ground state vanishes, i.e. $Z = |\langle\psi_0|\psi_{\text{GS}}\rangle|^2 \equiv 0$. Hence no quasiparticle exists in this case, giving rise to the term 'orthogonality catastrophe' (OC) [10]. The relation between the Anderson OC and Fermi polarons will be discussed in more detail in the following section 4.

3.1.2. 'Reverse' RF spectroscopy. In the 'reverse' RF scheme, sometimes also called the 'spin-injection' scheme [90], the role of interactions are reversed. Here the impurity in its initial atomic state $|\downarrow\rangle$ is not interacting with the Fermi gas. Hence, at $T = 0$, the fermions build a perfect free Fermi sea [FS] by filling up all single-particle eigenstates of the non-interacting Hamiltonian \hat{H}_0 up to the Fermi energy ϵ_F . The initial state is then given by $|i\rangle = |\downarrow\rangle \otimes |\text{FS}\rangle$. At finite temperature T , [FS] is replaced by the thermal density matrix $\hat{\rho}_{\text{FS}} = e^{-\beta(\hat{H}_0 - \mu\hat{N})}/Z_{\text{FS}}$ of a free Fermi gas.

The impurity is then driven into its final state $|\uparrow\rangle$ in which the impurity is interacting with the gas. In that state, the dynamics of the fermions is described by the Hamiltonian \hat{H} where the scattering center at $\mathbf{r} = 0$ is present; i.e. $g > 0$ in equation (5). The final states in equation (7) are then given by $|f\rangle = |\uparrow\rangle \otimes |\psi_\alpha\rangle$, where the fermionic states are defined by $\hat{H}|\psi_\alpha\rangle = E_\alpha|\psi_\alpha\rangle$. Note that we set the energy splitting between hyperfine levels to zero. Basic manipulations (for details see appendix B) lead to the reverse RF response

$$A(\omega) = 2\text{Re} \int_0^\infty dt e^{i\omega t} \text{Tr}[e^{i\hat{H}_0 t} e^{-i\hat{H} t} \hat{\rho}_{\text{FS}}]. \quad (9)$$

The reverse RF scheme had been implemented for the observation of the full impurity spectral function by Kohstall *et al* [67], and found multiple applications in the observation of polaronic physics with ultracold atoms [31, 58, 67, 70, 91–94].

3.2. Real-time responses

Information about the many-body dynamics can also be obtained from real-time observables. Here we give two examples for real-time responses, namely Ramsey and spin-echo interferometry [73, 95].

3.2.1. Ramsey interferometry. In many-body Ramsey interferometry, the impurity is initially prepared in a non-interacting spin state $|\downarrow\rangle$. Then using a $\pi/2$ rotation a superposition of the two impurity states, $(|\downarrow\rangle + |\uparrow\rangle)/\sqrt{2}$ is prepared, where in the state $|\uparrow\rangle$ the impurity interacts with the Fermi gas. After a finite interaction time t a second $\pi/2$ pulse with variable phase φ is applied. Measuring $\hat{\sigma}_z$ then yields the Ramsey signal $S(t)$ [71, 73]. Throughout this work we assume infinitely fast $\pi/2$ rotations that leave the Fermi sea unperturbed. While the implementation is experimentally challenging directly in the strongly interacting regime, it has been shown [31] that such protocols can indeed be realized by quenching interactions using the optical resonance shifting technique developed in [71]. A straightforward calculation shows that the Ramsey signal is given by

$$S(t) = \langle e^{i\hat{H}_0 t} e^{-i\hat{H} t} \rangle \equiv \text{Tr}[e^{i\hat{H}_0 t} e^{-i\hat{H} t} \hat{\rho}_{\text{FS}}]. \quad (10)$$

From this expression it is evident that the reverse RF absorption signal equation (9) is determined by the Fourier transform of the Ramsey signal. Hence both signals contain the same physical information and can be used as complementary experimental tools (for more details see appendix B).

3.2.2. Spin-echo interferometry. In addition to the Ramsey response, more complicated interferometric protocols can be chosen which do not have simple conjugate observables in the frequency domain. One example is spin-echo interferometry, which defines a more involved spin trajectory by augmenting the Ramsey sequence by an additional instantaneous spin-flip at half of the evolution time. This leads to the expression [73]

$$S_{\text{SE}}(t) = \langle e^{i\hat{H}_0 t/2} e^{i\hat{H} t/2} e^{-i\hat{H}_0 t/2} e^{-i\hat{H} t/2} \rangle. \quad (11)$$

In typical applications in the context of nuclear magnetic resonance (NMR) spectroscopy such protocols are employed to echo-out external, quasi-static perturbations. However, such protocols can also yield additional information about the system dynamics and we will contrast the spin-echo and Ramsey response in the thermal and quantum regimes in section 5.

3.3. Functional determinant approach

In order to calculate the absorption spectra $A(\omega)$ and the time-dependent many-body response such as the Ramsey and spin-echo signal, we use the functional determinant approach (FDA) [19–21]. The FDA provides an exact numerical solution for systems which are described by fermionic bilinear Hamiltonians. Extensions to bosonic systems are possible [20] and have been recently employed for the description of Rydberg impurity systems [93, 94, 97]. The FDA reduces expectation values of many-body operators to determinants in single-particle Hilbert space by virtue of the formula

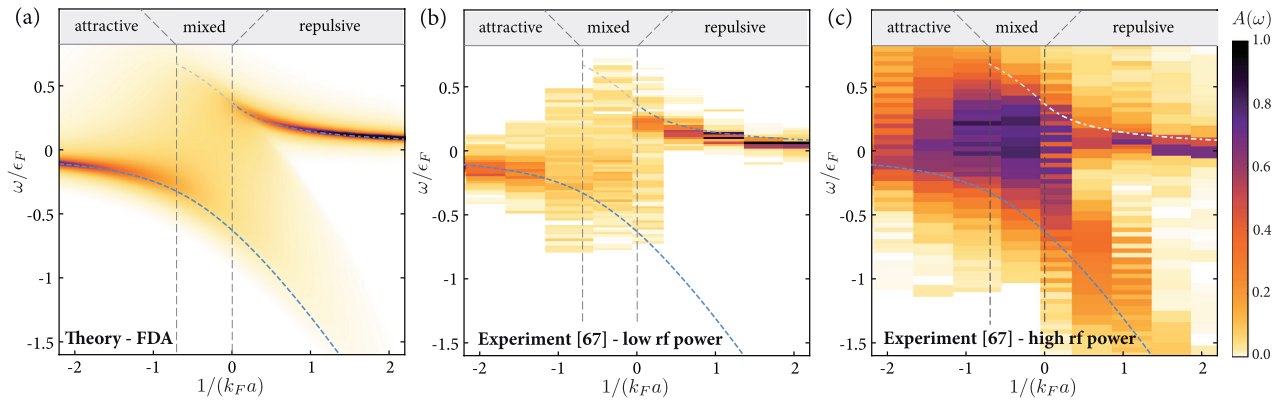


Figure 4. Finite temperature RF absorption spectra – theory and experiment [67]. (a) Reverse RF absorption spectrum $A(\omega)$ as function of frequency ω/ϵ_F and inverse interaction strength $1/k_F a$ in the ‘attractive’, ‘mixed’, and ‘repulsive’ interaction regime as obtained from an FDA calculation (throughout this work absorption spectra $A(\omega)$ are shown in units of ϵ_F). The temperature $T/T_F = 0.16$ and range parameter $k_{FR}^* = 0.71$ are chosen as in the experiment by Kohstall *et al* [67]. Their experimental results are shown for comparison: in (b) for a weak RF drive and (c) for a strong RF drive which saturated the signal and hence was beyond linear response. The dashed and dot-dashed lines, shown in ((a)–(c)) correspond to the energy of the onset of the attractive and repulsive excitation branch. They are calculated from Fumi’s theorem [96] which relates the sum over phase shifts to the ground state energy of the system, see also [1, 36, 60] and appendix C.

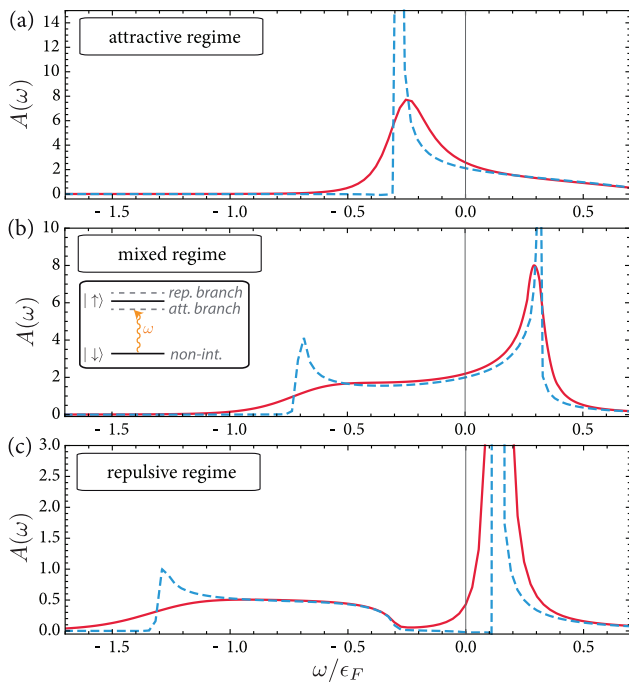


Figure 5. Finite temperature radio-frequency absorption spectra. RF response in the reverse scheme where the impurity is initially in a hyperfine state non-interacting with the Fermi gas and driven to a state interacting with the gas (see inset in (b) for an illustration). The spectra are shown for temperatures $T/T_F = (0.01, 0.16)$ (dashed, solid), for interaction strengths $1/k_F a = (-0.91, -0.1, 1.0)$ ranging from the attractive to the repulsive side of the Feshbach resonance, and for a fixed Feshbach range parameter $k_{FR}^* = 0.71$. For $T/T_F = 0$ the spectral onset of features will be replaced by sharp edges.

$$\langle e^{\hat{Y}_1} \dots e^{\hat{Y}_N} \rangle = \det[1 - \hat{n} + \hat{n} e^{\hat{Y}_1} \dots e^{\hat{Y}_N}]. \quad (12)$$

Here \hat{Y}_i are arbitrary, fermionic, bilinear many-body operators and \hat{y}_i their single-particle representatives. Furthermore, \hat{n} denotes the single-particle occupation number operator. The

identity (12) allows us to solve the time-dependent many-body problem exactly by using the analytical solutions for the single-particle states obtained for the model equation (5), see appendix A.

4. Universal many-body response: radio-frequency spectra

We now turn to RF absorption spectra. Our results are obtained by evaluating equation (8) and (9) using the FDA. While there has been much theoretical effort to predict the properties of impurities immersed in Fermi gases at zero temperature using approximate techniques [32–40, 46, 49–51, 53–55, 59, 60, 69, 98–124], our calculations are to our knowledge the first to predict corresponding spectra at arbitrary temperature, which are exact in the limit of infinitely heavy impurities (for comparison to recent ultracold atom experiments see also [31]). Studying the frequency resolved response provides insight about the relevant many-body states and allows us to identify the excitation branches which will become of importance in finding the analytical solution of the many-body dynamics in section 5.

In this section, we focus mostly on the low-frequency response which is universally determined by the scattering phase shift close to the Fermi surface. The high-frequency response is discussed in more detail in section 6.

4.1. Reverse RF spectra

First we consider the reverse RF absorption spectrum, where the system is initially prepared in the non-interacting impurity spin state and then driven into an interacting final state. In the reverse RF scheme the measured response is identical to the impurity spectral function [31, 32, 53, 67] and as such it reveals the spectrum of the Hamiltonian (5). In figure 4(a) we show a density plot of the predicted absorption spectrum as a

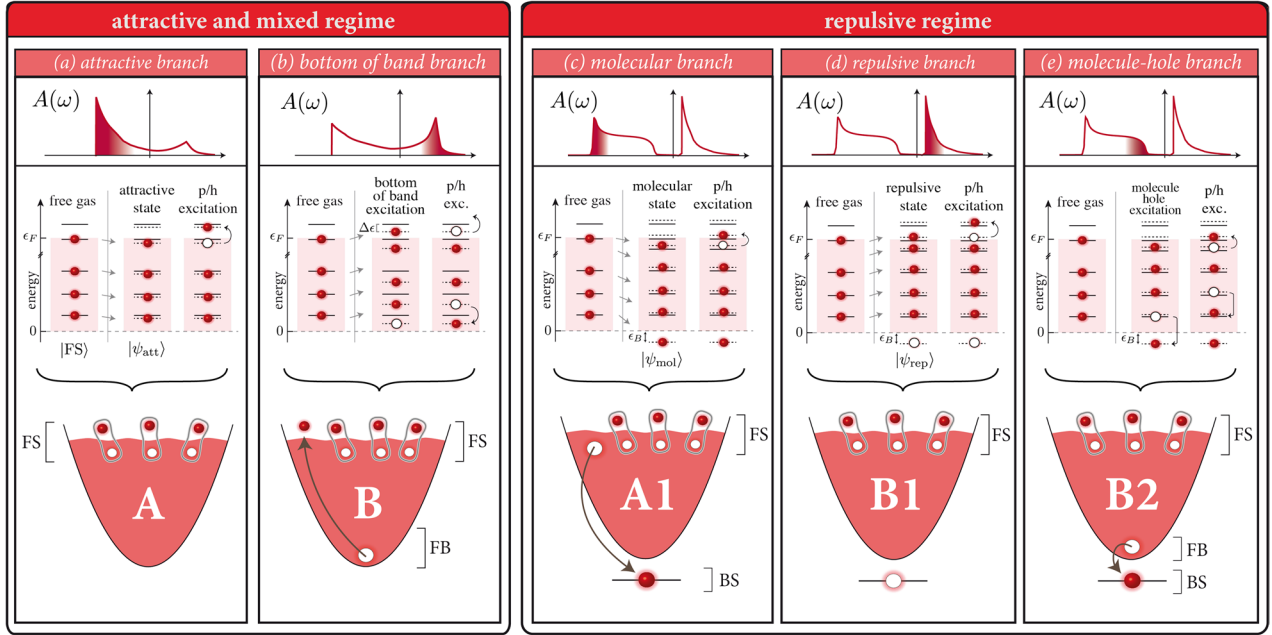


Figure 6. Illustration of the excitation branches dominating the OC dynamics. In the upper panels we illustrate typical absorption spectra realized in the respective interaction regimes. The middle panel shows representatives of many-body states constituting the respective excitation branch. In this panel we illustrate typical rearrangements of atoms (solid red spheres) from their non-interacting single-particle states (small solid, horizontal lines) into interacting states (small dashed, horizontal lines). Dependent on the interaction, those states are either shifted upwards or downwards in energy, and their wave function overlap with the non-interacting states is modified as well. In this panel ϵ_F is the Fermi energy, ϵ_B the binding energy of the molecule present for $a > 0$, $\Delta\epsilon$ the energy shift of single-particle levels due to interactions with the impurity, and $|\text{FS}\rangle$ represents the Fermi sea in its non-interacting ground state. The combined effect of the processes shown in the middle panel leads to the characteristic features in the absorption spectra shown in the upper panels where shaded regions highlight the corresponding contributions. The characteristic excitations of each branch are summarized in the lowest panel where FS, FB, and BS are short-hand for Fermi-surface, bottom-of-the-Fermi-sea, and bound-state contributions, respectively.

function of frequency ω/ϵ_F and inverse interaction strength $1/k_F a$ for the temperature $T/T_F = 0.16$ and range parameter $k_F r^* = 0.71$. In figure 5 corresponding spectral cuts are shown for each of the interaction regimes realized by the specific interaction strengths $1/(k_F a) = -0.91, -0.1, \text{ and } 1$, respectively, which range from the ‘attractive’ ($a < 0$) to the ‘repulsive’ side ($a > 0$) of the Feshbach resonance. We show results for both low ($T/T_F = 0.01$, dashed) and high temperatures ($T/T_F = 0.16$, solid). Note that the results are shown for the finite value $T/T_F = 0.01$ as we discuss this case also when considering the real-time response in section 5.

The reverse RF spectra are dominated by two main excitations. The ‘attractive excitation branch’ appears as a pronounced response at negative detuning $\omega/\epsilon_F < 0$. It is dominant in the attractive and mixed regime for $k_F a < 0$. As the resonance is crossed to positive values of $1/k_F a$ (figures 5(a)–(c)) the attractive branch loses weight and the ‘repulsive excitation branch’ emerges at positive energies and carries most of the spectral weight. As can be seen from the spectral cuts in figure 5, at ultralow temperatures both excitation branches exhibit a non-analytical onset in frequency. These absorption edges are a key signature of the Anderson orthogonality catastrophe (OC) [10–12, 73], and they are a consequence of the absence of quasiparticles at zero temperature for an infinitely heavy impurity.

4.1.1. From Fermi polarons to the orthogonality catastrophe. Before we turn to the case of an infinitely heavy

impurity, which is the focus of this report, let us briefly consider the general case of an impurity of arbitrary mass M . The formation of a polaron is associated with the dressing of the impurity by fluctuations in the many-body environment. These fluctuations correspond to various ways in which the fermions reoccupy their single-particle energy levels due to the interaction with the impurity. This reoccupation becomes apparent when expanding the many-body eigenstates of the system in particle-hole fluctuations [33, 36]:

$$|\psi_\alpha\rangle = \sqrt{Z_\alpha} \hat{d}_0^\dagger |\text{FS}\rangle + \sum_{\mathbf{k}\mathbf{q}} \alpha_{\mathbf{k}\mathbf{q}} \hat{d}_{\mathbf{q}-\mathbf{k}}^\dagger \hat{c}_{\mathbf{k}}^\dagger \hat{c}_{\mathbf{q}} |\text{FS}\rangle + \dots \quad (13)$$

Here we consider the case of zero total momentum, the operators $\hat{d}_{\mathbf{p}}^\dagger$ create an impurity in the momentum state \mathbf{p} , and $|\text{FS}\rangle$ represents the non-interacting Fermi sea in its ground state. The second term in this expression corresponds to the generation of a *single* particle-hole fluctuation from the Fermi sea, but to obtain the exact eigenstates of the system the complete expansion (indicated by the dots) has to be considered.

While all eigenstates of the many-body Hamiltonian can be described by equation (13), of particular interest are often those states $|\psi_\alpha\rangle$ that have finite overlap with the non-interacting state of the system $|\psi_0\rangle \equiv \hat{d}_0^\dagger |\text{FS}\rangle$. States with a finite *quasiparticle weight* $Z_\alpha \equiv |\langle \psi_0 | \psi_\alpha \rangle|^2$ represent quasiparticles, called polarons, that bear close resemblance to their non-interacting counterparts. As outlined in the introduction, for a mobile impurity in three dimensions two of these polaron

states dominate the absorption response: the ‘attractive Fermi polaron’ $|\psi_{\text{att}}^{\text{pol}}\rangle$ exists at negative energy for sufficiently weak attractive interactions, while the ‘repulsive Fermi polaron’ $|\psi_{\text{rep}}^{\text{pol}}\rangle$ appears at positive energy in the repulsive interaction regime (in addition to a dressed molecular state existing in this regime at negative frequencies).

Polaron states can only exist when the particle-hole fluctuations generated by the higher-order terms in equation (13) are moderate enough to allow for a finite quasi-particle weight Z_α . Although particle-hole fluctuations close to the Fermi surface come with no energy cost, they lead to a finite recoil energy experienced by an impurity of finite mass. For the leading term shown in equation (13), this energy is given by $E_{\text{rec}} = (\mathbf{k} - \mathbf{q})^2/2M$. In a simple picture, this energy cost suppresses particle-hole fluctuations and leads to a finite Fermi polaron quasiparticle weight $Z > 0$.

This is different for impurities of infinite mass and from our simple argument it is apparent that something remarkable must happen in this limit. Here the recoil energy vanishes and the energetic suppression of high-order particle-hole fluctuations is absent. As it turns out the fluctuations become indeed so dominant that they lead to the complete disintegration of the quasiparticle and the weight $Z = 0$ vanishes identically. Hence the many-body ground state $|\psi_{\text{GS}}\rangle$, which for a mobile impurity at weak interactions had been $|\psi_{\text{att}}^{\text{pol}}\rangle$, becomes now completely orthogonal to its non-interacting counterpart, $Z = |\langle\psi_0|\psi_{\text{GS}}\rangle|^2 = 0$, and one encounters the ‘orthogonality catastrophe’ (OC) [10]: no quasiparticles exist [11].

Describing the OC requires the inclusion of the higher-order terms in the expansion (13) which poses a challenge for theory that attracted intensive interest starting with the work of Anderson [10]. Among other approaches [11, 125–134], for overviews we refer to [1, 9, 135, 136], the FDA provides an efficient tool to address this problem and yields exact results for infinitely heavy impurities, also in the case of finite temperature where thermal averages have to be performed.

4.1.2. Single-particle interpretation. The fluctuations in equation (13) correspond to the various ways in which fermions can occupy their single-particle energy levels. The analysis of this reoccupation of states becomes particularly simple in the limit of an infinitely heavy impurity, where it corresponds to a static scattering center and the exact single-particle states are thus easily calculated.

Our analysis is illustrated in figure 6. In the upper panels we show typical absorption spectra in the various interaction regimes, while in the middle panel we illustrate the single-particle energies of \hat{H} and \hat{H}_0 as dashed and dotted lines, respectively. We show here only s-wave states; for short-range interactions, higher partial waves are not renormalized and hence irrelevant. In the initial state where the impurity as a scattering center is absent, the atoms fill up all these levels up to the Fermi energy ϵ_F and build a perfect Fermi sea |FS> (left subfigures). To the right, we show the single-particle energies when the impurity scattering center is present (dashed horizontal lines). We illustrate various occupations of those single-particle states which correspond to dominant features in the absorption spectrum $A(\omega)$.

The specific structure of the absorption spectra can be understood in a simple single-particle picture when expressing the spectral function as

$$A(\omega) = 2\pi \sum_{\alpha} |\langle\psi_{\alpha}|\text{FS}\rangle|^2 \delta[\omega - (E_{\alpha} - E_{\text{FS}})]. \quad (14)$$

Here $|\psi_{\alpha}\rangle$ denotes the many-body eigenstates of the interacting Hamiltonian \hat{H} with eigenenergies E_{α} , and E_{FS} is the energy of the initial non-interacting Fermi sea |FS>. Equation (14) is given for $T = 0$ and, as discussed in section 3, it can straightforwardly be extended to finite temperature by an additional summation over initial states weighted by the thermal density matrix.

A pronounced response in the spectrum is due to family of states $\{|\psi_{\alpha}\rangle\}$ which, for a finite size system, have a significant many-body Frank-Condon overlap $|\langle\psi_{\alpha}|\text{FS}\rangle|^2$ with the initial state |FS>. Together with the density of states the overlaps $|\langle\psi_{\alpha}|\text{FS}\rangle|^2$ determine the specific shape of the absorption spectrum. These dominant families of states are called excitation branches in the following.

Attractive excitation branch. When the microscopic interaction is weakly attractive, i.e. $1/k_F a \ll -1$, the dressing of the impurity by fermionic fluctuations leads to a reduction of energy. This leads to the formation of an attractive dressed impurity state $|\psi_{\text{att}}\rangle$ constituting the new ground state of the system. In the spectral cut shown in figure 5(a) the attractive ground state can be identified as the pronounced edge feature at negative detuning ω/ϵ_F . The onset of this feature at negative frequency is determined by eigenenergy E_{att} of the attractive state $|\psi_{\text{att}}\rangle$. This state is constructed by filling all interacting single-particle states up to the Fermi energy and it has zero quasiparticle weight $Z = |\langle\text{FS}|\psi_{\text{att}}\rangle|^2 = 0$ in the limit of infinite system size.

As illustrated by the horizontal dashed lines in figure 6, each single-particle level is subject to a small, negative energy shift $\Delta\epsilon$ which is determined by the scattering phase shift $\delta(E) \equiv \delta_{k=\sqrt{2mE}}$ evaluated at the respective single-particle energy E (see equation (A.5) in appendix A). Each fermion occupying these single-particle states acquires this energy shift and the summation over all $\Delta\epsilon$ determines the energy E_{att} , shown as a dashed line in figure 4(a). This summation reflects Fumi’s theorem [96], which states that the ground state energy is determined by the sum over the single-particle phase shifts [1, 4, 36, 60], see also appendix C.

We emphasize once more that for $T = 0$ the immobile impurity in its attractive ground state has zero quasiparticle weight $Z = |\langle\text{FS}|\psi_{\text{att}}\rangle|^2 = 0$ in the thermodynamic limit, signaling the breakdown of the polaron picture. This is different for a mobile impurity in three dimensions¹⁰: here $|\psi_{\text{att}}\rangle$ corresponds to the attractive polaron state $|\psi_{\text{att}}^{\text{pol}}\rangle$ with a finite quasiparticle weight Z that leads to a delta-peak response in absorption spectroscopy at $T = 0$. This is in contrast to the infinite-mass impurity where the finite weight in the delta function is fully redistributed into the asymmetric wing attached to the onset of the spectrum at E_{att} .

¹⁰ The case of a mobile impurity in a Fermi gas in two dimension is still not fully understood [9]; see also the recent work [134].

This asymmetric continuum, visible on top of the attractive ground-state excitation in figure 5, is due to the excitation of an arbitrary number of *low-energy particle-hole excitations* close to the Fermi surface. One representative member of this family of states, massively contributing to the sum in equation (14), is illustrated in the third column in the center panel in figure 6(a). The whole family of states, including $|\psi_{\text{att}}\rangle$, contributing to the edge and the attached ‘wing’ in the absorption spectrum (red shaded area in the spectrum in figure 6(a)) constitutes the ‘attractive excitation branch’.

For weak attraction each of the slightly renormalized *single-particle* states has a large overlap with its non-interacting counter part (dotted versus solid lines in the center panels of figure 6) and hence, by moving all fermions ‘down’ to the attractive ground-state configuration, the largest many-body overlap $|\langle\psi_{\alpha}|\text{FS}\rangle|^2$ can be achieved. This leads to the attractive branch as the dominant feature in the spectrum in the attractive interaction regime and it almost saturates the spectral sum rule.

This changes as attraction is increased. As illustrated in figure 6(b), for stronger attraction the single-particle states are shifted further down in energy and the attractive ground state becomes more deeply bound. At the same time the overlaps of the single-particle states with their corresponding non-interacting counterparts become progressively smaller so that the spectral feature of the attractive excitation branch loses weight.

Bottom-of-the-band excitation branch. Related to this loss of spectral weight is the appearance of an additional feature in the absorption spectrum as unitary scattering close to the Fermi surface, i.e. $\delta_{\text{F}} = \pi/2$, is approached. In this strong-coupling regime, the overlap of single-particle levels is such that a new pronounced excitation is favored at an energy ϵ_{F} above the attractive ground-state excitation. As illustrated in the second column of the center panel in figure 6(b), this feature corresponds to the distribution of the fermions into single-particle levels such that the lowest scattering state at the bottom of the Fermi sea remains empty. Hence the feature is termed the ‘bottom-of-the-band excitation’ [73].

First let us consider contact interactions. Here, at unitarity, where interactions are resonant, the phase shift is $\delta(E) = \pi/2$ for all scattering energies. From equation (A.5) of appendix A it then follows that the single-particle levels are located at half-way of their non-interacting counterparts (see second column in the middle panel of figure 6(b)). As a consequence of this symmetry, the same overlap $|\langle\psi_{\alpha}|\text{FS}\rangle|^2$ is achieved for moving all particles ‘up’ in energy to build the bottom-of-band excitation state or ‘down’ into the attractive ground state $|\psi_{\text{att}}\rangle$ where all low-energy levels are filled. Furthermore, the energies of the attractive and the bottom-of-band feature are given by $-\epsilon_{\text{F}}/2$ and $+\epsilon_{\text{F}}/2$, respectively.

In the mixed regime, realized for $k_{\text{F}}r^* > 0$, the phase shift at the Fermi surface δ_{F} exceeds $\pi/2$. We find that this leads to the bottom-of-the-band excitation acquiring a larger spectral weight compared to the attractive excitation branch while both excitations remain separated by approximately the Fermi energy. This behavior makes the bottom-of-band excitation

distinct from the repulsive state excitation to be discussed below.

Similarly to the attractive ground state, also the bottom-of-the-band feature can be dressed by particle-hole excitations. This effect leads to the characteristic enhancement of response on both sides of the bottom-of-the-band excitation (see shaded area in the upper panel of figure 6(b)). This collection of states defines the ‘bottom-of-the-band excitation branch’ and it dominates the spectrum in the mixed interaction regime, see figure 6(b). In a contact interaction model ($k_{\text{F}}r^* = 0$), where the mixed interaction regime is absent, the bottom-of-the-band branch still exists, but it does neither dominate the spectrum in weight, nor—as discussed in the following section—does it represent the so-called leading branch in the real-time dynamics.

Molecular excitation branch. When the attractive interaction becomes sufficiently strong, a single-particle bound state appears at zero energy as the Feshbach resonance at $1/k_{\text{F}}a = 0$ is crossed to the repulsive interaction regime where $a > 0$. This bound state with binding energy $\epsilon_{\text{B}} = -\hbar^2/2ma^2$ close to unitarity is energetically separated from the scattering states. By filling all particles into the low-lying states *including the bound state* one constructs the dressed ‘molecular ground state’ $|\psi_{\text{mol}}\rangle$ (see figure 6(c)). This state, which becomes the new ground state of the system after crossing the Feshbach resonance to $a > 0$, is reflected in the sharp spectral onset at its negative eigenenergy E_{mol} . Additional particle-hole excitations lead to a continuum of states attached to it, together constituting the ‘molecular excitation branch’. However, the molecular excitation branch does not represent the dominant branch in the absorption response (see figure 5(c)). In fact, the bound state has a wave function which decays exponentially in space as $\sim e^{-r/a}$ and hence it has decreasing overlap with the low-energy scattering states as $a > 0$ becomes smaller. In consequence, the weight of the molecular branch diminishes as one moves further away from the Feshbach resonance.

Repulsive excitation branch. In contrast, a many-body state with a much larger many-body overlap $|\langle\psi_{\alpha}|\text{FS}\rangle|^2$ can be constructed by leaving the bound state empty, and instead filling the lowest scattering states with all the atoms. This excited ‘repulsive state’ $|\psi_{\text{rep}}\rangle$ is illustrated in the second column of the middle panel in figure 6(d) and leads to the spectral edge at positive energies observed on the ‘repulsive’ side of the Feshbach resonance.

The existence of the repulsive state originates from the fact that the emergence of the bound state for $a > 0$ is tied to a reassignment of scattering states. While for $a < 0$ the single-particle levels are shifted downwards in energy, for $a > 0$ the scattering states are effectively shifted upwards in energy (see figures 6(c)–(e)). This reassignment of states becomes particularly apparent when considering the limit $a \rightarrow 0^+$ far away from resonance. Here the positive energy shifts of the scattering states approach zero from above. Indeed it is this upward shift of single-particle scattering states that motivates the term ‘*repulsive*’ interaction regime although the microscopic interaction of course still remains attractive.

The repulsive state can again be ‘dressed’ by fluctuations around the Fermi surface leading to the continuous spectrum directly attached to the repulsive state (illustrated as red shaded area in figure 6(d)). In contrast to the bottom-of-the-band excitation, however, only dressing towards energies above the edge of the repulsive state is efficient due to the finite binding energy of the molecule. The energy of the repulsive state can again be calculated analytically by a summation over the single-particle energy shifts reflecting Fumi’s theorem, here applied to an excited many-body state. The resulting energy E_{rep} is shown as dashed-dotted line in spectrum in figure 4.

While for an infinitely heavy impurity the repulsive state has zero quasiparticle weight, for an impurity of finite mass the repulsive state becomes the repulsive Fermi polaron extensively discussed in literature [51, 53, 59, 60, 73, 107] and observed in cold atoms [67, 68, 70] as well as two-dimensional semiconductors [30]. Its analog for impurities immersed in a Bose-Einstein condensate was recently observed as well [91, 92] following intensive theoretical studies [137–152].

Molecule-hole excitation branch. The bound state can be filled by any state from the Fermi sea which leads to the broad excitation band of width ϵ_F above the molecular ground state called the ‘molecule-hole continuum’ [53, 60, 67]. The upper edge of that band at $E_{\text{mol}} + \epsilon_F$ is again dressed by particle-hole excitations. The collection of these states constitutes the ‘molecule-hole excitation branch’ and it represents the analog of the bottom-of-the-band branch for $a > 0$. Note that at energies $\omega < 0$ but above $E_{\text{mol}} + \epsilon_F$ we find that a spectral gap appears where the weight is exponentially suppressed, a phenomenon that is reminiscent of the ‘dark continuum’ found in diagrammatic Monte Carlo studies of mobile impurities by Goulko [56].

4.1.3. Comparison to experiments. The reverse RF absorption spectrum of impurities has been measured in LiK mixtures [31, 67]. In these experiments the K impurity atoms are mobile. However, as shown in [31], by appropriately identifying the scattering parameters in our model, our theory can also be applied also in this case to obtain an approximate solution due to the large mass imbalance between K and Li atoms and the relatively high temperatures $T/T_F \gtrsim 0.1$. Specifically, our reduced mass differs by a factor $(40/46)$ from the experimental one [31, 67, 71]. According to equation (6) this difference in the effective mass affects the coupling strength g between the open-channel atoms and the closed-channel molecule. In order to achieve the same coupling g as realized in experiments we have to choose a rescaled Feshbach range parameter $k_{\text{F}} r_{\text{exp}}^* = k_{\text{F}} r_{\text{exp}}^* (40/46)^2$ which is reduced with respect to the experimental value $k_{\text{F}} r_{\text{exp}}^*$ (for a detailed discussion see [31]).

In figure 4 we show the comparison of the FDA prediction of the reverse RF spectrum to the experimental data obtained in [67] taken at low (b) and high (c) RF power for the experimentally realized range $k_{\text{F}} r_{\text{exp}}^* = 0.95$ and temperature $T/T_F = 0.16$. In all subfigures we also show as dashed and dot-dashed lines the analytically calculated energies of the

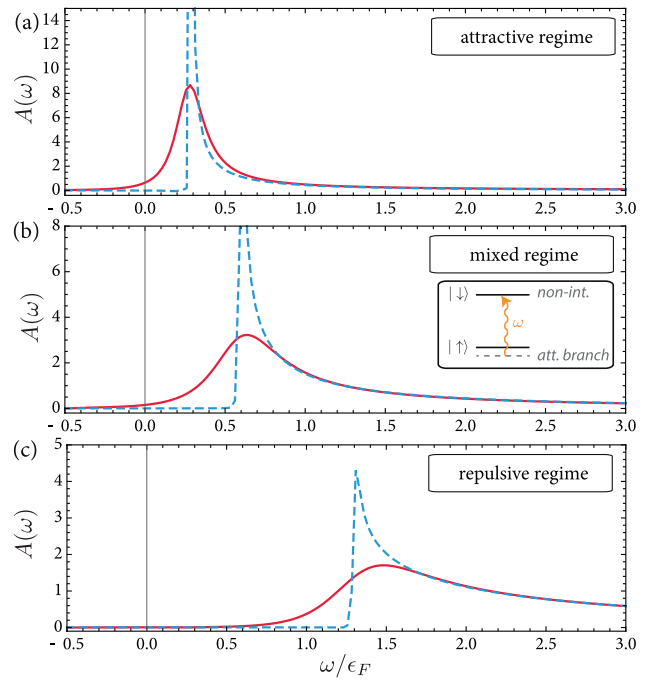


Figure 7. Radio-frequency absorption spectra in the standard RF scheme. In the standard scheme, the system is prepared in its many-body ground state where the impurity is initially interacting with the Fermi gas. It is then driven to a state non-interacting with the gas (see inset in (b) for an illustration). The spectra are shown for the same parameters as in figure 5, i.e. $T/T_F = (0.01, 0.16)$ (dashed, solid), interaction strengths $1/k_{\text{F}} a = (-0.91, -0.1, 1.0)$, and Feshbach range parameter $k_{\text{F}} r_{\text{exp}}^* = 0.71$.

attractive and repulsive state obtained from Fumi’s theorem as also discussed in [36, 60] and appendix C. Our finite temperature spectra are in excellent agreement with the experimental data not only in energy but also spectral line shapes (see also [31]) without any free parameters or artificial broadening of spectral lines.

The good agreement in spectral line shapes when applying our theory to the finite mass case, where it becomes an approximation, has two origins. First, although for the infinitely heavy impurity the ground state—e.g. $|\psi_{\text{att}}\rangle$ with energy E_{att} —loses all its quasiparticle weight, this weight is predominately redistributed to a continuum of states that are energetically close to E_{att} . Hence the *integrated weight* taken from a sufficiently large energy window around the attractive state can gain an integrated strength that is comparable to the finite mass case. Therefore, for experiments that are subject to broadening of spectral lines due to external factors (such as trap average, laser lines width, etc), observed line shapes and weights for the finite and infinite-mass case can appear quite similar and distinguishing both cases remains a challenge for frequency-domain measurements. Second, temperature has the effect of broadening spectral lines. As we will show in the following section 5, for finite temperature one can assign a thermal weight to the dominant attractive and repulsive state even for impurities of infinite mass. This leads to an absorption profile of Lorentzian line shape that is similar to the case of a mobile impurities and which further contributes to the good agreement between infinite-mass theory and experiment.

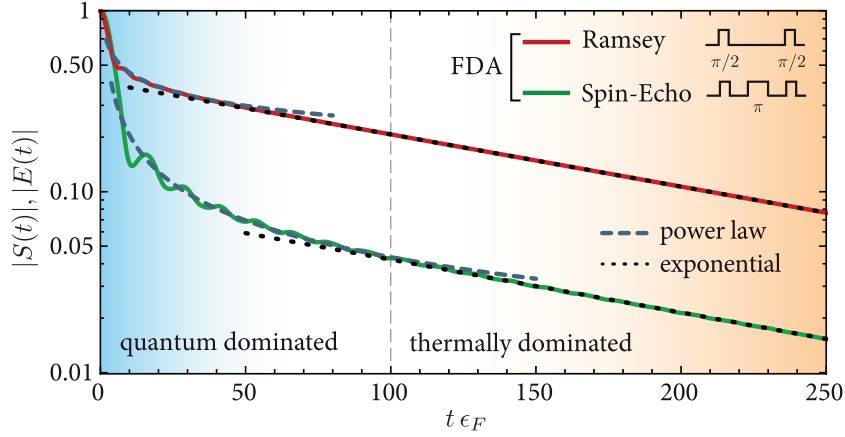


Figure 8. Real-time evolution of Ramsey and spin-echo response. At finite temperature, the real-time Ramsey and spin-echo response of the impurity atom unveil a quantum-to-classical crossover from short to long times. Here, the effective range, temperature, and scattering length are given by $k_F r^* = 0.8$, $T = 0.01 T_F$, and $k_F a = -1.1$, respectively. The vertical dashed line indicates the thermal time scale $\tau_{\text{th}} = \hbar/k_B T$. While for $t < \tau_{\text{th}}$ the spin-echo signal exhibits a three times faster power-law decay than the Ramsey signal, both signals are governed the same exponential decay rate in the thermal regime for $t > \tau_{\text{th}}$. The dashed and dotted lines on top of the FDA data show the analytical result for the OC-characteristic power-law decay at early times and thermal exponential decay of coherence at long times, respectively.

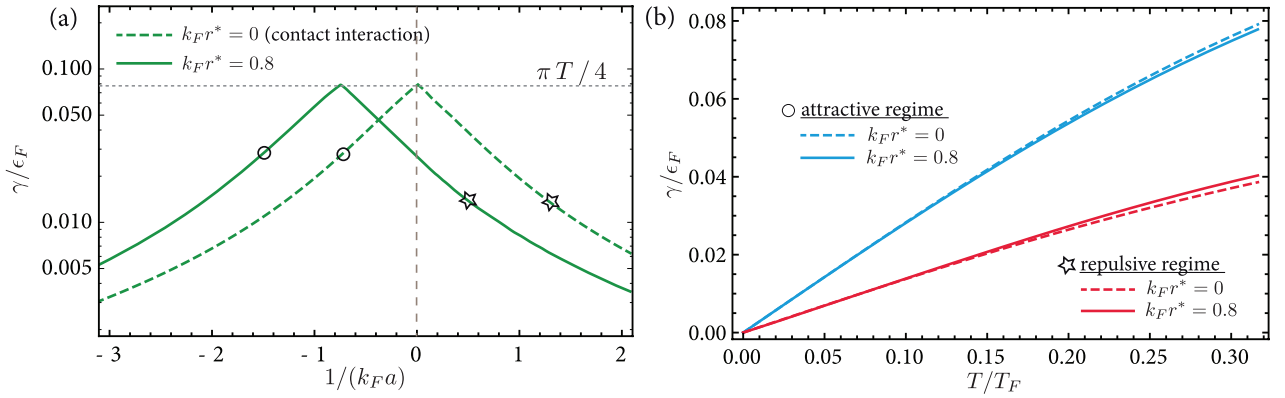


Figure 9. Finite temperature decoherence rate of Ramsey and spin-echo signal. (a) The long-time decoherence rate γ , as extracted from a fit to the long-time exponential decay of the Ramsey and spin-echo signal computed by FDA, is shown as a function of the inverse scattering length for $T/T_F = 0.1$. The decoherence rate γ of the two-channel model with $k_F r^* = 0.8$ (solid line) is compared with the results from a contact interaction model (dashed line). The decay rate of the Ramsey and spin-echo protocol are identical. (b) Decoherence rate γ as a function of temperature evaluated at the interactions specified as circle and stars in (a). In (b) the interaction parameters are chosen such that in the attractive and repulsive regime both zero and finite range give the same s-wave scattering phase shift δ_F at the Fermi energy. Specifically, in the attractive regime ($\delta_F = 0.95$): $1/k_F a = -0.72$, $k_F r^* = 0$ (dashed blue), and $1/k_F a = -1.5$, $k_F r^* = 0.8$ (solid blue); repulsive regime ($\delta_F = -0.66$): $1/k_F a = 1.28$, $k_F r^* = 0$ (dashed red), and $1/k_F a = 0.5$, $k_F r^* = 0.8$ (solid red).

4.2. Standard RF spectra

The attractive Fermi polaron has been observed first in a two-component ^6Li Fermi gas using the ‘standard’ RF scheme [57], and its quasi-particle properties, such as its energy and residue were measured. To illustrate the impact of the different RF protocols we show in figure 7 our prediction for the absorption spectrum as obtained in the standard RF scheme for the same parameters as in figure 5. As discussed in section 3, in the standard RF scheme the system is initially prepared in the interacting many-body ground state and then driven to a non-interacting final state.

The spectra are distinctly different from the reverse RF scheme. Since in the standard RF scheme the ground state, e.g. $|\psi_{\text{att}}\rangle$ for $a < 0$, is prepared initially, one has always to pay its energy, e.g. E_{att} , to ‘break’ this state. This leads to a shift to positive energies in the absorption spectrum, which

increases as the interactions are tuned across the Feshbach resonance. This shift has been observed by Schirotzek [57]. In particular, as $k_F a > 0$ and the bound state appears in the spectrum, the ‘break-up energy’ involves the binding energy of the molecule. Note that the repulsive state $|\psi_{\text{rep}}\rangle$, that corresponds to the repulsive Fermi polaron for finite-mass impurities, cannot be revealed using the standard RF scheme, unless it is prepared as an excited, non-equilibrium initial state of the system [68].

5. Universal many-body response: dephasing dynamics

In typical condensed matter experiments, real-time observables such as the many-body overlap $S(t)$ in equation (10) are challenging to measure due to the large size of the Fermi

energy ϵ_F . For instance, in typical solid state materials the corresponding Fermi time $\tau_F = \hbar/\epsilon_F$ is on the order of attoseconds [153]. In contrast, in ultracold atomic gases the Fermi energy is lower by many orders of magnitude due to the diluteness of ultracold atomic gases and large atomic masses, which leads to Fermi times on the order of μs to ms . The combination with interferometric techniques available in atomic experiments makes it then possible to study many-body correlation functions in fermionic systems in real time and to observe striking far-from-equilibrium many-body dynamics.

5.1. Exact numerical solution

The time-dependent impurity problem represents an instance where intriguing dynamics can be observed in an exactly solvable many-body system. In figure 8 we show the Ramsey signal (solid, red line) and the spin-echo response (solid, green line) for a system in the attractive interaction regime characterized by $k_F r^* = 0.8$, $T = 0.01 T_F$ and interaction strength $k_F a = -1.1$, as calculated by the FDA. Again, we assume infinitely fast $\pi/2$ spin rotations both in the Ramsey and spin-echo sequence.

At times that are short compared to the inverse temperature, quantum mechanics governs the evolution: due to the sudden switch-on of interactions at $t = 0$ the many-body wave function dephases, leading to a power-law decay of the Ramsey response with the exponent $(\delta_F/\pi)^2$, being the universal real-time signature of the Anderson orthogonality catastrophe [10, 11].

When time becomes comparable to the inverse temperature, $t \gtrsim \tau_{\text{th}} \sim \hbar/k_B T$, thermal fluctuations disrupt the coherent and time-reversal symmetric quantum many-body dynamics, and a crossover from quantum to predominantly thermal dynamics takes place, see figure 8. The precise time scale for this crossover depends on the microscopic details, such as the scattering length and the effective range. However, this time scale depends also on the chosen observable: for instance, in the Ramsey signal a crossover to exponential dephasing sets in earlier as compared to the spin-echo signal.

One key signature of the asymptotic finite-temperature behavior is an exponential decay of coherence, $|S(t)| \sim e^{-\gamma t}$. Remarkably, while in the quantum regime at early times, before thermal decoherence sets in, the dephasing rate is sensitive to the specific spin rotation protocol chosen (e.g. the spin-echo response decays faster than the Ramsey signal), using the theory of Toeplitz determinants [19, 154], we prove (see appendix E) that at finite temperature the long-time decoherence rate γ is identical for Ramsey and spin-echo interferometry—even though in the spin-echo sequence the impurity spin is flipped in the middle of the time evolution. This fact is of particular relevance for recent experiments which inferred the long-time decay of the impurity Green's function from the spin-echo and not the Ramsey signal [71] (see also the discussion in section 5.4).

In figure 9(a), we show the interaction dependence of the finite-temperature decoherence rates γ at $T/T_F = 0.1$ which are identical for both Ramsey and spin-echo interferometry. The rates are extracted from a fit to the very long-time decay of the numerically evaluated $S(t)$ and $S_{\text{SE}}(t)$ response, such

as shown in figure 8. We compare the decoherence rate for finite $k_F r^* = 0.8$ and for zero range $k_F r^* = 0$ corresponding to a model with contact interactions.

As expected, for zero-range interactions, the maximum decoherence rate arises at $k_F a \rightarrow \infty$. The inclusion of a finite range has the consequence of shifting this maximum of the decoherence rate away from the center of the Feshbach resonance. This shift can be understood from an analysis of the most relevant scattering processes which, due to Pauli blockade, take place close to the Fermi surface. The impurity-particle scattering rate is determined by the scattering amplitude $f(k)$ and hence the scattering phase shift δ_F , see equation (1), evaluated at the Fermi energy $E = \epsilon_F$.

For finite range $r^* > 0$, the magnitude of the scattering amplitude becomes maximal not at $k_F a = \infty$ but when the phase shift δ_F equals $\pi/2$. The corresponding critical scattering length a_{cr} marks the transition from the attractive to the mixed interaction regime. The shift in the decoherence rate can be seen in figure 9(a) where the maximum decoherence is reached at $1/k_F a_{\text{cr}} = -k_F r^* = -0.8$. The finite effective range in (1) hence leads to the, at first sight, counterintuitive effect that, in the mixed regime, decoherence can slow down as the magnitude of the scattering length a increases. Remarkably this also implies that the position of the decoherence maximum can be used to determine the few-body effective range from thermal many-body observables.

In figure 9(b), we show the temperature dependence of the exponential decay rate obtained from exact calculations of $S(t)$. In this figure, we compare the thermal decay rate γ on both sides of the Feshbach resonance for zero and finite-range interactions. To highlight the universality of our results, we choose interaction parameters so that for both scenarios the phase shifts δ_F are equal. We find that only at temperatures $T/T_F \gtrsim 0.15$ deviations become visible. This signifies the highly universal character of the physics which is dominated by the low-energy scattering phase shift alone and does not depend on the microscopic details of interactions. For low temperatures, we prove below that the maximal thermal dephasing rate for heavy impurities interacting with a Fermi gas with short-range interactions is in the long-time limit universally given by

$$\gamma_{\text{max}} = \frac{\pi}{4} T. \quad (15)$$

This value is saturated at the transition from the attractive to the mixed interaction regime.

As the temperature goes to zero, the thermal decoherence rate γ vanishes. In this limit, the asymptotic exponential form of the decay breaks down and logarithmic corrections start to dominate. Those lead to the power-law decay of $S(t)$ as the key signature of the Anderson orthogonality catastrophe with an exponent given by $(\delta_F/\pi)^2$. In contrast to the long-time exponential decay at finite temperature, at zero temperature the power law exponent *does depend* on the trajectory of the impurity spin on the Bloch sphere which are different for Ramsey or spin-echo interferometry. In particular, quantum interference effects enhance the exponent at each spin flip in an interferometric sequence [73].

Using the theoretical techniques of [13, 73], we prove that the spin-echo exponent is enhanced by a factor three; details are given in appendix E.2.

We note that for very narrow Feshbach resonances with $k_F r^* \gg 1$ the deviations from the contact interaction model, visible in figure 9(b), set in at lower temperatures. This is due to the fact that for such resonances the phase shift $\delta(E)$ close to the Fermi surface becomes strongly energy dependent. The thermal softening of the Fermi distribution function allows fermions to probe this energy dependence which leads to the deviations of dephasing rate from the contact interaction model.

5.2. Analytical results

While the previous subsection focused on an exact *numerical* evaluation of the Ramsey signal at all times, we will now derive *analytical* expressions at intermediate and long times. Analytical results for the short-time dynamics will be discussed in section 6.

In this section, we are interested in the many-body regime of quantum dynamics where $t\epsilon_F \gg 1$ and study the crossover from the ‘low-T’ regime (with $tT \ll 1$), where $S(t)$ exhibits power-law dephasing [10, 11, 126, 136], to the ‘high-T’ regime ($tT \gg 1$) showing exponential decay (figure 8) [127]. While analytic understanding of the Ramsey response has been developed in [73] in the low-T regime for zero-range interactions, below we focus on the high-T regime.

5.2.1. Excitation branches. Similarly to the absorption spectrum $A(\omega)$ discussed in section 4, the time-dependent overlap $S(t)$ can be decomposed into the sum

$$S(t) = \sum_{\{|\psi_\alpha\rangle\}} |\langle \psi_\alpha | \text{FS} \rangle|^2 e^{iE_{\text{FS}}t} e^{-iE_\alpha t}, \quad (16)$$

where $\{|\psi_\alpha\rangle\}$ denotes the complete set of many-body eigenstates of the ‘interacting’ Hamiltonian \hat{H} with eigenenergies E_α , and $|\text{FS}\rangle$ the non-interacting Fermi sea.

Being directly related by Fourier transforms, $A(\omega)$ and $S(t)$ carry the same physical information (for details see appendix B). Depending on the interaction regime, different ‘excitation branches’ $\{|\psi_\alpha\rangle\}$ dominate the dynamics of $S(t)$. In section 4 we identified five such branches (summarized in figure 6), and to make the discussion in this section self-contained we repeat here our main findings.

In the attractive and mixed regimes (a) and (b), the absorption spectra are dominated by the attractive state together with particle-hole (p/h) excitations around the Fermi surface (FS); this collection of states constitutes the ‘attractive excitation branch’ (branch A). Another relevant class of excitations in regimes (a) and (b) is the bottom-of-the-band contribution (FB, for ‘Fermi bottom’). Together with p/h excitations it forms the ‘bottom-of-the-band branch’ (branch B), see figure 6(b). We find that these two branches describe accurately the long-time many-body dynamics and $S(t)$ can be approximated as

$$S(t) \approx S_A(t) + S_B(t), \quad (17)$$

where $S_A(t)$ accounts for the attractive branch A, and $S_B(t)$ accounts for the bottom-of-the-band branch B.

The two branch contributions can be written as

$$S_A(t) = C_A S_0^{(\text{FS})}(t), \quad S_B(t) = C_B S_1^{(\text{FS})}(t) S_{-1}^{(\text{FB})}(t). \quad (18)$$

Here $S_n^{(\text{FS})}(t)$ and $S_n^{(\text{FB})}(t)$ represent excitations around the Fermi level and the creation of a hole at the bottom of the Fermi sea, respectively. The subscript n specifies the number of particles added or removed from the Fermi surface or bottom of the Fermi sea. Note that the total particle number is conserved in each of the branches. For instance, in $S_B(t)$ one particle is removed from the bottom of the band and inserted close to the Fermi surface.

In the ‘repulsive regime’ (c), where $\delta_F < 0$ and a bound state (BS) is present, three relevant branches can be identified and $S(t)$ approximated as

$$S(t) \approx S_{A1}(t) + S_{B1}(t) + S_{B2}(t). \quad (19)$$

The three branches, denoted as ‘molecular excitation branch’ A1, the ‘repulsive excitation branch’ B1, and the ‘molecule-hole branch’ B2 correspond to the most relevant spectral features discussed in section 4. As illustrated in figure 6(c), $S_{A1}(t)$ represents the attractive ground state ‘dressed’ by p/h excitations. In the spectral function those states correspond to the absorption edge at negative frequencies, while $S_{B1}(t)$ accounts for p/h excitations close to the Fermi surface on top of the repulsive state, see figure 6(d). Finally, $S_{B2}(t)$ describes the edge of the molecule-hole continuum and represents the family of states where the bound state is filled by an atom from the bottom of the Fermi sea again dressed by p/h fluctuations at the Fermi surface, see figure 6(e). Accordingly, the branch contributions can be expressed in terms of the processes (FS), (BS), and (FB),

$$\begin{aligned} S_{A1}(t) &= C_{A1} S_{-1}^{(\text{FS})}(t) S_1^{(\text{BS})}(t), \\ S_{B1}(t) &= C_{B1} S_0^{(\text{FS})}(t), \\ S_{B2}(t) &= C_{B2} S_0^{(\text{FS})}(t) S_{-1}^{(\text{FB})}(t) S_1^{(\text{BS})}(t). \end{aligned} \quad (20)$$

While the contributions $S_\alpha(t)$ can be analytically evaluated as we will now demonstrate, the coefficients C_α in equations (18) and (20) depend on the microscopic details, and have to be determined from a numerical evaluation of equation (12).

5.2.2. Temperature independent contributions. First, we turn to the contributions from the bottom of the Fermi sea $S_{-1}^{(\text{FB})}(t)$ and the bound state $S_1^{(\text{BS})}(t)$. Both involve states deep under the Fermi sea and hence yield temperature-independent contributions to the dynamics. The bound-state contribution is simply given by the phase accumulation of the form

$$S_1^{(\text{BS})}(t) \propto e^{-i\epsilon_B t}, \quad (21)$$

where $\epsilon_B < 0$ is the energy of the bound state.

Table 1. Summary of the interaction regimes and branches. The various branches contributing to the dephasing of $S(t)$. The leading branches, leading dephasing rates, as well as references to the high temperature corrections are indicated for the different interaction regimes (a)–(c).

Interaction regime	Parameters	Branch	Leading	Contribution to $S(t)$	Low- T decay rate γ	High- T correction
(a) ‘Attractive’	$a < 0, \delta(E) > 0,$ $\delta_F < \pi/2$	A	yes	$S_0^{(\text{FS})}(t)$	$\gamma_0 = T\delta_F^2/\pi$	Equation (34)
		B	no	$S_1^{(\text{FS})}(t) S_{-1}^{(\text{FB})}(t)$	$\gamma_1 = T(\delta_F - \pi)^2/\pi$	Equation (38)
(b) ‘Mixed’	$a < 0, \delta(E) > 0,$ $\delta_F > \pi/2$	A	no	$S_0^{(\text{FS})}(t)$	$\gamma_0 = T\delta_F^2/\pi$	Equation (38)
		B	yes	$S_1^{(\text{FS})}(t) S_{-1}^{(\text{FB})}(t)$	$\gamma_1 = T(\delta_F - \pi)^2/\pi$	Equation (34)
(c) ‘Repulsive’	$a > 0, \delta(E) < 0$	A1	no	$S_{-1}^{(\text{FS})}(t) S_1^{(\text{BS})}(t)$	$\gamma_{-1} = T(\delta_F + \pi)^2/\pi$	Equation (38)
		B1	yes	$S_0^{(\text{FS})}(t)$	$\gamma_0 = T\delta_F^2/\pi$	Equation (34)
		B2	yes	$S_0^{(\text{FS})}(t) S_{-1}^{(\text{FB})}(t) S_1^{(\text{BS})}(t)$	$\gamma_0 = T\delta_F^2/\pi$	Equation (34)

For the bottom-of-the-band feature an analysis of the relevant many-body states yields (for details see appendix D)

$$S_{-1}^{(\text{FB})}(t) \propto \int_0^\infty \frac{dE}{\sqrt{\epsilon_F E}} \sin^2 \delta(E) e^{iEt}. \quad (22)$$

Equation (22) has a power-law decay with time $t^{-1/2}$ at $1/\epsilon_F \ll t \ll 1/\epsilon_B^*$ and $t^{-3/2}$ at $1 \ll t \epsilon_B^*$, where we define the energy scale $\epsilon_B^* = 1/(2m|a|^2)$ for both positive and negative a . A similar result for the bottom-of-the-band and bound-state contributions was reported in [73].

5.2.3. Fermi-surface contributions. In contrast to the (BS) and (FB) processes, p/h excitations around the Fermi surface (FS) involve arbitrarily low energies. Hence these processes are influenced by finite temperature and they become responsible for the exponential dephasing of the Ramsey signal.

The behavior of the contributions $S_n^{(\text{FS})}(t)$ can be understood analytically using two approaches. First, bosonization, valid at low temperatures, allows us to describe a crossover from short-time power-law decay to long-time exponential decoherence and allows us to reveal corrections to the temperature dependence of the decoherence rate. Second, the theory of Toeplitz determinants provides analytical expressions for the decoherence rate of the various excitation branches at relatively high temperatures.

5.2.4. Bosonization. In the bosonization approach (for details see appendix D and [4, 29]), the energy dependence of the phase shift $\delta(E)$ is neglected and the dispersion relation is linearized around the Fermi surface. Hence, the approach is only applicable at low temperatures where the Fermi surface is sharply defined. Following standard bosonization techniques one can extract the power-law decay of coherence at $T = 0$,

$$S_0^{(\text{FS})}(t) \propto e^{-i\Delta E t} t^{-(\delta_F/\pi)^2}, \quad (23)$$

which represents the well-known result for the Fermi-edge singularity [11]. Here the energy ΔE determines the spectral onset of the attractive and repulsive polaron feature, which is given by Fumi’s theorem [1, 4],

$$\Delta E = - \int_0^{\epsilon_F} \frac{dE}{\pi} \delta(E), \quad (24)$$

as a sum over all phase shifts up to the Fermi energy (see appendix C).

At finite temperature, a conformal mapping of complex time onto a cylinder with the periodicity i/T leads to (see appendix D and [29, 155, 156])

$$S_0^{(\text{FS})}(t) \propto e^{-i\Delta E t} \left(\frac{\pi T}{\sinh \pi T t} \right)^{(\delta_F/\pi)^2}, \quad (25)$$

which generalizes equation (23) to finite temperature.

Now we turn to the Fermi-surface branch contributions $S_n^{(\text{FS})}(t)$ for $n \neq 0$. These contributions appear when atoms are transferred from the bottom of the Fermi sea to the Fermi surface ($n = 1$) or from the Fermi surface to the bound state ($n = -1$). As derived in the theory of the Fermi-edge singularity [128], and as also discussed in the context of full counting statistics (see, e.g. [22, 157] and references therein), the contributions $S_n(t)$ with $n \neq 0$ are accounted for by a shift $\delta_F \rightarrow \delta_F \pm \pi$. Furthermore, as a particle is removed or added to the Fermi surface, the energy ΔE is modified as well, and $\Delta E \rightarrow \Delta E \pm \epsilon_F$. This leads to the general expression for the various Fermi-surface contributions,

$$S_n^{(\text{FS})}(t) \propto e^{-i(\Delta E + n\epsilon_F)t} \left(\frac{\pi T}{\sinh \pi T t} \right)^{\left(\frac{\delta_F}{\pi} - n\right)^2}. \quad (26)$$

This equation describes the full crossover from the low-temperature regime with power-law behavior

$$S_n^{(\text{FS})}(t) \propto e^{-i(\Delta E + n\epsilon_F)t} t^{-\left(\frac{\delta_F}{\pi} - n\right)^2} \quad (27)$$

to the finite temperature regime where, at sufficiently long times $tT \gg 1$, the Fermi-surface contributions decay exponentially according to

$$S_n^{(\text{FS})}(t) \propto T^{\left(\frac{\delta_F}{\pi} - n\right)^2} e^{-\gamma_n t} e^{-i\omega_n t}. \quad (28)$$

Here, we introduced the exponential decay rates and frequencies

$$\begin{aligned} \gamma_n &= T \frac{(\delta_F - n\pi)^2}{\pi}, \\ \omega_n &= \Delta E + n\epsilon_F. \end{aligned} \quad (29)$$

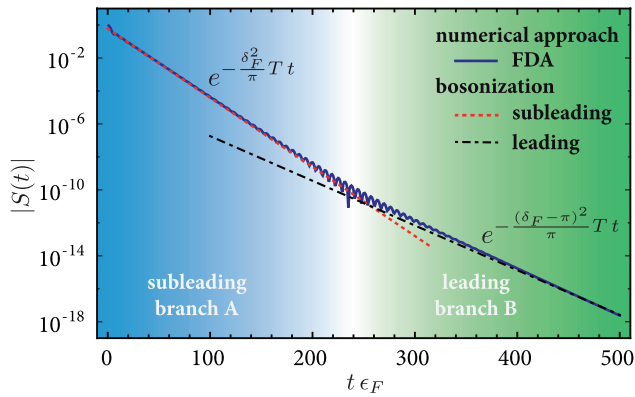


Figure 10. Crossover from subleading to leading branch dynamics. Absolute value of the Ramsey contrast $S(t)$ as function of time. Interaction parameters are chosen to correspond to the mixed regime (b) with $T/T_F = 0.1$, $1/k_F a = -0.61$, and $k_F r^* = 0.8$. The solid line shows the exact numerical evaluation of the dynamical overlap $S(t)$ using the FDA, while the dotted (dashed) line shows exponentials with exponents γ_1 (γ_0), respectively, which correspond to the leading (subleading) branch dynamics in this interaction regime. For the detailed dependence of the decoherence rates on $1/(k_F a)$, see figure 15.

Remarkably, equation (28) predicts a *prefactor* of the exponential decay which features a power-law dependence on temperature with an exponent governed by the OC $(\delta_F/\pi)^2$.

According to equations (17) and (19), $S(t)$ is given by a sum over various branch contributions. Out of those, the branch exhibiting the smallest decay coefficient γ_n , as determined by equation (29), will survive at long evolution times. This branch, which we call the ‘leading’ branch, determines the temperature scaling of the prefactor $\propto T^{(\frac{\delta_F}{\pi} - n)^2}$ in equation (28).

In table 1 we summarize our findings. In the column ‘low-T decay rate’ we list the decay rates γ_n which are applicable in the limit $T/\epsilon_F \ll 1$ (provided $tT \gg 1$ and $t\epsilon_F \gg 1$). Furthermore we show the definitions of the interaction regimes as well as the various contributions to the dephasing dynamics of the Ramsey signal $S(t)$.

For instance, according to equation (18), in the attractive regime (a) both $S_0^{(\text{FS})}(t)$ and $S_1^{(\text{FS})}(t)$ contribute. Since in this regime $\delta_F < \pi/2$, we find that $\gamma_0 < \gamma_1$. Therefore $S_A(t)$, which represents the attractive excitation branch, is leading. In contrast, in the mixed regime (b) $\gamma_1 < \gamma_0$ and hence the bottom-of-the-band contribution $S_B(t)$ is the leading branch. Finally, in the repulsive regime (c) both $S_{B1}(t)$ and $S_{B2}(t)$ are leading branches. They represent the dressed repulsive state branch and the edge of the molecule-hole continuum, respectively (see figure 6).

The actual time scale from which on the leading branch observably *dominates* the dynamics depends on the relative magnitudes of its coefficients $C_\alpha(T)$. For instance, in the mixed regime (b) the ‘bottom-of-the-band branch’ B is leading. However, its coefficient C_B can be numerically so small that for experimentally observable times the attractive branch A actually dominates the dynamics. This effect is shown in figure 10. Here a crossover between two exponential decay

rates can be seen in the Ramsey signal $S(t)$. For short and intermediate times, $S(t)$ exhibits an exponential decay with the ‘fast’, subleading decay rate γ_0 (dotted line). Only at long times $S(t)$ crosses over to the slower, leading decay rate γ_1 (dot-dashed line).

The fact that the fast decay of the subleading branch can dominate the short-time behavior demonstrates that, although the observed dynamics may naively seem to have reached quasi-classical behavior, quantum effects can still lead to long-time interference effects. The small signal at long times makes the experimental observation of this crossover between multiple exponential decoherence rates a challenge, similar to competing T_2 decay coefficients encountered in NMR spectroscopy [158, 159]. We note that in figure 10 we have chosen interaction parameters that allow us to demonstrate the crossover at long times. This choice leads to a very small Ramsey contrast in the crossover regime. In experiments more favorable interaction parameters can be chosen that lead to a substantially higher Ramsey contrast (as an example see figure F1 in appendix F).

Power-law temperature dependence. The power-law temperature dependence of the Fermi surface contributions given by equation (28) can be observed experimentally. One means to do so is to fit the asymptotic forms of $S(t)$ in equations (17) and (19) to the measured data of $S(t)$. To obtain unbiased results, the prefactor $T^{(\frac{\delta_F}{\pi} - n)^2}$ is absorbed in a rescaled definition of the coefficients

$$\tilde{C}_\alpha(T) = C_\alpha T^{(\frac{\delta_F}{\pi} - n)^2} \quad (30)$$

where C_α is a temperature independent constant. Studying the fit parameters $\tilde{C}_\alpha(T)$ as a function of temperature then allows one to reveal the intricate OC power-law dependence.

We demonstrate this fitting procedure for the three interaction regimes by numerically calculating the exact signal $S(t)$ shown in the upper panels of figure 11. This data is then fit by the respective asymptotic forms (17) and (19) using equations (21), (22) and (26) with rescaled coefficients $\tilde{C}_\alpha(T)$. The resulting fits of the complex $S(t)$ are shown as solid lines in figures 11(a)–(c) and they compare remarkably well with the exact data (symbols) down to relatively short times.

The scaling of the extracted coefficients \tilde{C}_α with temperature is shown in the lower panels of figure 11. Specifically, in figure 11(d) we study the attractive regime where the attractive branch A is leading. We find that the corresponding coefficient \tilde{C}_A universally follows the predicted power-law dependence. Furthermore, our analysis shows that the subleading coefficient $|\tilde{C}_B(T)|$ is numerically smaller than $|\tilde{C}_A(T)|$ so that the leading branch A will also dominate the decay of $S(t)$.

As an alternative to a fit of the full complex signal of $S(t)$, one may also fit directly the absolute value $|S(t)|$ to obtain the temperature scaling of \tilde{C}_α . In such a procedure, illustrated in figure 12, $|\tilde{C}_\alpha|$ as well as the decay exponent serve as fit parameters. The corresponding results are illustrated as open symbols in figure 11(d). This alternative procedure reveals that the temperature scaling of \tilde{C}_A , that is governed by the OC

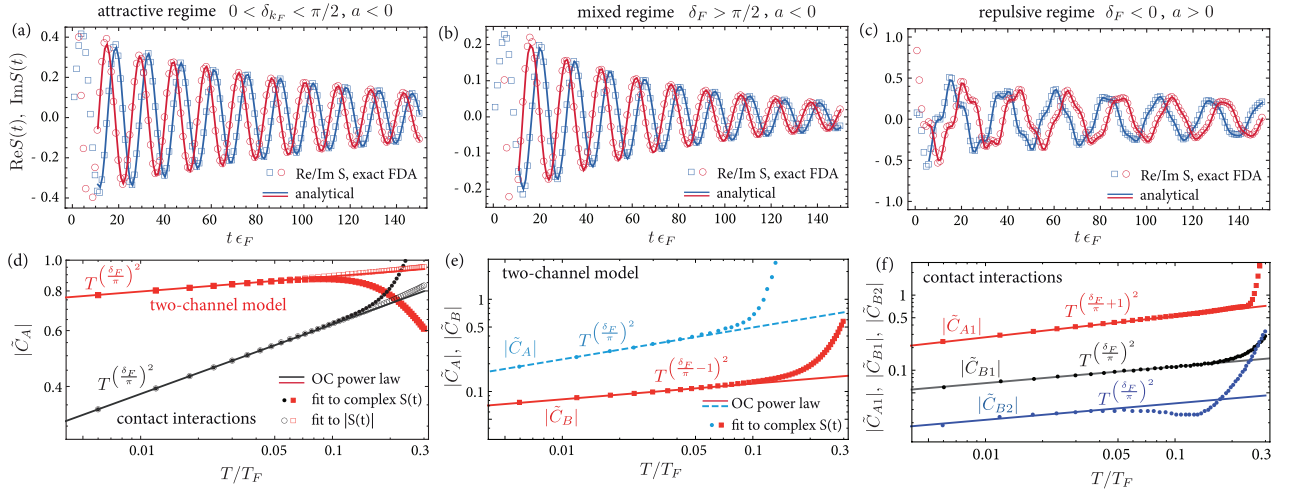


Figure 11. Power-low temperature dependence of dephasing dynamics. The upper panels (a-c) show the real and imaginary part of the Ramsey signal as calculated exactly using the FDA (symbols). The data, shown for the exemplary temperature $T/T_F = 0.012$, is fitted by the analytical expressions (17) and (19) (solid lines). The results are shown for parameters (a) $1/k_F a = -0.1$, $k_F r^* = 0$, (b) $1/k_F a = -0.5$, $k_F r^* = 0.8$ (c) $1/k_F a = 2$, $k_F r^* = 0$. In (d-f) the temperature dependence of the rescaled coefficients $\tilde{C}_\alpha(T)$ is shown where $\alpha = (A, B, A1, B1, B2)$ specifies the excitation branch. The parameters are: (d) $1/k_F a = -0.1$, $k_F r^* = 0$ (black) and $1/k_F a = -2$, $k_F r^* = 0.8$ (red), (e) $1/k_F a = -0.5$, $k_F r^* = 0.8$, (f) $1/k_F a = 0.1$, $k_F r^* = 0$. The open symbols in (d) correspond to an alternative fitting procedure, where the absolute value of $|S(t)|$ is fit by a single exponential decay function.

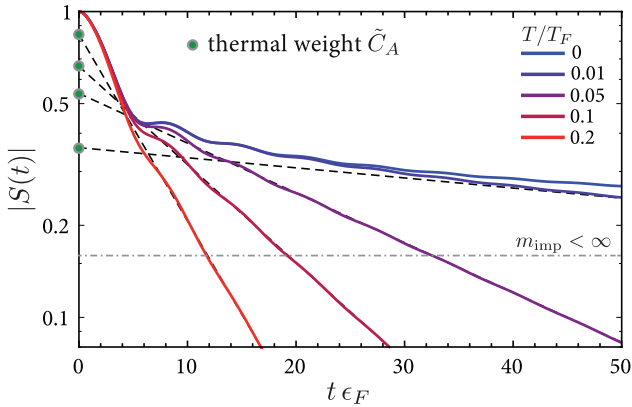


Figure 12. Thermal decay of the Ramsey signal and thermal weight. The Ramsey contrast $|S(t)|$ is shown for various temperatures at fixed interaction parameters $k_F a = -1.1$ and $k_F r^* = 0.8$. While at $T = 0$ the contrast decays to zero as a power-law, the decay is exponential at finite temperature. The dashed lines are exponential fits to the data and the points on the y-axis indicate the scaling behavior of the ‘thermal weights’ \tilde{C}_A (the fit for $T/T_F = 0.01$ involves data at times not shown in the plot). For an impurity of finite mass (e.g. $m_{\text{imp}}/m = 40/6$ for a ^{40}K impurity in a ^6Li Fermi gas), the decay of the Ramsey contrast would saturate at the finite polaron quasi-particle weight $Z = |S(t \rightarrow \infty)|$ at zero temperature (illustrated by the dot-dashed line).

exponent $(\frac{\delta_F}{\pi})^2$, can be observed up to temperatures as large as $T/T_F \approx 0.2$, making it accessible to current experimental technology.

Figure 11(e) shows the results in the mixed regime ($k_F r^* = 0.8$, $1/k_F a = -0.5$) for both coefficients $\tilde{C}_A(T)$ and $\tilde{C}_B(T)$. The dashed and solid curves show the predicted asymptotic power law behavior $\sim T^{(\frac{\delta_F}{\pi})^2}$ and $\sim T^{(\frac{\delta_F}{\pi}-1)^2}$, respectively. Although in this regime the bottom-of-the-band

branch B is formally leading, the corresponding coefficient $|\tilde{C}_B(T)|$ is numerically substantially smaller than $|\tilde{C}_A(T)|$. This finding reflects the crossover of exponential decay rates shown in figure 10: for limited observation time the decay with the subleading, and hence larger decay rate γ_0 will dominate. This demonstrates that in experiments performed in the mixed interaction regime one has to be careful in assigning thermal decoherence rates from early-time dynamics.

In the repulsive interaction regime the presence of the bound state leads to additional oscillations in the Ramsey signal. As can be seen in the upper panel figure 11(c) these oscillations are captured with remarkably high accuracy by the analytical expression equation (19) even at short times. In the lower panel figure 11(f) the temperature dependence of the corresponding rescaled Ramsey coefficients $\tilde{C}_\alpha(T)$ is shown. We find that up to high temperatures $T/T_F = 0.2$ the coefficient \tilde{C}_{A1} follows the power-law prediction (solid line). Similarly to the mixed interaction regime, it is again not the leading branches B1 and B2 which have the numerically largest values $|\tilde{C}_\alpha(T)|$. Instead, for the chosen interactions we find that the subleading bound-state branch $A1$ dominates the dephasing at short and intermediate times.

Relation to ion mobility in ^3He . Our results on the scaling of the coefficients $\tilde{C}_\alpha(T)$ allow us to draw connections to early work by Kondo and Soda [160] on ion mobility in ^3He . In their work Kondo and Soda studied the renormalization of a heavy ion due to its interaction with the fermionic quasiparticles in liquid ^3He . In this case, the ion Green’s function can be expressed as $G(\mathbf{q}, \omega) = Z(T)/[\omega - E_{\mathbf{q}} + i\Gamma(T)]$, which in the time domain becomes

$$G(\mathbf{q}, t) = Z(T)e^{-\Gamma t}e^{iE_{\mathbf{q}}t}. \quad (31)$$

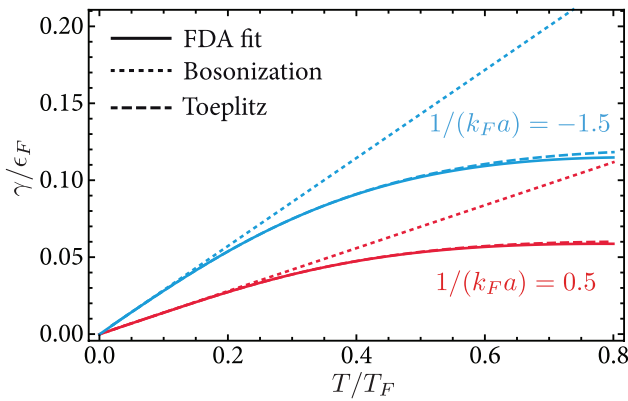


Figure 13. Decoherence rate at high temperatures. We compare theoretical predictions from bosonization and the Toeplitz-determinant approach to the numerically exact long-time decoherence rate of the Ramsey signal as function of temperature in the attractive and repulsive regime for $k_F r^* = 0.8$. The Toeplitz determinant approach gives very accurate results up to high temperatures, while bosonization starts to fail at $T/T_F \approx 0.15$.

Here E_p is the renormalized ion dispersion relation and $\Gamma(T)$ its quasiparticle lifetime. $Z(T)$ is the quasiparticle weight that determines the ion mobility $\mu \propto Z(T)^2$ [160].

Using a perturbative expansion, Kondo and Soda predicted the ion quasiparticle weight to scale as

$$Z(T) \propto \left(\frac{T}{T_F} \right)^{2V_0^2 \rho^2}. \quad (32)$$

Here V_0 is the microscopic contact coupling constant between the ion impurity and fermions of mass m , and ρ is the density of states at the Fermi surface. This scaling was predicted to be valid for temperatures $T_0 \ll T \ll T_F$, where $T_0 \equiv (m/M)T_F$ approaches zero as the ion mass M goes to infinity.

The expression for the ion Green's function equation (31) suggests a comparison with our prediction for the Fermi surface contribution to the impurity Green's function equation (28). Remarkably, the scaling of the prefactor, see equation (30) for $n = 0$, reproduces Kondo's scaling of the impurity quasiparticle weight in equation (32), in our case derived from an exact calculation.

Having this relation in mind, one may interpret the coefficients \tilde{C}_α as wave-function renormalizations that determine the temperature-dependent spectral weight of the respective excitation branches. As temperature goes to zero we predict this thermal weight to vanish according to a power law that is governed by the OC exponent, see figure 11. This behavior is illustrated in figure 12, where we show Ramsey contrast curves at various temperatures. Exponential fits to the long-time decoherence data, shown as dashed lines in figure 12, indicate that the weights of the exponential decays, shown as green dots, decrease with decreasing temperature. Simultaneously, the regime of quantum dephasing extends to longer times. In the limit of zero temperature, the thermal weight goes to zero and the thermal exponential decay of the Ramsey contrast is replaced by a power law with exponent $(\delta_F/\pi)^2$, characteristic of the Anderson OC. Remarkably, we find that each excitation branch is governed by its unique scaling exponent. While

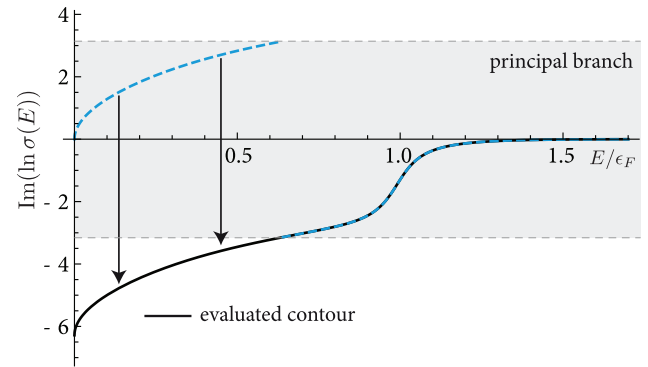


Figure 14. Evaluation of the Toeplitz determinant. For the evaluation of the Toeplitz determinant according to equation (33) the branch of the logarithm has to be analytically continued as illustrated by the black solid line. Here the imaginary part of the integrand $\ln \sigma(E)$ is shown as function of E for interaction parameters in the mixed interaction regime (b) with $1/k_F a = -0.5$, $k_F r^* = 0.8$, and $T/T_F = 0.114$.

in liquid Helium the measurement of subleading excitation branches is difficult, ultracold atoms allow not only for the verification of the power-law scaling equation (30) but also for the observation of subleading excitation branch dynamics.

We note that, while for an infinitely heavy impurity the thermal weight \tilde{C}_A goes to zero at $T = 0$, for a mobile impurity in three dimensions the Ramsey contrast will saturate at a finite quasi-particle weight $Z(T = 0) = S(t \rightarrow \infty)$ (illustrated by horizontal dash-dotted line in figure 12 [31, 32, 53, 60]). Here, the time scale for the crossover to many-body dynamics that is greatly affected by the impurity mass is expected to be approximately given by the inverse impurity recoil energy $E_{\text{rec}} \sim (2k_F)^2/(2M)$. However, both a detailed study of the behavior of the quasiparticle weight as function of the inverse impurity mass $1/M$ as well as the related many-body dynamics remain open questions which need to be addressed in future studies.

5.2.5. Toeplitz-determinant approach. In figure 13 we compare the temperature dependence of the leading branch decoherence rate γ_n as obtained from bosonization (dotted lines) with the exact numerical result (solid lines). We find that for sufficiently low temperatures both agree. However, as T/T_F is increased to values realized in current experiments, $T/T_F \approx 0.2$, deviations appear. The reason for the failure of the bosonization approach lies in the fact that at high temperatures, on the one hand, the energy dependence of the phase shift $\delta(E)$ has to be taken into account, and, on the other hand, the assumption of a linearized dispersion relation becomes invalid.

These effects can be taken into account in a quasi-classical approach motivated by the theory of the Toeplitz determinants [19, 161–165]. In this approach, many-body overlaps such as equation (12) are evaluated in a quasi-classical basis of wave packets localized both in coordinate space and momentum; for details we refer to appendix E. In this basis, the evolution operator in equation (10) is of a Toeplitz form, i.e. the kernel depends only on a time difference and, consequently, $S(t)$ can

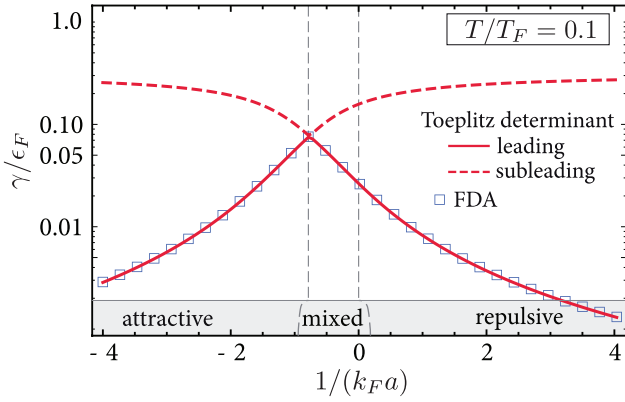


Figure 15. Dependence of decoherence rate on the interaction strength. The interaction dependent decoherence rate of $S(t)$ obtained from the exact FDA and Toeplitz determinant approach at $T/T_F = 0.1$ and $k_F r^* = 0.8$.

be expressed as a Toeplitz determinant. Such determinants were studied in various physical and mathematical context, and, applying these techniques, the asymptotic behavior of the Fermi-surface contributions at long times can be obtained (see, e.g. [22] for a related discussion in the context of full counting statistics).

Leading branch decoherence. The leading asymptotic behavior of Toeplitz determinants is given by the so-called Szegő formula, which allows us to map the calculation of the asymptotic Toeplitz determinant onto contour integrations, see e.g. [165]. By going to the frequency representation, in which the kernel operator in equation (10) is diagonal, one finds for the Fermi sea contributions (see appendix E)

$$S(t) = \exp \left(t \int_0^\infty \frac{dE}{2\pi} \ln \left[1 - n_F(E) + n_F(E) e^{2i\delta(E)} \right] \right), \quad (33)$$

where $n_F(E)$ is the Fermi occupation number.

In the evaluation of equation (33) the branch of the logarithm must be chosen so that the integrand analytically continues along the integration contour and tends to zero as $E \rightarrow \infty$. While in the attractive and repulsive interaction regime (a) and (c) one can remain in the principal branch of the logarithm, the mixed interaction regime (b) requires more care. Here the phase shift at the Fermi surface exceeds $\pi/2$ which requires to evaluate the integrand in equation (33) starting at low energies in the lower Riemann sheet and then analytically continue to the principal branch at high energies. This is illustrated in figure 14 where we show the imaginary part of the integrand of equation (33) along the integration contour.

Using this integration procedure, one obtains the oscillation frequency ω_L and the decay rate γ_L from

$$i\omega_L + \gamma_L = - \int_0^\infty \frac{dE}{2\pi} \ln [\sigma(E)], \quad (34)$$

where we defined the so-called ‘symbol’ of the Toeplitz determinant

$$\sigma(E) = 1 - n_F(E) + n_F(E) e^{2i\delta(E)}. \quad (35)$$

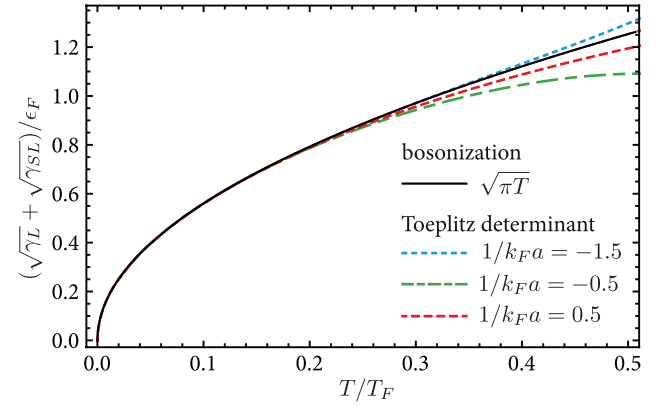


Figure 16. Universal scaling relations of decoherence rates. At low temperatures the decoherence rates of the leading and subleading branch obey the universal scaling relations equation (39) (solid line) which are independent of interaction strength and hold up to temperature $T/T_F \approx 0.2$ as can be seen from the comparison to the result from the Toeplitz determinant theory for three different interaction strengths and fixed $k_F r^* = 0.8$.

However, the values of ω_L and γ_L as obtained from equation (34) correspond only to the *leading* branch of the respective interaction regime (see figure 6): in regime (a) this is branch A, in regime (b) it is branch B, and in regime (c) these are the branches B1 and B2. Note that in the limit $T \rightarrow 0$, the integral (34) is easily computable and reproduces the results derived in the bosonization approach, equation (29).

Subleading branch decoherence. Calculating the frequencies and the decay rates for the subleading branch requires more effort. In the context of the theory of Toeplitz determinants, subleading branches were studied in the case of singular symbols $\sigma(E)$. In that case, the theory of subleading branches is known under the name of the generalized Fisher-Hartwig conjecture and all branches decay as power laws [162, 166, 167]. However, in our finite-temperature case, the decay is exponential, and the theory of Fisher-Hartwig singularities does not directly apply.

Still, the contribution of different excitation branches can be found from the following argument. Each branch contribution corresponds to a specific configuration of fermions (see figure 6) and should be an analytical functional of $\delta(E)$. Consequently, the subleading branch may be obtained as an analytical continuation from the regime where the corresponding contribution constitutes the leading branch and is given by equation (33). This analytical continuation technically amounts to a continuous deformation of the leading integration contour in equation (33) into a new contour \mathcal{C}_{SL} in the complex energy plane so that it never crosses any singularities of the integrand.

As discussed in detail in appendix G, we find that for each interaction regime an integration contour \mathcal{C}_{SL} can be chosen to give the desired subleading frequency and decay rate

$$i\omega_{SL} + \gamma_{SL} = - \int_{\mathcal{C}_{SL}} \frac{dE}{2\pi} \ln [\sigma(E)]. \quad (36)$$

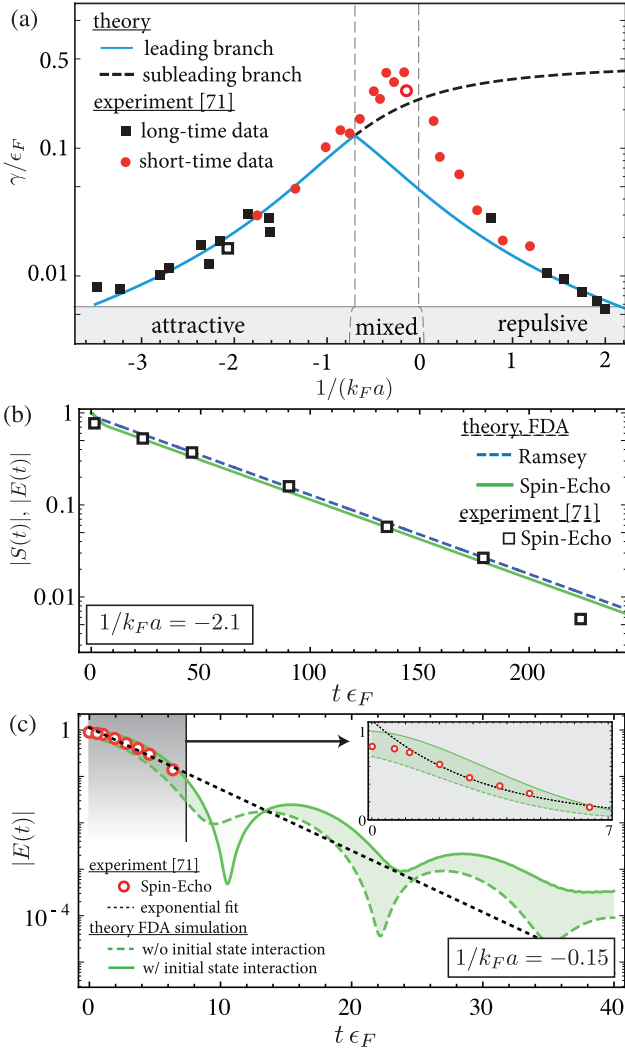


Figure 17. Decoherence rate: theory and experiment [71]. (a) Decoherence rate as function of interaction strength $1/k_F a$. The black symbols represent the experimentally measured decoherence rate of the spin-echo signal at long times while the red data points were extracted from exponential fits to the short-time dynamics. The theoretical predictions from FDA and Toeplitz determinant theory are shown as solid and dashed lines. They are obtained for experimental temperature $T/T_F = 0.16$ and rescaled resonance parameter $k_{F,r}^* = (40/46)^2 k_{F,r,\text{exp}}^* = 0.7$ [31]. (b) FDA simulation of the time-resolved responses (lines) and experimental data (symbols) for the interaction strength $1/k_F a = -2.1$, indicated by the open square in (a). The Ramsey and spin-echo response lead to the same exponential decay rate. (c) FDA simulation of the experimental spin-echo sequence at $T/T_F = 0.2$ and $1/k_F a = -0.15$, including finite pulse duration and initial state interaction. The dotted line is an exponential fit to the experimental data that leads to the open red circle in (a). The inset shows a zoom into short evolution times on a linear scale. The experimental data is taken from [71].

The specific contours are derived from an analysis of the analytical structure of the integrand $\ln \sigma(E)$ which is determined by the roots E_r of the symbol $\sigma(E)$,

$$\sigma(E_r) = 0, \quad (37)$$

in the complex energy plane. By choosing the appropriate integration contours one can show that the subleading decay rate and frequency are given by (see appendix G)

$$\begin{aligned} \gamma_{\text{SL}} &= \gamma_L + |\text{Im}E_r| \\ \omega_{\text{SL}} &= \omega_L - \text{sign}(\text{Im}E_r) \text{Re}E_r. \end{aligned} \quad (38)$$

In the low temperature limit $T \rightarrow 0$, $E_r = \epsilon_F + iT(\pm\pi + 2\delta_F)$ where the $-$ applies to the attractive and mixed regime (a) and (b) and $+$ holds for the repulsive regime (c). Then the result equation (38) indeed reproduces equation (29).

The analytical Toeplitz approach is in remarkable agreement with exact numerical results. In figure 13 we compare the temperature dependence of decoherence rate as obtained from the Toeplitz approach and the exact FDA calculation. The predicted rates, shown for two interaction regimes, are in excellent agreement up to temperatures as high as $T/T_F \approx 1$, where bosonization completely fails.

The virtue of the Toeplitz approach is further demonstrated in figure 15 where we show the interaction dependence of the decoherence rate. The rate of the leading (solid) and subleading branch (dashed) obtained from the Toeplitz approach compare remarkably well with the exact FDA results (symbols). But most importantly it also analytically predicts the rate of the subleading branch which can dominate the intermediate time evolution, see figure 10. As discussed below, this becomes particularly relevant for experiments in which very long time scales are inaccessible due to small Ramsey contrast.

5.3. Universal scaling relations

Within the bosonization approximation, the decay rates and frequencies for the leading and subleading branches obey simple scaling relations,

$$\sqrt{\gamma_L} + \sqrt{\gamma_{\text{SL}}} = \sqrt{\pi T}, \quad (39)$$

$$|\omega_L - \omega_{\text{SL}}| = \epsilon_F. \quad (40)$$

These relations are universal and do not depend on the particular form of the phase shift $\delta(E)$. Being derived from bosonization, they are valid in the limit of low temperature T , but remarkably, we find that finite- T corrections remain small up to rather high temperatures compared to T_F . This is illustrated in figure 16, where we compare the scaling of the decay rates obtained from the Toeplitz determinant approach to the prediction equation (39) for the various interaction regimes.

5.4. Comparison to experiments

The long-time thermal decoherence rate of impurities immersed in a Fermi gas has recently been measured [71]. The experiment was performed using a dilute sample of ^{40}K impurities immersed in a ^6Li Fermi gas, and the spin-echo decoherence rate was determined. The interaction between the impurities and the Fermi gas was characterized by a narrow Feshbach resonance of range $k_{F,r,\text{exp}}^* = 0.93$ and the temperature was $T/T_F = 0.16$. For relatively ‘weak’ interactions with $1/k_F a < -1.4$ and $1/k_F a > 0.8$ the loss in spin-echo contrast $|E(t)|$ was recorded up to long times $t\epsilon_F \approx 220$ and was fit to an exponential decay. In figure 17(a) the experimentally determined finite temperature decoherence rate is shown as

black squares. In this figure we also show our prediction from the FDA with the appropriately rescaled resonance parameter $k_{\text{F}}r^* = (40/46)^2 k_{\text{F}}r_{\text{exp}}^* = 0.7$ (see [31]) as the blue solid line. In this temperature regime the exact FDA agrees with the theory of Toeplitz determinants and we find full agreement with the experimental data (black squares).

In a complementary approach in [71, 115], the thermal decoherence rate of the spin-echo signal was calculated using Fermi liquid theory. In these works, which relied on an *a priori* assumed equivalence of the spin-echo and Ramsey signal, good agreement with experimental observation was found away from the Feshbach resonance. In the theoretical description, which applies to the weakly interacting regime [71], the inclusion of the decay of the repulsive polaron into the weakly bound molecular state was found to be important in the repulsive regime. This decay process was captured by adding a semi-phenomenological decay rate to the quasiparticle collision rate, obtained from Fermi liquid theory. Our results which are based on an exact solution, fully include all conversion processes between the repulsive polaron excitation branch and the molecular state. The excellent agreement of our prediction with the experimental data hence confirms the previous conjecture [71] that the inclusion of higher-order processes is crucial for an accurate description of the impurity dephasing dynamics.

Close to the Feshbach resonance, the experiment could not access the very long-time dynamics due to fast loss of spin-echo contrast. As a consequence, the data was measured only up to small times of $t\epsilon_{\text{F}} \approx 10$ and again fit to an exponential decay. The resulting, experimentally measured rates are shown as the red dots in figure 17(a). We find that in the mixed, as well as in the repulsive regime at strong interactions, it deviates from the FDA prediction.

Based on our previous discussion this discrepancy does, however, not come as a surprise, and we can identify two possible explanations for the deviations. First, in the repulsive and mixed regime, very long times have to be reached to observe the leading long-time decoherence rate, as here the subleading branch dominates the intermediate-time dynamics. In figure 17(a) we show the decoherence rate of the subleading branch as obtained from the theory of Toeplitz determinants as dashed line. We find that it agrees reasonably well with the observed enhanced decay rate in the mixed regime. This makes it plausible that the experiment may have observed the intermediate-time dynamics governed by the subleading branch. A second explanation for the deviations may be found in the fact that at the times accessible in the experiment oscillations originating from bottom-of-the-band excitations still influence the dynamics of the Ramsey and spin-echo contrast. Indeed these oscillations dominate the short and intermediate time dynamics in the strongly interacting regime, see e.g. figure F1 in appendix F. Only far beyond the thermal time scale $\tau_{\text{th}} = 1/T$ a pure exponential decay can be expected, and hence the experimental data may have been still strongly influenced by non-thermal quantum dynamics. Furthermore, while the Ramsey- and spin-echo response lead to equivalent decoherence rates at very long times, their signals can show very distinct behavior at short and intermediate times.

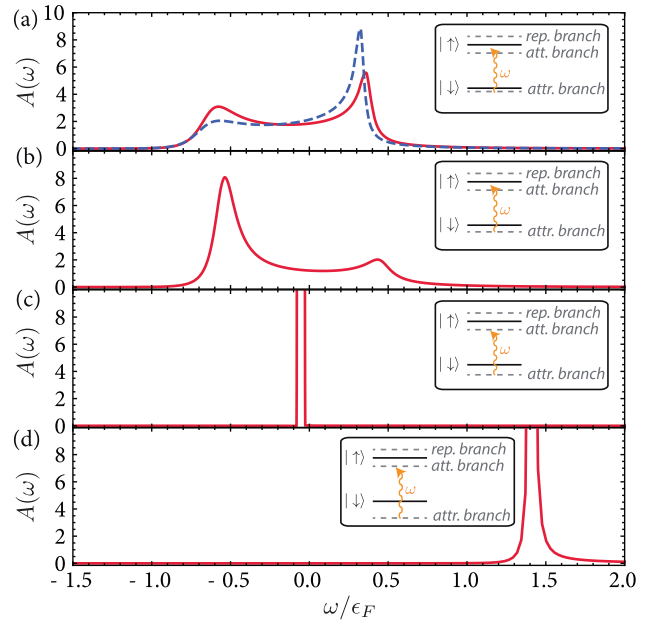


Figure 18. RF spectra for finite initial and final state interactions. RF spectrum for fixed final state interaction $1/k_{\text{F}}a_{\text{f}} = 0.05$ while the initial state interaction between the static impurity and the Fermi gas is varied: (a) $1/k_{\text{F}}a_{\text{i}} = -6$, (b) $1/k_{\text{F}}a_{\text{i}} = -2$, (c) $1/k_{\text{F}}a_{\text{i}} = -0.05$, (d) $1/k_{\text{F}}a_{\text{i}} = 2$. The temperature is given by $T/T_{\text{F}} = 0.1$ and $k_{\text{F}}r_{\text{i}}^* = k_{\text{F}}r_{\text{f}}^* = 0.8$ in both the initial and the final state.

To corroborate these arguments we have simulated the time-resolved signal for the experimental setup of [71] using the FDA and taking the experimental parameters as input. The results of our simulations for two representative interaction strengths (open symbols in figure 17(a)) are shown as curves in figures 17(b) and (c) where also the experimental, time-resolved data (symbols) for the spin-echo signal, as given in [71], is shown. For weak interaction, see figure 17(b), long evolution times were experimentally accessible. Here the theoretical simulation of the time-resolved spin-echo signal reveals that the experimental data is well described by an exponential, thermal decay with a decay rate that agrees with the experimental data.

This is in contrast to strong interactions, analyzed in figure 17(c). Here we simulate in detail the experimental sequence employed to obtain the red open data point in figure 17(a). To this end, we include the finite pulse duration $\tau_{\pi/2} = \tau_{\pi}/2 \approx 2.5/\epsilon_{\text{F}}$ of the spin-rotation pulses. Moreover, we simulate the fact that these pulses were performed at weak initial interaction $1/k_{\text{F}}a_{\text{in}}$ followed by a quench to the final interaction strength $1/k_{\text{F}}a_{\text{f}} = -0.15$. The details of the protocol are described in [31]. The green shaded area in figure 17(c) shows the simulated response for varying initial state interactions ranging from zero $1/k_{\text{F}}a_{\text{in}} = -\infty$ (solid), to intermediate interactions $1/k_{\text{F}}a_{\text{in}} = -2.25$ (dashed). The dotted black line is an exponential fit to the experimental data (symbols). From the simulation we find that independent of the initial state interaction, the dynamics is strongly influenced by bottom-of-the-band excitations that lead to pronounced oscillations in the signal. The comparison with the experimental

data (symbols) in figure 17(c) makes it thus plausible that the experiment may have probed an intermediate time regime at which the pure exponential late-time decay has not yet become apparent.

6. Universal short-time, high-frequency response

In the previous sections we have demonstrated that the combined use of the FDA, bosonization, and the theory of Toeplitz determinants allows us to obtain a precise analytical understanding of the dephasing dynamics of heavy impurities immersed in a Fermi gas at intermediate and long times. The analytical approaches provided an intuitive description of the universal long-time dynamics and hence low-frequency response in terms of a few relevant excitation branches. Here we turn to the short-time behavior of the Ramsey signal which is more conveniently studied in the corresponding high-frequency response. To this end we study the high-frequency absorption for a system where the impurities are interacting with the Fermi gas in both the initial and final state. Considering this scenario allows us to connect our predictions to universal analytical results obtained from a short-time operator product expansion [23].

6.1. RF response with finite initial and final state interactions

For many experimentally accessible atomic species interactions between the impurity and the Fermi gas are present both in the initial and final impurity spin state [168]. In this case the absorption spectrum is given by

$$A(\omega) = 2\text{Re} \int_0^\infty dt e^{i\omega t} \text{Tr}[e^{i\hat{H}_i t} e^{-i\hat{H}_f t} \hat{\rho}_i]. \quad (41)$$

Here \hat{H}_i (\hat{H}_f) is the initial (final) Hamiltonian of the system with initial (final) state scattering length a_i (a_f) and range r_i^* (r_f^*).

Based on equation (41) we study the influence of initial state interactions on the RF response as shown in figure 18. In this figure, we keep the final state interactions fixed at $1/k_F a_f = 0.05$ while varying the interaction $1/k_F a_i$ in the initial state. For weak initial state interactions (solid line in figure 18(a)), the spectrum is only slightly shifted with respect to the perfect reverse RF response (dashed line). However, as interactions in the initial state are increased, not only the spectrum is shifted further, but it also changes in shape, see figures 18(b)–(d).

When interactions in the initial and final state become comparably strong, see figure 18(c), the response approaches a δ -peak due to the symmetry between the initial and final state. Using this feature—when the initial and final state have the same scattering length, $a_i = a_f$, yet differ in the Feshbach resonance width—RF measurements on impurities provide a tool for the experimental determination of r^* .

6.2. Analytical high-frequency response

We now turn to the absorption response at high frequencies. As has been shown recently [23], the absorption behavior at

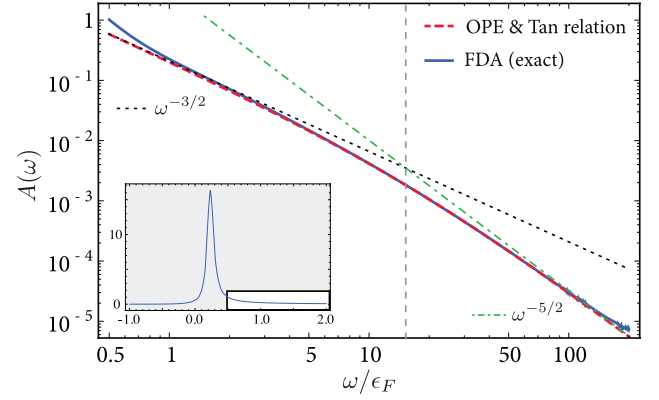


Figure 19. RF high-frequency tail. RF spectrum on double-logarithmic scale as function of frequency as obtained from FDA (blue solid) for contact interactions, $k_F r^* = 0$, where both finite initial and final state interactions are present with $1/k_F a_i = -0.5$, $1/k_F a_f = -4$. The black dotted (green dot-dashed) line shows the limiting $\omega^{-3/2}$ ($\omega^{-5/2}$) behavior. The red dashed line gives the analytical prediction from the operator product expansion, equation (44) [23], with the contact C calculated from the adiabatic theorem, equation (43). The inset shows the rf response including low frequencies.

high frequency can be related to seemingly unrelated quantities by so-called ‘Tan relations’ [25–28, 62, 169–176]. These relations apply to arbitrary two-component Fermi gases (the case of an impurity immersed in a Fermi gas is a special case), where the two fermion species interact with short-range potentials. For such gases the momentum distribution decays as [177]

$$n(\mathbf{k}) \rightarrow \frac{C}{k^4} \quad (42)$$

at large momenta $k = |\mathbf{k}|$. A decade ago, Tan discovered theoretically that the coefficient C , which has been termed the ‘contact’, is related to various quantities by simple, universal relations [25–27]. For instance, Tan’s adiabatic theorem states that the change of energy E of an arbitrary two-component Fermi gas interacting with contact interactions, due to a change of the interspecies scattering length a is determined by

$$\frac{dE}{d(1/a)} = -\frac{C}{8\pi\mu_{\text{red}}} \quad (43)$$

where $\mu_{\text{red}} = m_1 m_2 / (m_1 + m_2)$ is the reduced mass, and $m_{1,2}$ are the masses of the two fermion species. Similar formulas relate the contact C to the pressure, the density-density correlator, the virial theorem, and the inelastic two-body loss observed in such systems [25–28, 62, 172, 175, 176].

The contact C appears also in the RF absorption spectrum when final and initial state interactions are present. Using an operator product expansion (OPE) Braaten [23] predicted that at high frequencies the RF response follows

$$A(\omega) \rightarrow \frac{1}{4\pi(2\mu_{\text{red}}\omega^3)^{1/2}} \left(\frac{1}{a_i} - \frac{1}{a_f} \right)^2 \frac{C}{a_f^{-2} + 2\mu_{\text{red}}\omega} \quad (44)$$

where we have set the Rabi coupling $\Omega = 1$. The contact C depends on the initial state of the system, and hence in particular on the initial state scattering length a_i .

The Tan relations can be derived from operator identities and as such hold irrespectively of the state of the system. Only the contact C itself then depends on the state and has either to be measured experimentally or determined from first principle calculations which are a challenge for generic many-body problems. However, being valid for an arbitrary two-component Fermi gas, the Tan relations apply also to our case of heavy impurities immersed in a Fermi gas.

In figure 19 we show the high-frequency response of an impurity on a double logarithmic scale as obtained from the FDA (solid line). In this figure, both initial and final state contact interactions are present ($k_F a_i = -0.5$ and $k_F a_f = -4$). The inset shows the response on a linear scale including the polaron ‘peak’ at low frequencies. We find that the signal undergoes a crossover from a non-analytical $\omega^{-3/2}$ to $\omega^{-5/2}$ behavior. Having the exact numerical FDA solution we may now turn to the verification of equation (44). To this end, we first calculate the ground-state energy $E \equiv \Delta E$ as function of the scattering length a_i from equation (24). Using the adiabatic theorem, equation (43), we then determine the contact as function of a_i . The resulting function $C(a_i)$ serves as input into the OPE prediction equation (44) which has hence no free parameter (for an infinitely heavy impurity $\mu_{\text{red}} = m$, where m is the mass of the atoms in the Fermi gas). In figure 19 the resulting prediction is shown as red, dashed curve. We find that the analytical expression equation (44) describes with remarkable precision the exact RF response down to frequencies of the order of the Fermi energy. We note that we discussed here only the high-frequency response for contact interactions. The inclusion of a finite characteristic range r^* leads to the crossover to a modified power-law at frequencies $\omega \sim 1/(mr^{*2})$ [23, 172]. For a detailed discussion of the role of finite range interactions we refer to [32].

6.2.1. Relation to the long-time evolution. The RF absorption response $A(\omega)$ is related to the Ramsey signal $S(t)$ by Fourier transformation (see also appendix B). Accordingly, the high-frequency behavior of $A(\omega)$ including the contact C as given by equation (44), is naturally reflected in the *short-time* dynamics of $S(t)$. The Tan relations connect the high-frequency behavior, however, also to the *long-time* behavior of $S(t)$. To illustrate this, we focus on low temperatures and the attractive interaction regime.

As we have seen in section 5.2, in the attractive interaction regime the attractive polaron excitation branch A, and hence the Fermi surface contribution $S_{\text{FS}}^{(0)}$, dominates the long-time dynamics, see equations (17) and (18). Thus, at long times the phase evolution of the Ramsey signal follows $S(t) \sim e^{-i\Delta E t}$ (see equation (28)). Here ΔE is given by the attractive ‘polaron’ ground-state energy, which follows from Fumi’s theorem, equation (24). According to equation (28) the long-time phase evolution is approximately linear in time. Hence ΔE can be extracted relatively easily as function of the scattering length from experimental long-time data [31]. We note that a similar relation of the phase evolution of the Ramsey signal to the Tan contact C has recently been discussed also in an experimental study of the dephasing dynamics of the unitary Bose gas [178].

The ground-state energy of the system $E \equiv \Delta E$ can be used to calculate the contact C from the adiabatic theorem (43). Since the contact C is the only free parameter that enters the high-frequency tail in equation (44), one can predict the short-time (high-frequency) dephasing behavior of the corresponding Ramsey signal $S(t)$ from long-time dephasing dynamics.

7. Summary and outlook

We have studied the real-time and absorption response of impurities immersed in a Fermi sea. In cold atoms the interaction between the impurity and fermions can be controlled by Feshbach resonances and we showed that the system is described by an Anderson–Fano model. We found that three distinct interaction regimes can be identified that are universally determined by the phase shift at the Fermi surface. For each of these regimes we have computed the ‘standard’ and ‘reverse’ radio-frequency absorption spectra at both zero and finite temperature and calculated the real-time interferometric responses of the system exactly.

In each interaction regime we identified analytically excitation branches in the many-body Hilbert space which dominate the dynamics. While in the attractive and repulsive regime polaron-type excitations govern the dynamics, narrow Feshbach resonances allow one to additionally address a novel ‘mixed regime’ where ‘bottom-of-the-Fermi sea’ excitations dominate the dynamics. This regime is special in exhibiting a quantum-interference-induced crossover in the decoherence dynamics at times much larger than the thermal time scale $\hbar/k_B T$.

We have analyzed the competition between quantum dephasing and thermal decoherence in the real-time response of the system. The former leads to a power-law decay of coherence up to a time scale set by the inverse temperature, while the latter gives rise to exponential decoherence. Using bosonization and Toeplitz determinant theory, we obtained analytic predictions for the intermediate to long-time response, which only depend on the scattering phase shift and temperature but not on the trajectory of the impurity spin. As a consequence, Ramsey and spin-echo interferometry exhibit the same decoherence rates at long times and we predicted that the maximum decoherence rate is given by $\pi k_B T/4$.

Moreover, in analogy to earlier results on ion mobility in liquid ^3He we find that at finite temperatures a finite spectral weight can be assigned to the various excitation branches that depends as a power-law on temperature. As temperature approaches zero, this weight vanishes as $\propto T^\alpha$, with α being related to the OC critical exponent.

In the present work we have considered the problem of an infinitely heavy impurity coupled to a Fermi gas. Extending on our exact solution, one may study the fate of the Anderson orthogonality catastrophe as the mass of the impurity becomes finite. This problem is still lacking a definite solution in low dimensions [9, 179–182], and experiments with ultracold atoms, where the mass of the impurity can be tuned using state selective optical potentials [183, 184], may shed light on this outstanding problem. To address this question theoretically, the

functional determinant approach can be extended to account for Hamiltonians beyond bilinear order. In this way also interactions in the bath can be accounted for, as of relevance for a wide set of impurity problems in condensed matter physics. The inclusion of higher-order terms is expected to become of particular relevance when considering low dimensional systems where enhanced quantum effects can lead to striking non-equilibrium dynamics [185–190], or when studying externally driven systems [191–195]. Similarly, higher-order effect will become important as the impurity concentration is increased. In this case bath-mediated interactions will modify the many-body dynamics of the system. The detailed study of such effects remains an open challenge.

While the real-time Ramsey interferometry signal corresponds to the Fourier transform of the reverse radio-frequency response, more complicated interferometric measurements do not have a simple conjugate response [73]. As an example we discussed spin-echo interferometry, yet, more complex protocols from nuclear-magnetic resonance can be envisioned, not only as a probe of many-body physics but also for controlling and manipulating many-body wave functions. Augmenting this technique with parameter ramps, one can adiabatically prepare many-body states and consequently probe them similar to pump-probe experiments in ultra-fast spectroscopy [196].

Moreover, in recent experiments exotic states of matter have been created in non-equilibrium transient regimes [191, 192, 197, 198]. In these experiments, physics is probed on scales ranging from long times to short times on the order of the Fermi time $\sim \hbar/\epsilon_F$. In light of these developments a detailed account of the short- to long-time dynamics becomes increasingly important for our theoretical understanding of new frontiers of condensed matter physics. In this respect cold atomic systems provide a well-controlled starting point where dynamics can find a universal description on extended time scales as compared to traditional solid state systems. The description of dynamics in terms of excitation branches, put forward in this work, may provide a means to devise powerful variational wave functions that take into account most relevant parts of Hilbert space, and allow one to account for the interplay of few- and many-body physics far from equilibrium.

Acknowledgments

We thank Michael Jag and the group of Rudolf Grimm for providing the experimental data and Dima Abanin, Rudolf Grimm, Zoran Hadzibabic, Atac Imamoglu, Jesper Levinsen, Ivan Levkivskyi, Meera Parish, Yulia Shchadilova, Tarik Yefsah, Wilhelm Zwerger, and Martin Zwierlein for interesting and fruitful discussions. Parts of this work were inspired by Adilet Imambekov and Aditya Shashi. We acknowledge support from Harvard-MIT CUA, NSF Grant No. DMR-1308435, AFOSR Quantum Simulation MURI, AFOSR grant number FA9550-16-1-0323. RS is supported by the NSF through a grant for the Institute for Theoretical Atomic, Molecular, and Optical Physics at Harvard University and the Smithsonian Astrophysical Observatory. MK acknowledges support from the Technical University of Munich—Institute

for Advanced Study, funded by the German Excellence Initiative and the European Union FP7 under grant agreement 291763, and the DFG grant No. KN 1254/1-1. The research of DAI was supported by the Swiss National Foundation through the NCCR QSIT. J-SY is supported by the Ministry of Science and Technology, Taiwan (Grant No. MOST 104-2917-I-564-054). MC was supported by the Austrian Science Fund FWF within the SFB FoQuS (F40-P04).

Appendix A. Exact single-particle wavefunctions in the two-channel model

We calculate exactly the single-particle wavefunctions of model (5). We use the Ansatz $|\Psi\rangle = \alpha_m|m\rangle + |\psi\rangle$ to solve the Schrödinger equation $\hat{H}|\Psi\rangle = E|\Psi\rangle$ which gives (in units $\hbar = 2m = 1$)

$$\epsilon_m \alpha_m + g \int d^3r \chi(r) \psi(r) = E \alpha_m \quad (\text{A.1a})$$

$$g \chi(r) \alpha_m - \nabla^2 \psi(r) = E \psi(r), \quad (\text{A.1b})$$

where $\chi(r) = e^{-r/\rho}/4\pi\rho^2 r$ is the form factor defined in the main text. These equations can be solved by choosing

$$\alpha_m = \text{const.} \quad (\text{A.2a})$$

$$\psi(r) = A \frac{\sin kr + \delta_k}{r} + B \chi(r), \quad (\text{A.2b})$$

where the phase shift δ_k is a function of k . This leads to the following equations

$$E = k^2 \quad (\text{A.3a})$$

$$\alpha_m = \frac{Ag}{\rho} \frac{k\rho \cos \delta_k + \sin \delta_k}{(k^2 - \epsilon_m)(1 + k^2\rho^2) - \frac{g^2}{8\pi\rho}} \quad (\text{A.3b})$$

while normalization requires

$$1 = \alpha_m^2 + 2\pi A^2 R \left(1 + \frac{\sin 2\delta_k}{2kR}\right) + \frac{g^2 \rho \alpha_m^2}{8\pi(1 + k^2\rho^2)^2} + 2Ag\rho\alpha_m \frac{k\rho \cos \delta_k + \sin \delta_k}{(1 + k^2\rho^2)^2}. \quad (\text{A.4})$$

Together these equations determine the unknown coefficients A , B , and α_m .

Next, we calculate k and δ_k from the boundary conditions set by constraining the atoms to a spherical box of radius R which yields

$$kR + \delta_k = n\pi. \quad (\text{A.5})$$

This result is then compared to the scattering phase shift δ_k as obtained from continuum scattering solution for the two-channel model (5) [84],

$$f(k) = \frac{\mu_{\text{red}}}{2\pi\hbar^2} g^2 \chi(\mathbf{k})^2 \left[-\frac{\hbar^2 k^2}{2\mu_{\text{red}}} + \epsilon_m - \frac{g^2 \mu_{\text{red}}}{4\pi\hbar^2 \rho [1 - ik\rho]^2} \right]^{-1}, \quad (\text{A.6})$$

where we made factors of \hbar and the reduced mass μ_{red} explicit. Using the low energy expansion of $f(k)$ one readily identifies

the microscopic parameters of our model as discussed in [31, 84] and given in equation (6). Note within our model the effective range is given by $r_e = -2r^* + 3\rho - 4\rho^2/a$ which reduces to $r_e = -2r^*$ for small values of ρ as stipulated in the main text.

Appendix B. Relation between $S(t)$ and $A(\omega)$

In this appendix we prove the simple statement that the time-dependent Ramsey signal $S(t)$ and the frequency-resolved absorption spectrum $A(\omega)$ are related by Fourier transformation. The absorption response is given by Fermi's Golden Rule equation (7) (see. also the $T = 0$ limit in equation (14)). After inserting the Fourier representation of the delta distribution and using that $|\psi_i\rangle$ and $|\psi_\alpha\rangle$ are many-body eigenstates of \hat{H}_0 and \hat{H} , respectively (i.e. $\hat{H}_0|\psi_i\rangle = E_i|\psi_i\rangle$ and $\hat{H}|\psi_\alpha\rangle = E_\alpha|\psi_\alpha\rangle$) this equation can be rewritten as

$$\begin{aligned} A(\omega) &= \int_{-\infty}^{\infty} dt \sum_{i,\alpha} \langle \psi_i | \hat{\rho}_{\text{FS}} e^{i\hat{H}_0 t} | \psi_\alpha \rangle \langle \psi_\alpha | e^{-i\hat{H} t} | \psi_i \rangle e^{i\omega t} \\ &= \int_{-\infty}^{\infty} dt \text{Tr} \left[\hat{\rho}_{\text{FS}} e^{i\hat{H}_0 t} e^{-i\hat{H} t} \right] e^{i\omega t}. \end{aligned} \quad (\text{B.1})$$

This can be conveniently reexpressed as

$$A(\omega) = 2\text{Re} \int_0^{\infty} dt' \text{Tr} \left[\hat{\rho}_{\text{FS}} e^{i\hat{H}_0 t'} e^{-i\hat{H} t'} \right] e^{i\omega t'} \quad (\text{B.2})$$

where we used that $\hat{\rho}_{\text{FS}}$, \hat{H} , and \hat{H}_0 are hermitian. The integrand contains the overlap $S(t)$:

$$S(t) = \text{Tr}[\hat{\rho}_{\text{FS}} e^{i\hat{H}_0 t} e^{-i\hat{H} t}] \quad (\text{B.3})$$

that is experimentally obtained for positive times $t \geq 0$ from the Ramsey signal. The function $S(t)$ at negative times can be inferred from $S(-t) = S^*(t)$. Hence the absorption spectrum is directly obtained from the Fourier transform of the Ramsey signal. From equation (B.1) now simply follows also the reverse statement: multiplication of equation (B.1) by $e^{-i\omega t}/2\pi$ and integration over all frequencies yields

$$\begin{aligned} \int_{-\infty}^{\infty} \frac{d\omega}{2\pi} A(\omega) e^{-i\omega t} &= \int_{-\infty}^{\infty} \frac{d\omega}{2\pi} \int_{-\infty}^{\infty} dt' e^{i\omega(t'-t)} \text{Tr}[\hat{\rho}_{\text{FS}} e^{i\hat{H}_0 t'} e^{-i\hat{H} t'}] \\ &= \int_{-\infty}^{\infty} dt' S(t') \delta(t' - t) = S(t) \end{aligned} \quad (\text{B.4})$$

which shows that the complex Ramsey signal $S(t)$ can be directly calculated from the Fourier transform of the absorption spectrum $A(\omega)$.

Appendix C. Fumi's theorem

Here we give a short illustrative derivation of Fumi's theorem [1] for the case of an immobile impurity that interacts with contact interactions with a surrounding Fermi gas at zero temperature and in three dimensions. Specifically, we consider here the attractive ground state of the system at $a < 0$, but the generalization to the repulsive state as well as the inclusion of the bound state for $a > 0$ is straightforward.

Consider the impurity being localized at $\mathbf{r} = 0$ in a spherical box of radius R (see appendix A). Only s-wave states have to be considered and the radial single-particle wave functions in absence of the impurity potential are given by $u_n(r) \sim \sin(n\pi r/R)$ with n the nodal quantum number. In presence of the scattering potential the wave functions acquire a scattering phase shift and are given by $v_n(r) \sim \sin(k_n r + \delta_n)$ where the wave number k_n is determined from the boundary condition equation (A.5) and we introduced $\delta_n \equiv \delta_{k_n}$.

The energy of the many-body state of interest is obtained by filling the single-particle states with fermions up to the Fermi energy. The single-particle energies in the non-interacting case are $\epsilon_n = (n\pi/R)^2/2m$ while in the presence of the scattering potential they are given by $\tilde{\epsilon}_n = \frac{1}{2m} (n\pi - \delta_n/R)^2$. In the attractive interaction regime this leads to a downward shift of single-particle levels. The 'interacting' ground state energy of the attractive state (with respect to the non-interacting ground state) is given by summing over all single-particle energy shifts $\Delta\epsilon_n \equiv \tilde{\epsilon}_n - \epsilon_n$ up to the Fermi energy

$$E = \sum_n \Delta\epsilon_n = -\frac{2\pi}{R^2} \sum_n n \delta_n. \quad (\text{C.1})$$

In the second equation we used the fact that $\delta_n^2 \ll 2n\pi|\delta_n|$ is a good approximation since $|\delta_n|$ is bound by π . In the limit $R \rightarrow \infty$ we may now replace the sum over n by an energy integration using $\Delta E_n \equiv \epsilon_n - \epsilon_{n-1} = (2n-1)(\pi/R)^2$. For large box sizes R , states with small n lie at very small energies for which the phase shift is negligible. Thus we can take $\Delta E_n = 2n(\pi/R)^2$. From this follows now directly the continuum limit of equation (C.1):

$$\begin{aligned} E &= -\frac{2\pi}{R^2} \sum_n n \delta_n = -\frac{1}{\pi} \sum_n 2 \underbrace{\left(\frac{\pi}{R}\right)^2}_{\Delta E_n} n \delta_n \\ &\stackrel{R \rightarrow \infty}{=} - \int_0^{\epsilon_F} \frac{dE}{\pi} \delta(E). \end{aligned} \quad (\text{C.2})$$

In 'repulsive regime' one has $a > 0$ and a molecular bound state with finite binding energy ϵ_B is present in the single-particle spectrum. If one is interested in the repulsive state the bound state remains unoccupied and equation (C.2) directly applies. To obtain, however, the energy E_{mol} for the ground state in this regime in which the molecule is occupied with a fermion, the molecular binding energy $\epsilon_B < 0$ has to be added to equation (C.2).

Appendix D. Technical details on bosonization

D.1. Fermi-surface contribution

The problem of a three-dimensional Fermi sea coupled to a static impurity scattering potential reduces for s-wave scattering effectively to a one-dimensional problem in a semi-infinite space ($r > 0$). Furthermore, at sufficiently low temperatures one can linearize the spectrum near the Fermi surface so that one obtains right and left moving fermions. If one unfolds the coordinate axis one can map left moving fermions at $r > 0$ onto right moving fermions at $r < 0$, thus arriving at the

model of one-dimensional ‘chiral’ fermions [4]. Denoting the annihilation operator of the chiral fermions as $\psi(x)$, the effective Hamiltonian then can be expressed as

$$H_0 = -iv_F \int dx \psi^\dagger(x) \partial_x \psi(x), \quad (\text{D.1})$$

$$H_{\text{int}} = \int dx V_0(x) \psi^\dagger(x) \psi(x), \quad (\text{D.2})$$

where $V_0(x)$ is a scattering potential around $x = 0$ (we assume that the impurity is infinitely heavy). Using the standard bosonization approach, we rewrite the problem in terms of a bosonic field $\phi(x)$ [4, 19, 29],

$$\psi(x) \propto e^{i\phi(x)}, \quad (\text{D.3})$$

with the commutator

$$[\phi(x), \phi(x')] = i\pi \text{Sign}(x - x'). \quad (\text{D.4})$$

At long times, the short-range structure of the potential $V_0(x)$ may be ignored, with the effect of the scattering incorporated in the scattering phase δ_F :

$$H_0 = \frac{v_F}{4\pi} \int dx (\partial_x \phi(x))^2, \quad (\text{D.5})$$

$$H_{\text{int}} = -\frac{v_F \delta_F}{\pi} \partial_x \phi(0) + \Delta E, \quad (\text{D.6})$$

where

$$\Delta E = - \int_0^{\epsilon_F} \frac{dE}{\pi} \delta(E) \quad (\text{D.7})$$

is the total energy shift due to the impurity (this relation is known as Fumi’s theorem, see appendix C). Then $S(t)$ can be calculated as

$$\begin{aligned} S(t) &= \langle e^{iH_0 t} e^{-i(H_0 + H_{\text{int}})t} \rangle = e^{-i\Delta E t} \left\langle \exp \left[i \frac{v_F \delta_F}{\pi} \int_0^t dt' \partial_x \phi(0, t') \right] \right\rangle_{H_0} \\ &= e^{-i\Delta E t} \left\langle \exp \left[i \frac{\delta_F}{\pi} (\phi(0, t) - \phi(0, 0)) \right] \right\rangle_{H_0} \propto e^{-i\Delta E t} \left(\frac{\pi T}{\sinh \pi T t} \right)^{\left(\frac{\delta_F}{\pi}\right)^2}. \end{aligned} \quad (\text{D.8})$$

In the second step we used the linearized dispersion and replaced the time derivative by a spacial derivative $v_F dt' \rightarrow dx$, which allows us to easily evaluate the integral in the exponent.

D.2. Bottom-of-the-band and bound-state contributions

The bottom-of-the-band and bound-state effects are associated with intermediate states where a particle is moved from the bottom of the Fermi sea (or from the bound state) to the Fermi level, see figure 6. Such contributions were discussed in [73, 128] and here we extend those results. We start with the case of the bottom-of-the-band contribution.

The contribution to $S(t)$ from the intermediate states with one isolated hole deep inside the Fermi sea can be written as

$$S'(t) = \int \frac{dk}{2\pi} \sum_{\tilde{m}'} \left| \langle \text{FS} | \tilde{\psi}_k | \tilde{m}' \rangle \right|^2 e^{-iE_{\tilde{m}'} t + i(E_k - \epsilon_F) t}, \quad (\text{D.9})$$

where $|\text{FS}\rangle$ is the ground state of the free Hamiltonian H_0 , $|\tilde{m}'\rangle$ are the eigenstates of the Hamiltonian *with* scattering $H_0 + H_{\text{int}}$ *without* any holes deep under the Fermi surface (only with particle-hole excitations around the Fermi level) and *with one extra particle* compared to the state $|\text{FS}\rangle$. Furthermore $\tilde{\psi}_k$ is the annihilation operator for the single-particle eigenstate of the scattering Hamiltonian with the momentum k close to the bottom of the Fermi sea, $E_{\tilde{m}'}$ is the multi-particle energy of the state $|\tilde{m}'\rangle$ (relative to the ground-state energy of H_0), E_k is the single-particle energy of $\tilde{\psi}_k$ measured from the bottom of the Fermi sea, and ϵ_F is the Fermi energy.

We can further expand $\tilde{\psi}_k$ in terms of the free-Hamiltonian states ψ_k :

$$\langle \tilde{m}' | \tilde{\psi}_k^\dagger | \text{FS} \rangle = \int \frac{dk'}{2\pi} \langle \tilde{m}' | \psi_{k'}^\dagger | \text{FS} \rangle \langle \psi_{k'} | \tilde{\psi}_k \rangle. \quad (\text{D.10})$$

The overlap matrix elements can be computed as

$$\begin{aligned} \langle \psi_{k'} | \tilde{\psi}_k \rangle &= 4 \int_0^\infty \sin(k'x) \sin(kx + \delta(E_k)) dx \\ &= \frac{4k'}{k'^2 - k^2} \sin \delta(E_k) \approx \frac{4}{k_F} \sin \delta(E_k), \end{aligned} \quad (\text{D.11})$$

where $\delta(E_k)$ is the scattering phase at the energy E_k and we have used $k \ll k_F \approx k'$.

Combining everything together and performing integration over k' in equation (D.10), we find

$$S'(t) = \frac{16}{k_F^2} \int \frac{dk}{2\pi} \sin^2 \delta(E_k) e^{iE_k t} \left\langle e^{iH_0 t} \psi(0) e^{-i(H_0 + H_{\text{int}})t} \psi^\dagger(0) \right\rangle e^{-i\epsilon_F t}, \quad (\text{D.12})$$

where the last average can now be understood in the linearized model of chiral fermions discussed in the previous section. The important property of the above expression is that it factorizes into the bottom-of-the-Fermi-sea and Fermi-surface contributions.

The first factor due to the bottom-of-the-Fermi-sea can be re-expressed, using the quadratic dispersion relation $E_k = k^2/(2m)$ as

$$S_{-1}^{(\text{FB})}(t) = \frac{4}{k_F} \int_0^\infty \frac{dk}{2\pi} \sin^2 \delta(E_k) e^{iE_k t} = \frac{1}{\pi} \int_0^\infty \frac{dE}{\sqrt{E\epsilon_F}} \sin^2 \delta(E) e^{iEt}. \quad (\text{D.13})$$

Here we extended integration to infinity, assuming $T \ll \epsilon_F$ and $t \gg \epsilon_F^{-1}$. The time dependence of $S_{-1}^{(\text{FB})}(t)$ at large t is determined by the behavior of the integrand around $E = 0$. Since $\delta(E) \propto k \propto \sqrt{E}$ at $E \rightarrow 0$, we find that

$$S_{-1}^{(\text{FB})}(t) \propto t^{-3/2} \quad (\text{D.14})$$

at very large t . Close to the resonance ($|\epsilon_B| = (2m|a|^2)^{-1} \ll \epsilon_F$), there is an intermediate regime $\epsilon_F^{-1} \ll t \ll |\epsilon_B|^{-1}$. At such times, we may approximate $\delta(E) \approx \pi/2$ in the integral, which gives

$$S_{-1}^{(\text{FB})}(t) \propto t^{-1/2}. \quad (\text{D.15})$$

The second factor in equation (D.12) is the Fermi-surface contribution. It can be calculated using the bosonization approach:

$$\begin{aligned}
S_1^{(\text{FS})}(t) &= \frac{4}{k_F} \left\langle e^{iH_0 t} \psi(0) e^{-i(H_0 + H_{\text{im}})t} \psi^\dagger(0) \right\rangle e^{-i\epsilon_F t} \\
&= \frac{4}{k_F} e^{-i\Delta E t - i\epsilon_F t} \left\langle \exp \left[i \left(\frac{\delta_F}{\pi} - 1 \right) (\phi(0, t) - \phi(0, 0)) \right] \right\rangle_{H_0} \\
&\propto e^{-i\Delta E t - i\epsilon_F t} \left(\frac{\pi T}{\sinh \pi T t} \right)^{\left(\frac{\delta_F}{\pi} - 1 \right)^2}.
\end{aligned} \tag{D.16}$$

The case of the bound-state contribution can be treated in a similar way. The only difference will be the overlap matrix element $\langle \psi_{k'} | \tilde{\psi}_{\text{BS}} \rangle$ (here $\tilde{\psi}_{\text{BS}}$ is the wave function of the bound state), which will contribute to the overall prefactor in the bound-state term (21).

Appendix E. Asymptotic long-time response

E.1. Finite temperature

In this section, we derive the exponential decay of the Ramsey signal $S(t)$ at finite temperature at long times $t\epsilon_F \gg 1$:

$$S(t) \sim \exp(-\gamma t - i\omega t). \tag{E.1}$$

Furthermore, we will show that the decay rate is identical for the spin-echo and Ramsey protocols.

Our derivation is inspired by the Toeplitz-determinant technique used in full counting statistics for linearized dispersion relations [19, 164] and resembles the Szegő formula for Toeplitz determinants. However, here we go beyond the Toeplitz-determinant approximation and take into account both the energy-dependence of the scattering phase and the nonlinear dispersion relation.

The Ramsey overlap is given by

$$S(t) = \det \hat{B}; \quad \hat{B} = 1 - \hat{n} + \hat{n} e^{i\hat{h}_0 t} e^{-i\hat{h} t}, \tag{E.2}$$

where \hat{h}_0 and \hat{h} are the *single-particle* Hamiltonians without and with scattering potential, respectively.

Since the scattering potential is spherically symmetric, we can perform a partial wave expansion, and due to the low energies involved, we need to consider s-wave scattering only. We then use the standard approach to express the radial part of the scattering wave function $\Psi(r)$ by

$$u(r) = r\Psi(r) \tag{E.3}$$

where $r > 0$ and $u(r)$ fulfills the radial boundary condition $u(0) = 0$. Outside of the scattering potential $u(r)$ takes the form

$$u(r) \propto \sin[kx + \delta(E)], \tag{E.4}$$

where $\delta(E)$ is the scattering phase shift and $E = k^2/2m$ the scattering energy.

The key observation for calculating the determinant (E.2) is that the operator \hat{B} acts nearly diagonally on quasiclassical wave packets localized both in momentum and coordinate space. For example we can use the Gaussian wave packets

$$u_{k_0, r_0}^{(0)}(r) = (2\pi)^{-1/4} \Delta_r^{-1/2} \exp \left[ik_0 r - \frac{(r - r_0)^2}{4\Delta_r^2} \right]. \tag{E.5}$$

where Δ_r determines the width of the wave packet in real space. From its Fourier transform it follows that the wave packet is localized in momentum space around the momentum k_0 with width Δ_r^{-1} .

There are three time/energy scales in the problem: the inverse Fermi energy ϵ_F^{-1} , the evolution time t , and the ‘collision time’ $\tau_{\text{col}} = \partial\delta(E)/\partial E$ (this time is typically of the order of ϵ_F^{-1} or smaller, but becomes large at the bottom of the Fermi sea). Our further discussion assumes that the wave packets (E.5) propagate quasiclassically and simply acquire an extra phase when scattering. This requires that the wave packets are sufficiently localized in coordinate space so that the time t fulfills

$$E^{-1} \ll \frac{\Delta_r}{v} \ll t \tag{E.6}$$

where $v \equiv |v(k_0)|$ is given by the group velocity $v(k_0) = \frac{\partial E}{\partial k} \Big|_{k_0}$ of the wave packet. We impose the condition (E.6) at the Fermi surface (with $E = \epsilon_F$ and $v = v_F$), which implies $t \gg \epsilon_F^{-1}$. The condition (E.6) would break down close to the bottom of the Fermi sea, but we can make this region arbitrarily small for large t . Additionally, we require that the phase shift does not change much across the energy window of the wave packet, which implies

$$\tau_{\text{col}} \ll \frac{\Delta_r}{v}. \tag{E.7}$$

For the same reason as above, we require this condition only at the Fermi energy (which, in turn, implies the applicability condition $t \gg \tau_{\text{col}}$).

To properly take into account the boundary conditions on the function $u(r)$, we consider anti-symmetrized superposition of wave packets

$$u_{k_0, r_0}(r) = u_{k_0, r_0}^{(0)}(r) - u_{-k_0, -r_0}^{(0)}(r). \tag{E.8}$$

These form an overcomplete set on $r > 0$ with the completeness relation ($r, r' > 0$)

$$\int_{-\infty}^{+\infty} \frac{dk_0}{2\pi} \int_0^\infty dr_0 u_{k_0, r_0}(r) u_{k_0, r_0}^*(r') = \delta(r - r'). \tag{E.9}$$

The two time evolution operators in \hat{B} in equation (E.2) propagate the wave packets forward and backward in time. Neglecting residual diffusion of the wave packet due to the short range interaction potential (which is a good approximation for small collision times, see (E.7)), \hat{B} acts approximately diagonally on the wave packets:

$$\hat{B} u_{k_0, r_0}(r) \approx u_{k_0, r_0}(r) \begin{cases} 1 & -v(k_0)t < r_0, \\ 1 + n(E(k_0))(e^{2i\delta(E(k_0))} - 1) & -v(k_0)t > r_0. \end{cases} \tag{E.10}$$

Here we made use of the condition (E.7), i.e. we assume the wave packet is sufficiently localized in momentum space around momentum k_0 , so that phase shift is approximately constant across the wave packet’s energy window.

Using the completeness relation (E.9) and equation (E.10), we can compute

$$\begin{aligned}
\ln S(t) &= \text{tr} \ln \hat{B} = \int_{-\infty}^{+\infty} \frac{dk_0}{2\pi} \int_0^\infty dr_0 \theta(-r_0 - v(k_0)t) \\
&\quad \ln \left[1 + n(E(k_0))(e^{2i\delta(E(k_0))} - 1) \right] \\
&= \int_{-\infty}^0 \frac{dk_0}{2\pi} \frac{\partial E}{\partial k_0} t \ln \left[1 + n(E(k_0))(e^{2i\delta(E(k_0))} - 1) \right] \\
&= t \int_0^\infty \frac{dE}{2\pi} \ln \left[1 + n(E)(e^{2i\delta(E)} - 1) \right], \tag{E.11}
\end{aligned}$$

where a small correction due to the normalization of equation (E.8) is assumed to be negligible. The result (E.11) is equation (33) from the main text which determines γ and ω .

In particular,

$$\gamma = -\text{Re} \int_0^\infty \frac{dE}{2\pi} \ln \left[1 + n(E)(e^{2i\delta(E)} - 1) \right]. \tag{E.12}$$

Our derivation above generalizes the Toeplitz-determinant approach commonly used in full-counting statistics (see, e.g. [165] and references therein). The conventional Toeplitz-determinant approach usually assumes a linearized spectrum, which results in the operator \hat{B} being a Toeplitz matrix, and equation (E.11) resulting from the Szegő theorem. In our derivation, we relax the assumption of a linear dispersion relation, however \hat{B} may still be loosely thought of as a Toeplitz matrix, if we label states by their arrival time $\tau = r_0/v(k_0)$ at the scatterer. With this relation in mind, we continue to call our method the ‘Toeplitz-determinant approach’, keeping the corresponding terminology of the Szegő formula for equation (E.11) and ‘symbol’ for the argument of the logarithm in it.

Repeating the same calculation for the case of the spin-echo response,

$$E(t) = \det \hat{C}; \quad \hat{C} = 1 - \hat{n} + \hat{n}e^{i\hbar_0 t/2} e^{i\hbar t/2} e^{-i\hbar_0 t/2} e^{-i\hbar t/2}, \tag{E.13}$$

we find

$$\hat{C} u_{k_0, r_0}(r) \approx u_{k_0, r_0}(r) \begin{cases} 1 & -v(k_0)t < r_0, \\ 1 + n(E(k_0))(e^{-2i\delta(E(k_0))} - 1) & -v(k_0)t/2 < r_0 < -v(k_0)t, \\ 1 + n(E(k_0))(e^{2i\delta(E(k_0))} - 1) & -v(k_0)t/2 > r_0, \end{cases} \tag{E.14}$$

which leads to

$$\begin{aligned}
\gamma_{\text{SE}} + i\omega_{\text{SE}} &= -\frac{1}{2} \int_0^\infty \frac{dE}{2\pi} \left\{ \ln[1 + n(E)(e^{2i\delta(E)} - 1)] \right. \\
&\quad \left. + \ln[1 + n(E)(e^{-2i\delta(E)} - 1)] \right\}. \tag{E.15}
\end{aligned}$$

It is straightforward to check that $\omega_{\text{SE}} = 0$ and γ_{SE} reduces to equation (E.12), i.e. the Ramsey and spin-echo decoherence rates are equal.

Generalizing these derivations, we find that the decoherence rate γ does generally not depend on the trajectory of the impurity spin (on the Bloch sphere), i.e. arbitrarily many spin-echos with corresponding time partitions as in equation (E.13)

also yield the same result. Hence different trajectories give rise to the same exponential decay in the thermal long-time regime.

E.2. Zero temperature

At zero temperature, dephasing of the many-body wave function leads to a power-law decay of the dynamic Ramsey and spin-echo response [73]. The power-law decay can be attributed to the creation of infinitely many particle-hole excitations at the Fermi level which gradually renders the many-body wave function orthogonal to the original Fermi sea. We note that the exponential decay rate γ which we evaluated in the previous section for finite temperature tends asymptotically to zero with temperature, see equation (29). Approaching zero temperature logarithmic corrections to equation (E.1) will emerge giving rise to the power-law decay. Using the mapping onto a Riemann–Hilbert problem, introduced in [13] to solve generic time-dependent perturbations to the Fermi sea, we calculate the power law exponent for both Ramsey and spin echo protocols, see also [73].

We first study the Ramsey response equation (10) and define $R(\lambda, \tau)$ as the time diagonal element of equation (E.10), which dominates the asymptotic dynamics, to the power of an auxiliary parameter λ

$$R(\lambda, \tau) = \begin{cases} 1, & \text{if } t < \tau \\ e^{2i\lambda\delta_F}, & \text{otherwise.} \end{cases} \tag{E.16}$$

The asymptotic behavior of the Ramsey signal can be obtained from [13]

$$\ln S(t) \sim \frac{i}{2\pi} \int_0^\lambda d\lambda \int_0^t d\tau \frac{d \ln Y(\tau + i0)}{d\tau} \frac{d \ln R(\lambda, \tau)}{d\lambda}, \tag{E.17}$$

where $Y(z)$ solves the Riemann–Hilbert problem

$$Y(t - i0^+)Y(t + i0^+)^{-1} = R(\lambda, t). \tag{E.18}$$

The function $Y(z)$ is analytic everywhere in the complex plane except for the interval $[0, t]$ and can be obtained from

$$\ln Y(z) = \frac{1}{2\pi i} \int \frac{\ln R(\lambda, z')}{z - z'} dz'. \tag{E.19}$$

For $R(\lambda, \tau)$ given by equation (E.16), we obtain

$$\ln Y(z) = \frac{\lambda\delta_F}{\pi} \ln \frac{z}{z-t}. \tag{E.20}$$

In the vicinity of the branch points of Y at 0 and t we cut off the integral equation (E.17) at the Fermi energy ϵ_F of the problem which amounts to replacing $i0^+$ by $i\epsilon_F^-$. Computing the integral gives

$$S(t) \sim (i\epsilon_F t)^{-\delta_F^2/\pi^2}, \quad (\text{E.21})$$

which is the well known result for the asymptotic behavior of $S(t)$ [11, 13].

For the spin-echo response equation (11), $R_{\text{SE}}(\lambda, \tau)$ is obtained from equation (E.14)

$$R_{\text{SE}}(\lambda, \tau) = \begin{cases} e^{2i\lambda\delta_F} & t > 2\tau \\ e^{-2i\lambda\delta_F} & 2\tau > t > \tau \\ 1 & \text{otherwise} \end{cases} \quad (\text{E.22})$$

yielding

$$\ln Y_{\text{SE}}(z) = \frac{\lambda\delta_F}{\pi} \ln \frac{z(z-t)}{(z-t/2)^2}. \quad (\text{E.23})$$

With that we can evaluate equation (E.17)

$$\ln S_{\text{SE}}(t) \sim -\frac{1}{2} \frac{\delta_F^2}{\pi^2} \left(\int_0^{t/2} d\tau - \int_{t/2}^t d\tau \right) \frac{d}{d\tau} \ln \frac{z(z-t)}{(z-t/2)^2} \sim -3 \frac{\delta_F^2}{\pi^2} \ln(i\epsilon_F t) \quad (\text{E.24})$$

and thus we find for the asymptotic behavior of the spin-echo response

$$S_{\text{SE}}(t) \sim (i\epsilon_F t)^{-3\delta_F^2/\pi^2}. \quad (\text{E.25})$$

At zero temperature, the spin-echo exponent is therefore enhanced by a factor 3 as compared to the Ramsey exponent, which demonstrates the importance of quantum interference effects.

Appendix F. Bi-exponential crossover

The measurement of the crossover of exponential decay rates of the Ramsey signal $S(t)$ from subleading- to leading-branch dynamics can be an experimental challenge due to small Ramsey contrast. In figure 10 in the main text, we have shown an example where the crossover takes place at relatively long times t . There, the parameters were chosen so that oscillations due to bottom-of-the band excitations at short times are damped out in the crossover regime. At the correspondingly long times, the Ramsey contrast $|S(t)|$ became inaccessibly small for experiments.

However, the precise time at which the crossover takes place, as well as the corresponding magnitude of the Ramsey signal, is highly sensitive to the specific interaction parameters chosen. Hence, more favorable Ramsey contrast can easily be achieved by choosing only slightly modified parameters. For instance, in figure F1 we show the Ramsey contrast where, compared to figure 10, the temperature is increased from $T/T_F = 0.1$ to $T/T_F = 0.2$ and where $k_{\text{F}r^*}$ is changed from 0.8 to 1.1. This slight variation already yields an increase of the Ramsey contrast in the interference region by six orders of magnitude. This demonstrates that parameters can be optimized to bring the observation of the subleading to leading branch dynamics within reach of experimental precision.

Appendix G. Subleading branches of Toeplitz determinants

As outlined in section 5, analytical expressions for the different branches of the Fermi-surface contribution $S_n^{(\text{FS})}(t)$ may

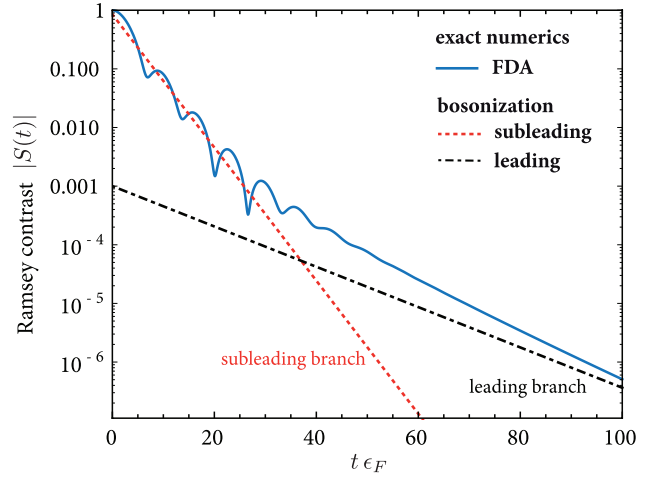


Figure F1. Crossover from subleading to leading branch dynamics. Ramsey contrast $|S(t)|$ as function of time. Interaction parameters are chosen to correspond to the mixed regime (b). Compare to figure 10, we choose slightly different parameters, $T/T_F = 0.2$, $1/k_{\text{F}a} = -0.61$, and $k_{\text{F}r^*} = 1.1$. The solid line shows the exact numerical evaluation of the dynamical overlap $S(t)$ using the FDA, while the dotted (dashed) line shows exponentials with the analytically predicted exponents γ_1 (γ_0), see equation (29).

be obtained by choosing different integration contours \mathcal{C}_{SL} in equation (36), which, for convenience, we state here again,

$$i\omega_{\text{SL}} + \gamma_{\text{SL}} = - \int_{\mathcal{C}_{\text{SL}}} \frac{dE}{2\pi} \ln [\sigma(E)], \quad (\text{G.1})$$

where, using the explicit form of Fermi distribution function, the symbol $\sigma(E)$ is given by

$$\sigma(E) = 1 - n(E) + n(E)e^{2i\delta(E)}. \quad (\text{G.2})$$

The derivation of the contours follows from an argument based on analytic continuation: the leading branch is given by the Szegő formula, leading to equation (34), while the subleading branch can be obtained by analytically continuing contours from a neighboring interaction regime where the corresponding branch is leading.

First, we consider the *leading* branches. In the upper panels of figure G1, we show as solid lines the contours for the evaluation of the leading branch in the three interaction regimes (a)–(c) (according to table 1). The corresponding trajectories of $\sigma(E)$ in the complex plane are shown in the lower panels of figure G1 as a function of the real variable E ranging from 0 to ∞ (assuming low temperature $T \ll \epsilon_F$). In the regimes (a) and (c), those trajectories do not encircle zero, and the asymptotics of the corresponding Toeplitz determinant follows from the conventional Szegő formula. In other words, the leading branch $S_0^{(\text{FS})}(t)$ is given by equation (34) with the usual integration along the real axis.

At the transition between the regimes (b) and (c), only scattering deeply below the Fermi surface is modified. Therefore we deduce that the leading branch in the regime (b) is also given by an integration along the real axis. As discussed in section 5.2.5, the branch of the logarithm is continued analytically along the contour, with the boundary condition $\log(\sigma(E \rightarrow \infty)) = 0$. In the interaction regime (b) we denote

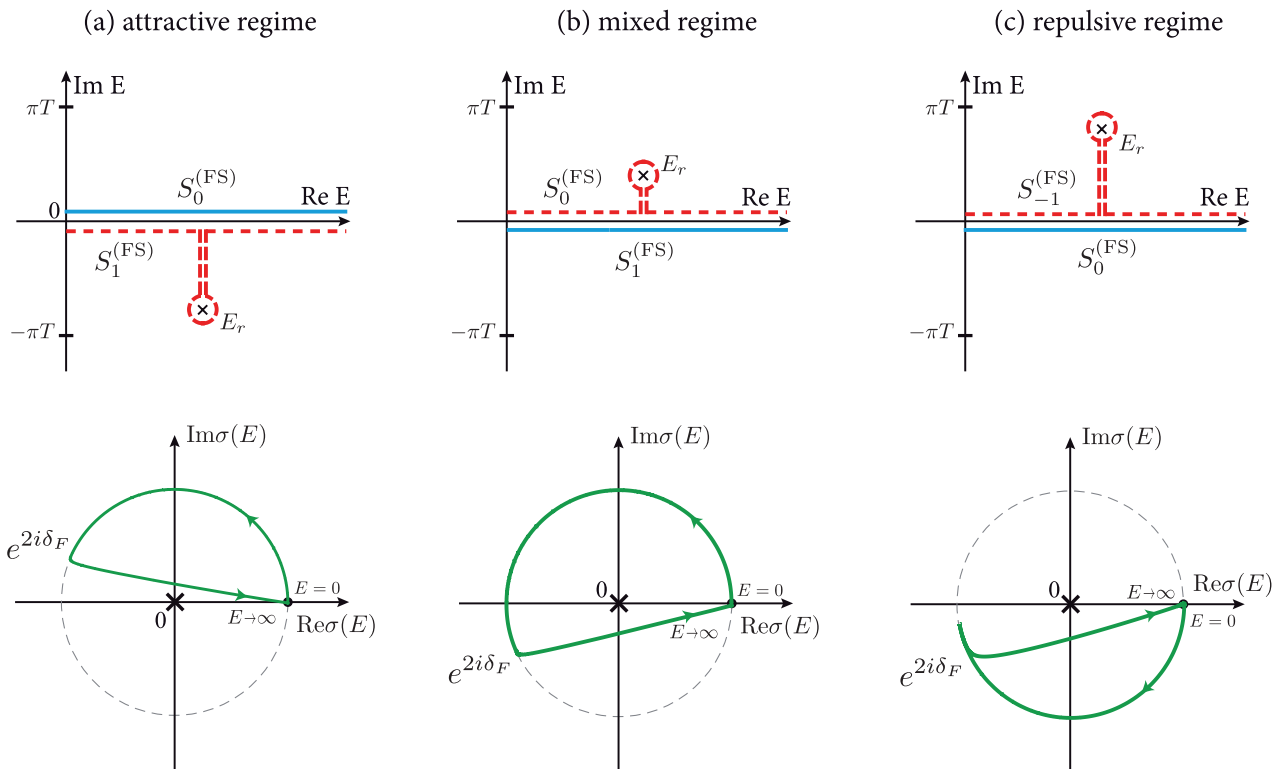


Figure G1. Integration contours for the evaluation of the Toeplitz determinant. The upper panel shows the integration contours in the complex variable E for the leading (solid lines) and subleading (dashed lines) branches in equations (34) and (36) for the three interaction regimes in table 1. The cross marks the logarithmic branching point E_r of the integrand. The lower panels schematically show the trajectories of $\sigma(E)$ in the complex plane (solid lines) for the leading branch as E spans the range from 0 to ∞ . Low temperature $T \ll \epsilon_F$ is assumed.

the leading branch as $S_1^{(\text{FS})}(t)$. This change of notation with respect to the leading branch contribution $S_0^{(\text{FS})}(t)$ in regimes (a) and (c) reflects that on passing from the regime (c) to the regime (b), we re-integrate the empty bound or bottom of the band state (see figure 6) into a hole near the bottom of the Fermi sea: as a consequence, the state without an extra particle at the Fermi surface in the regime (c) is interpreted as a state with one extra particle at the Fermi surface in the regime (b), hence the nomenclature $S_1^{(\text{FS})}(t)$. Note that the physical oscillation frequency is indeed continuous across the transition: while the shift of $\delta(E)$ by π (see figure 3) leads to a decrease of ω_L by ϵ_F , this energy is compensated by an additional contribution of ϵ_F from the hole at the bottom of the Fermi sea.

We now turn to the *subleading* branches. In order to obtain the corresponding integration contours, we examine first the transition between the regimes (a) and (b). At this transition, a zero E_r of $\sigma(E)$ (and hence a logarithmic branching point of the integrand) crosses the real axis of E . The analytical continuity of the branches prescribes that they may be obtained by the same integrals (36), but with the contours deformed to accommodate for the shift of the zero of $\sigma(E)$, so that the integrand stays continuously on the same branch of the logarithm. In this way, we find the subleading branch in the regime (b) as a continuation of the leading branch in the regime (a) and the subleading branch in the regime (a) as a continuation of the leading branch in the regime (b). The corresponding integration contours for the subleading branches are shown in the upper panels of figure G1 as dashed lines: they deviate from

the real axis to go around the zero of $\sigma(E)$ (and end up on a different branch of the logarithm, with respect to the integrand for the leading branch of their respective interaction regime). Finally, the subleading branch in the regime (c) is given by the same type of contour as in the regime (b) for the same reason as for the leading branch. For the calculation of integrals for the subleading branches, leading to the expressions equation (38), the contour deviations from the real axis can be chosen to be perpendicular to it, so that the contour retraces itself on the way back, as shown in figure G1. The universal jump of the logarithm of $2\pi i$ between the two branches then yields the result (38).

ORCID iDs

Richard Schmidt  <https://orcid.org/0000-0003-2776-269X>
 Michael Knap  <https://orcid.org/0000-0002-7093-9502>
 Dmitri A Ivanov  <https://orcid.org/0000-0001-6903-0679>

References

- [1] Mahan G D 2000 *Many Particle Physics* (New York: Kluwer)
- [2] Onsager L 1944 Crystal statistics. 1. A two-dimensional model with an order-disorder transition *Phys. Rev.* **65** 117–49
- [3] Bethe H 1931 Zur Theorie der Metalle *Z. Phys.* **71** 205–26
- [4] Giamarchi T 2004 *Quantum Physics in One Dimension* (Oxford: Oxford University Press)
- [5] Kitaev A 2003 Fault-tolerant quantum computation by anyons *Ann. Phys.* **303** 2–30

- [6] Kitaev A 2006 Anyons in an exactly solved model and beyond *Ann. Phys.* **321** 2–111
- [7] Dicke R H 1954 Coherence in spontaneous radiation processes *Phys. Rev.* **93** 99
- [8] Weiss U 1999 *Quantum Dissipative Systems* vol 10 (Singapore: World Scientific)
- [9] Rosch A 1999 Quantum-coherent transport of a heavy particle in a fermionic bath *Adv. Phys.* **48** 295–394
- [10] Anderson P W 1967 Infrared catastrophe in Fermi gases with local scattering potentials *Phys. Rev. Lett.* **18** 1049–51
- [11] Nozières P and De Dominicis C T 1969 Singularities in the x-ray absorption and emission of metals. III. One-body theory exact solution *Phys. Rev.* **178** 1097
- [12] Nozières P 1994 The effect of recoil on edge singularities *J. Phys. I* **4** 1275
- [13] d’Ambrumenil N and Muzykantskii B 2005 Fermi gas response to time-dependent perturbations *Phys. Rev. B* **71** 045326
- [14] Schweigert I V and Mukamel S 2007 Coherent ultrafast core-hole correlation spectroscopy: x-ray analogues of multidimensional nmr *Phys. Rev. Lett.* **99** 163001
- [15] Shah J 2013 *Ultrafast Spectroscopy of Semiconductors and Semiconductor Nanostructures* vol 115 (New York: Springer)
- [16] Bloch I, Dalibard J and Zwerger W 2008 Many-body physics with ultracold gases *Rev. Mod. Phys.* **80** 885–80
- [17] Braaten E and Hammer H-W 2006 Universality in few-body systems with large scattering length *Phys. Rep.* **428** 259–390
- [18] Chin C, Grimm R, Julienne P and Tiesinga E 2010 Feshbach resonances in ultracold gases *Rev. Mod. Phys.* **82** 1225–86
- [19] Levitov L S, Lee H and Lesovik G B 1996 Electron counting statistics and coherent states of electric current *J. Math. Phys.* **37** 4845–66
- [20] Klich I 2003 *Full Counting Statistics: an Elementary Derivation of Levitov’s Formula* (Dordrecht: Kluwer)
- [21] Schönhammer K 2007 Full counting statistics for noninteracting fermions: exact results and the levitov-lesovik formula *Phys. Rev. B* **75** 205329
- [22] Ivanov D A and Abanov A G 2013 Fisher-Hartwig expansion for Toeplitz determinants and the spectrum of a single-particle reduced density matrix for one-dimensional free fermions *J. Phys. A: Math. Theor.* **46** 375005
- [23] Braaten E, Kang D and Platter L 2010 Short-time operator product expansion for rf spectroscopy of a strongly interacting Fermi gas *Phys. Rev. Lett.* **104** 223004
- [24] Nishida Y 2012 Probing strongly interacting atomic gases with energetic atoms *Phys. Rev. A* **85** 053643
- [25] Tan S 2008 Energetics of a strongly correlated Fermi gas *Ann. Phys.* **323** 2952–70
- [26] Tan S 2008 Large momentum part of a strongly correlated Fermi gas *Ann. Phys.* **323** 2971–86
- [27] Tan S 2008 Generalized virial theorem and pressure relation for a strongly correlated Fermi gas *Ann. Phys.* **323** 2987–90
- [28] Braaten E and Platter L 2008 Exact relations for a strongly interacting Fermi gas from the operator product expansion *Phys. Rev. Lett.* **100** 205301
- [29] Gogolin A O, Nersisyan A A and Tselik A M 2004 *Bosonization and Strongly Correlated Systems* (Cambridge: Cambridge University Press)
- [30] Sidler M, Back P, Cotlet O, Srivastava A, Fink T, Kroner M, Demler E and Imamoglu A 2017 Fermi polaron-polaritons in charge-tunable atomically thin semiconductors *Nat. Phys.* **1** 255–61
- [31] Cetina M *et al* 2016 Ultrafast many-body interferometry of impurities coupled to a Fermi sea *Science* **354** 96–9
- [32] Parish M M and Levinsen J 2016 Quantum dynamics of impurities coupled to a Fermi sea *Phys. Rev. B* **94** 184303
- [33] Chevy F 2006 Universal phase diagram of a strongly interacting Fermi gas with unbalanced spin populations *Phys. Rev. A* **74** 063628
- [34] Lobo C, Recati A, Giorgini S and Stringari S 2006 Normal state of a polarized Fermi gas at unitarity *Phys. Rev. Lett.* **97** 200403
- [35] Pilati S and Giorgini S 2008 Phase separation in a polarized Fermi gas at zero temperature *Phys. Rev. Lett.* **100** 030401
- [36] Combescot R, Recati A, Lobo C and Chevy F 2007 Normal state of highly polarized Fermi gases: simple many-body approaches *Phys. Rev. Lett.* **98** 180402
- [37] Punk M, Dumitrescu P T and Zwerger W 2009 Polaron-to-molecule transition in a strongly imbalanced Fermi gas *Phys. Rev. A* **80** 053605
- [38] Prokof’ev N and Svistunov B 2008 Fermi-polaron problem: diagrammatic Monte-Carlo method for divergent sign-alternating series *Phys. Rev. B* **77** 020408
- [39] Prokof’ev N V and Svistunov B V 2008 Bold diagrammatic Monte-Carlo: a generic sign-problem tolerant technique for polaron models and possibly interacting many-body problems *Phys. Rev. B* **77** 125101
- [40] Mora C and Chevy F 2009 Ground state of a tightly bound composite dimer immersed in a Fermi sea *Phys. Rev. A* **80** 033607
- [41] Bruun G M and Massignan P 2010 Decay of polarons and molecules in a strongly polarized Fermi gas *Phys. Rev. Lett.* **105** 020403
- [42] Parish M M 2011 Polaron-molecule transitions in a two-dimensional Fermi gas *Phys. Rev. A* **83** 051603
- [43] Mathy C J M, Parish M M and Huse D A 2011 Trimers, molecules, and polarons in mass-imbalanced atomic Fermi gases *Phys. Rev. Lett.* **106** 166404
- [44] Zöllner S, Bruun G M and Pethick C J 2011 Polarons and molecules in a two-dimensional Fermi gas *Phys. Rev. A* **83** 021603
- [45] Levinsen J and Parish M M 2013 Bound states in a quasi-two-dimensional Fermi gas *Phys. Rev. Lett.* **110** 055304
- [46] Massignan P, Zaccanti M and Bruun G M 2014 Polarons, dressed molecules and itinerant ferromagnetism in ultracold Fermi gases *Prog. Phys.* **77** 034401
- [47] Trefzger C and Castin Y 2012 Impurity in a Fermi sea on a narrow Feshbach resonance: a variational study of the polaronic and dimeronic branches *Phys. Rev. A* **85** 053612
- [48] Massignan P, Bruun G M and Stoof H T C 2008 Spin polarons and molecules in strongly interacting atomic Fermi gases *Phys. Rev. A* **78** 031602
- [49] Combescot R and Giraud S 2008 Normal state of highly polarized Fermi gases: full many-body treatment *Phys. Rev. Lett.* **101** 050404
- [50] Combescot R, Giraud S and Leyronas X 2009 Analytical theory of the dressed bound state in highly polarized Fermi gases *Europhys. Lett.* **88** 60007
- [51] Schmidt R, Enss T, Pietilä V and Demler E 2012 Fermi polarons in two dimensions *Phys. Rev. A* **85** 021602
- [52] Nikolić P and Sachdev S 2007 Renormalization-group fixed points, universal phase diagram, and $1n$ expansion for quantum liquids with interactions near the unitarity limit *Phys. Rev. A* **75** 033608
- [53] Schmidt R and Enss T 2011 Excitation spectra and rf response near the polaron-to-molecule transition from the functional renormalization group *Phys. Rev. A* **83** 063620
- [54] Kroiss P and Pollet L 2014 Diagrammatic Monte-Carlo study of quasi-two-dimensional Fermi polarons *Phys. Rev. B* **90** 104510
- [55] Kroiss P and Pollet L 2015 Diagrammatic Monte-Carlo study of a mass-imbalanced Fermi-polaron system *Phys. Rev. B* **91** 144507

- [56] Goulko O, Mishchenko A S, Prokof'ev N and Svistunov B 2016 Dark continuum in the spectral function of the resonant Fermi polaron *Phys. Rev. A* **94** 051605
- [57] Schirotzek A, Wu C, Sommer A and Zwierlein M W 2009 Observation of Fermi polarons in a tunable Fermi liquid of ultracold atoms *Phys. Rev. Lett.* **102** 230402
- [58] Zhang Y, Ong W, Arakyan I and Thomas J E 2012 Polaron-to-polaron transitions in the radio-frequency spectrum of a quasi-two-dimensional Fermi gas *Phys. Rev. Lett.* **108** 235302
- [59] Cui X and Zhai H 2010 Stability of a fully magnetized ferromagnetic state in repulsively interacting ultracold Fermi gases *Phys. Rev. A* **81** 041602
- [60] Massignan P and Bruun G M 2011 Repulsive polarons and itinerant ferromagnetism in strongly polarized Fermi gases *Eur. Phys. J. D* **65** 83–9
- [61] Jo G-B, Lee Y-R, Choi J-H, Christensen C A, Kim T H, Thywissen J H, Pritchard D E and Ketterle W 2009 Itinerant ferromagnetism in a Fermi gas of ultracold atoms *Science* **325** 1521–4
- [62] Barth M and Zwerger W 2011 Tan relations in one dimension *Ann. Phys.* **326** 2544–65
- [63] Pekker D, Babadi M, Sensarma R, Zinner N, Pollet L, Zwierlein M W and Demler E 2011 Competition between pairing and Ferromagnetic instabilities in ultracold Fermi gases near Feshbach resonances *Phys. Rev. Lett.* **106** 050402
- [64] Weld D M and Ketterle W 2011 Towards quantum magnetism with ultracold atoms *J. Phys.: Conf. Ser.* 264 012017
- [65] Sanner C, Su E J, Huang W, Keshet A, Gillen J and Ketterle W 2012 Correlations and pair formation in a repulsively interacting Fermi gas *Phys. Rev. Lett.* **108** 240404
- [66] Valtolina G, Scazza F, Amico A, Burchianti A, Recati A, Enss T, Inguscio M, Zaccanti M and Roati G 2017 Exploring the ferromagnetic behaviour of a repulsive Fermi gas through spin dynamics *Nat. Phys.* **13** 704–9
- [67] Kohstall C, Zaccanti M, Jag M, Trenkwalder A, Massignan P, Bruun G M, Schreck F and Grimm R 2012 Metastability and coherence of repulsive polarons in a strongly interacting Fermi mixture *Nature* **485** 615–8
- [68] Koschorreck M, Pertot D, Vogt E, Fröhlich B, Feld M and Köhl M 2012 Attractive and repulsive Fermi polarons in two dimensions *Nature* **485** 619–22
- [69] Ngampruetikorn V, Levinsen J and Parish M M 2012 Repulsive polarons in two-dimensional Fermi gases *Europhys. Lett.* **98** 30005
- [70] Scazza F, Valtolina G, Massignan P, Recati A, Amico A, Burchianti A, Fort C, Inguscio M, Zaccanti M and Roati G 2017 Repulsive Fermi polarons in a resonant mixture of ultracold ^6Li atoms *Phys. Rev. Lett.* **118** 083602
- [71] Cetina M, Jag M, Lous R S, Walraven J T M, Grimm R, Christensen R S and Bruun G M 2015 Decoherence of impurities in a Fermi sea of ultracold atoms *Phys. Rev. Lett.* **115** 135302
- [72] Goold J, Fogarty T, Lo Gullo N, Paternostro M and Busch T 2011 Orthogonality catastrophe as a consequence of qubit embedding in an ultracold Fermi gas *Phys. Rev. A* **84** 063632
- [73] Knap M, Shashi A, Nishida Y, Imambekov A, Abanin D A and Demler E 2012 Time-dependent impurity in ultracold fermions: Orthogonality catastrophe and beyond *Phys. Rev. X* **2** 041020
- [74] Greiner M, Mandel O, Esslinger T, Hansch T W and Bloch I 2002 Quantum phase transition from a superfluid to a Mott insulator in a gas of ultracold atoms *Nature* **415** 39–44
- [75] Lamporesi G, Catani J, Barontini G, Nishida Y, Inguscio M and Minardi F 2010 Scattering in mixed dimensions with ultracold gases *Phys. Rev. Lett.* **104** 153202
- [76] Serwane F, Zürn G, Lompe T, Ottenstein T B, Wenz A N and Jochim S 2011 Deterministic preparation of a tunable few-fermion system *Science* **332** 336–8
- [77] Catani J, Lamporesi G, Naik D, Gring M, Inguscio M, Minardi F, Kantian A and Giamarchi T 2012 Quantum dynamics of impurities in a one-dimensional Bose gas *Phys. Rev. A* **85** 023623
- [78] Wenz A N, Zürn G, Murmann S, Brouzos I, Lompe T and Jochim S 2013 From few to many: observing the formation of a Fermi sea one atom at a time *Science* **342** 457–60
- [79] Fedichev P O, Kagan Y, Shlyapnikov G V and Walraven J T M 1996 Influence of nearly resonant light on the scattering length in low-temperature atomic gases *Phys. Rev. Lett.* **77** 2913–6
- [80] Bohn J L and Julienne P S 1996 Semianalytic treatment of two-color photoassociation spectroscopy and control of cold atoms *Phys. Rev. A* **54** R4637–40
- [81] Bohn J L and Julienne P S 1999 Semianalytic theory of laser-assisted resonant cold collisions *Phys. Rev. A* **60** 414–25
- [82] Friedrich H 2013 *Scattering Theory* vol 872 (New York: Springer)
- [83] Pethick C J and Smith H 2002 *Bose–Einstein Condensation in Dilute Gases* (Cambridge: Cambridge University Press)
- [84] Schmidt R, Rath S P and Zwerger W 2012 Efimov physics beyond universality *Eur. Phys. J. B* **85** 1–6
- [85] Langmack C, Schmidt R and Zwerger W 2017 Efimov states near a Feshbach resonance and the limits of van der Waals universality at finite background scattering length (arXiv:1709.00749)
- [86] Anderson P W 1961 Localized magnetic states in metals *Phys. Rev.* **124** 41–53
- [87] Fano U 1961 Effects of configuration interaction on intensities and phase shifts *Phys. Rev.* **124** 1866–78
- [88] Góral K, Köhler T, Gardiner S A, Tiesinga E and Julienne P S 2004 Adiabatic association of ultracold molecules via magnetic-field tunable interactions *J. Phys. B: At. Mol. Opt. Phys.* **37** 3457
- [89] Szymańska M H, Góral K, Köhler T and Burnett K 2005 Conventional character of the BCS–BEC crossover in ultracold gases of 40 K *Phys. Rev. A* **72** 013610
- [90] Cheuk L W, Sommer A T, Hadzibabic Z, Yefsah T, Bakr W S and Zwierlein M W 2012 Spin-injection spectroscopy of a spin-orbit coupled Fermi gas *Phys. Rev. Lett.* **109** 095302
- [91] Jørgensen N B, Wacker L, Skalmstang K T, Parish M M, Levinsen J, Christensen R S, Bruun G M and Arlt J J 2016 Observation of attractive and repulsive polarons in a Bose-Einstein condensate *Phys. Rev. Lett.* **117** 055302
- [92] Hu M-G, Van de Graaff M J, Kedar D, Corson J P, Cornell E A and Jin D S 2016 Bose polarons in the strongly interacting regime *Phys. Rev. Lett.* **117** 055301
- [93] Camargo F *et al* 2017 Creation of Rydberg polarons in a Bose gas (arXiv:1706.03717)
- [94] Schmidt R *et al* 2017 Theory of excitation of Rydberg polarons in an atomic quantum gas (arXiv:1709.01838)
- [95] Thomas M, Karzig T and Viola Kusminskiy S 2015 Langevin dynamics of a heavy particle and orthogonality effects *Phys. Rev. B* **92** 245404
- [96] Fumi F G 1955 Cxvi. Vacancies in monovalent metals *Lond. Edinburgh Dublin Phil. Mag. J. Sci.* **46** 1007–20
- [97] Schmidt R, Sadeghpour H R and Demler E 2016 Mesoscopic Rydberg impurity in an atomic quantum gas *Phys. Rev. Lett.* **116** 105302
- [98] Veillette M, Moon E G, Lamacraft A, Radzihovsky L, Sachdev S and Sheehy D E 2008 Radio-frequency spectroscopy of a strongly imbalanced Feshbach-resonant Fermi gas *Phys. Rev. A* **78** 033614
- [99] Yi W and Zhang W 2012 Molecule and polaron in a highly polarized two-dimensional Fermi gas with spin-orbit coupling *Phys. Rev. Lett.* **109** 140402
- [100] Levinsen J, Massignan P, Chevy F and Lobo C 2012 *p*-wave polaron *Phys. Rev. Lett.* **109** 075302

- [101] Massignan P 2012 Polarons and dressed molecules near narrow Feshbach resonances *Europhys. Lett.* **98** 10012
- [102] Trefzger C and Castin Y 2013 Energy, decay rate, and effective masses for a moving polaron in a Fermi sea: explicit results in the weakly attractive limit *Europhys. Lett.* **104** 50005
- [103] Trefzger C and Castin Y 2013 Polaron residue and spatial structure in a Fermi gas *Europhys. Lett.* **101** 30006
- [104] Massel F, Kantian A, Daley A J, Giamarchi T and Törmä P 2013 Dynamics of an impurity in a one-dimensional lattice *New J. Phys.* **15** 045018
- [105] Edwards D M 2013 A smooth polaron-molecule crossover in a Fermi system *J. Phys.: Condens. Matter* **25** 425602
- [106] Astrakharchik G E and Brouzos I 2013 Trapped one-dimensional ideal Fermi gas with a single impurity *Phys. Rev. A* **88** 021602
- [107] Knap M, Abanin D A and Demler E 2013 Dissipative dynamics of a driven quantum spin coupled to a bath of ultracold fermions *Phys. Rev. Lett.* **111** 265302
- [108] Vlietinck J, Ryckebusch J and Van Houcke K 2013 Quasiparticle properties of an impurity in a Fermi gas *Phys. Rev. B* **87** 115133
- [109] Doggen E V H and Kinnunen J J 2013 Energy and contact of the one-dimensional Fermi polaron at zero and finite temperature *Phys. Rev. Lett.* **111** 025302
- [110] Massignan P, Yu Z and Bruun G M 2013 Itinerant ferromagnetism in a polarized two-component Fermi gas *Phys. Rev. Lett.* **110** 230401
- [111] Parish M M and Levinsen J 2013 Highly polarized Fermi gases in two dimensions *Phys. Rev. A* **87** 033616
- [112] Kantian A, Schollwöck U and Giamarchi T 2014 Competing regimes of motion of 1d mobile impurities *Phys. Rev. Lett.* **113** 070601
- [113] Trefzger C and Castin Y 2014 Self-energy of an impurity in an ideal Fermi gas to second order in the interaction strength *Phys. Rev. A* **90** 033619
- [114] Bour S, Lee D, Hammer H-W and Mei U-G 2015 *Ab initio* lattice results for Fermi polarons in two dimensions *Phys. Rev. Lett.* **115** 185301
- [115] Christensen R S and Bruun G M 2015 Quasiparticle scattering rate in a strongly polarized Fermi mixture *Phys. Rev. A* **91** 042702
- [116] Chen J-G, Deng T-S, Yi W and Zhang W 2016 Polarons and molecules in a Fermi gas with orbital Feshbach resonance *Phys. Rev. A* **94** 053627
- [117] Roscher D, Braun J and Drut J E 2015 Phase structure of mass- and spin-imbalanced unitary Fermi gases *Phys. Rev. A* **91** 053611
- [118] Lan Z and Lobo C 2015 Excitonic states of an impurity in a Fermi gas *Phys. Rev. A* **92** 053605
- [119] Hu H, Wang A-B, Yi S and Liu X-J 2016 Fermi polaron in a one-dimensional quasiperiodic optical lattice: the simplest many-body localization challenge *Phys. Rev. A* **93** 053601
- [120] Gopalakrishnan S, Parker C V and Demler E 2015 Mobile magnetic impurities in a Fermi superfluid: a route to designer molecules *Phys. Rev. Lett.* **114** 045301
- [121] Duncan C W, Loft N J S, Öhberg P, Zinner N T and Valiente M 2017 Spin localization of a Fermi polaron in a quasirandom optical lattice *Few-Body Syst.* **58** 50
- [122] Mao R, Guan X W and Wu B 2016 Exact results for polaron and molecule in one-dimensional spin-1/2 Fermi gas *Phys. Rev. A* **94** 043645
- [123] Mitchison M T, Johnson T H and Jaksch D 2016 Probing the dynamic structure factor of a neutral Fermi superfluid along the BCS–BEC crossover using atomic impurity qubits *Phys. Rev. A* **94** 063618
- [124] Kain B and Ling H Y 2017 Hartree-Fock treatment of Fermi polarons using the Lee-Low-Pines transformation *Phys. Rev. A* **96** 033627
- [125] De Dominicis C and Martin P C 1964 Stationary entropy principle and renormalization in normal and superfluid systems. II. Diagrammatic formulation *J. Math. Phys.* **5** 31
- [126] Mahan G D 1967 Excitons in metals: infinite hole mass *Phys. Rev.* **163** 612–7
- [127] Yuval G and Anderson P W 1970 Exact results for the Kondo problem: One-body theory and extension to finite temperature *Phys. Rev. B* **1** 1522–8
- [128] Combescot M and Nozières P 1971 Infrared catastrophe and excitons in the x-ray spectra of metals *J. Phys. France* **32** 913–29
- [129] Hentschel M, Ullmo D and Baranger H U 2005 Fermi edge singularities in the mesoscopic regime: Anderson orthogonality catastrophe *Phys. Rev. B* **72** 035310
- [130] Pustilnik M, Khodas M, Kamenev A and Glazman L I 2006 Dynamic response of one-dimensional interacting fermions *Phys. Rev. Lett.* **96** 196405
- [131] Pereira R G, White S R and Affleck I 2008 Exact edge singularities and dynamical correlations in spin-1/2 chains *Phys. Rev. Lett.* **100** 027206
- [132] Pereira R G, White S R and Affleck I 2009 Spectral function of spinless fermions on a one-dimensional lattice *Phys. Rev. B* **79** 165113
- [133] Mkhitarian V V and Raikh M E 2011 Fermi-edge singularity in the vicinity of the resonant scattering condition *Phys. Rev. Lett.* **106** 197003
- [134] Pimenov D, von Delft J, Glazman L and Goldstein M 2017 Fermi-edge exciton-polaritons in doped semiconductor microcavities with finite hole mass (arXiv:1707.08613)
- [135] Ohtaka K and Tanabe Y 1990 Theory of the soft-x-ray edge problem in simple metals: historical survey and recent developments *Rev. Mod. Phys.* **62** 929–91
- [136] Nazarov Y V and Blanter Y M 2009 *Quantum Transport: Introduction to Nanoscience* (Cambridge: Cambridge University Press)
- [137] Rath S P and Schmidt R 2013 Field-theoretical study of the Bose polaron *Phys. Rev. A* **88** 053632
- [138] Li W and Das Sarma S 2014 Variational study of polarons in Bose–Einstein condensates *Phys. Rev. A* **90** 013618
- [139] Kain B and Ling H Y 2014 Polarons in a dipolar condensate *Phys. Rev. A* **89** 023612
- [140] Yi W and Cui X 2015 Polarons in ultracold Fermi superfluids *Phys. Rev. A* **92** 013620
- [141] Schmidt R and Leshchko M 2015 Rotation of quantum impurities in the presence of a many-body environment *Phys. Rev. Lett.* **114** 203001
- [142] Levinsen J, Parish M M and Bruun G M 2015 Impurity in a Bose–Einstein condensate and the Efimov effect *Phys. Rev. Lett.* **115** 125302
- [143] Christensen R S, Levinsen J and Bruun G M 2015 Quasiparticle properties of a mobile impurity in a Bose–Einstein condensate *Phys. Rev. Lett.* **115** 160401
- [144] Dehkharghani A S, Volosniev A G and Zinner N T 2015 Quantum impurity in a one-dimensional trapped Bose gas *Phys. Rev. A* **92** 031601
- [145] Volosniev A G, Hammer H-W and Zinner N T 2015 Real-time dynamics of an impurity in an ideal Bose gas in a trap *Phys. Rev. A* **92** 023623
- [146] Ardila L A P N and Giorgini S 2015 Impurity in a Bose–Einstein condensate: study of the attractive and repulsive

- branch using quantum Monte-Carlo methods *Phys. Rev. A* **92** 033612
- [147] Shchadilova Y E, Schmidt R, Grusdt F and Demler E 2016 Quantum dynamics of ultracold Bose polarons *Phys. Rev. Lett.* **117** 113002
- [148] Schmidt R and Leshchko M 2016 Deformation of a quantum many-particle system by a rotating impurity *Phys. Rev. X* **6** 011012
- [149] Ardila L A P N and Giorgini S 2016 Bose polaron problem: effect of mass imbalance on binding energy *Phys. Rev. A* **94** 063640
- [150] Kain B and Ling H Y 2016 Generalized Hartree–Fock–Bogoliubov description of the Fröhlich polaron *Phys. Rev. A* **94** 013621
- [151] Ashida Y, Schmidt R, Tarruell L and Demler E 2017 Many-body interferometry of magnetic polaron dynamics (arXiv:1701.01454)
- [152] Sun M, Zhai H and Cui X 2017 Visualizing the Efimov correlation in Bose polarons *Phys. Rev. Lett.* **119** 013401
- [153] Kittel C 1966 *Introduction to Solid State* (New York: Wiley)
- [154] Martin T and Landauer R 1992 Wave-packet approach to noise in multichannel mesoscopic systems *Phys. Rev. B* **45** 1742–55
- [155] Braunecker B 2006 Response of a Fermi gas to time-dependent perturbations: Riemann–Hilbert approach at nonzero temperatures *Phys. Rev. B* **73** 075122
- [156] Gutman D B, Gefen Y and Mirlin A D 2011 Non-equilibrium 1d many-body problems and asymptotic properties of Toeplitz determinants *J. Phys. A: Math. Theor.* **44** 165003
- [157] Ivanov D A and Levkivskiy I P 2016 Fermionic full counting statistics with smooth boundaries: from discrete particles to bosonization *Europhys. Lett.* **113** 17009
- [158] Yeramian E and Claverie P 1987 Analysis of multiexponential functions without a hypothesis as to the number of components *Nature* **326** 169–74
- [159] Wern H, Barth P, Folkerts K H, Staemmler M and Gersonde K 1989 A new hybrid method for analysis of multiexponential T2 relaxation processes in NMR images *Proc. of the Int. Symp. CAR* vol 89
- [160] Kondo J and Soda T 1983 Theory of ion mobility in liquid ^3He *J. Low Temp. Phys.* **50** 21–32
- [161] Szegő G 1952 On certain hermitian forms associated with the fourier series of a positive function *Commun. Sém. Math. Univ. Lund* **1952** 228–38
- [162] Basor E L and Tracy C A 1991 The Fisher–Hartwig conjecture and generalizations *Physica A* **177** 167–73
- [163] Gray R M 2006 *Toeplitz and Circulant Matrices: a review* (Bostson, MA: Now Publishers Inc) (<https://doi.org/10.1561/01000000006>)
- [164] Hassler F, Suslov M V, Graf G M, Lebedev M V, Lesovik G B and Blatter G 2008 Wave-packet formalism of full counting statistics *Phys. Rev. B* **78** 165330
- [165] Hassler F 2009 Wave-packet approach to full counting statistics *PhD Thesis, Dissertation* Eidgenössische Technische Hochschule ETH Zürich, Nr. 18218
- [166] Fisher M E 2007 *Hartwig Toeplitz Determinants R E, Theorems, Conjectures* (New York: Wiley) pp 333–53
- [167] Deift P, Its A and Krasovsky I 2011 Asymptotics of Toeplitz, Hankel, and Toeplitz + Hankel determinants with Fisher–Hartwig singularities *Ann. Math.* **174** 1243–99
- [168] Bartenstein M, Altmeyer A, Riedl S, Jochim S, Chin C, Denschlag J H and Grimm R 2004 Crossover from a molecular Bose–Einstein condensate to a degenerate Fermi gas *Phys. Rev. Lett.* **92** 120401
- [169] Yu Z and Baym G 2006 Spin-correlation functions in ultracold paired atomic-fermion systems: sum rules, self-consistent approximations, and mean fields *Phys. Rev. A* **73** 063601
- [170] Baym G, Pethick C J, Yu Z and Zwierlein M W 2007 Coherence and clock shifts in ultracold Fermi gases with resonant interactions *Phys. Rev. Lett.* **99** 190407
- [171] Punk M and Zwerger W 2007 Theory of rf-spectroscopy of strongly interacting fermions *Phys. Rev. Lett.* **99** 170404
- [172] Braaten E, Kang D and Platter L 2008 Universal relations for a strongly interacting Fermi gas near a Feshbach resonance *Phys. Rev. A* **78** 053606
- [173] Valiente M, Zinner N T and Mølmer K 2011 Universal relations for the two-dimensional spin-1/2 Fermi gas with contact interactions *Phys. Rev. A* **84** 063626
- [174] Valiente M 2012 Tan’s distributions and Fermi–Huang pseudopotential in momentum space *Phys. Rev. A* **85** 014701
- [175] Langmack C, Barth M, Zwerger W and Braaten E 2012 Clock shift in a strongly interacting two-dimensional Fermi gas *Phys. Rev. Lett.* **108** 060402
- [176] Hofmann J, Barth M and Zwerger W 2013 Short-distance properties of Coulomb systems *Phys. Rev. B* **87** 235125
- [177] Lifshitz E, Pitaevskii L and Berestetskii B 1980 *Course of theoretical physics Statistical Physics* vol 5 (Oxford: Pergamon)
- [178] Fletcher R J, Lopes R, Man J, Navon N, Smith R P, Zwierlein M W and Hadzibabic Z 2017 Two- and three-body contacts in the unitary Bose gas *Science* **355** 377–80
- [179] Sols F and Guinea F 1987 Bulk and surface diffusion of heavy particles in metals: a path-integral approach *Phys. Rev. B* **36** 7775–85
- [180] Prokof’ev N 1993 Diffusion of a heavy particle in a Fermi-liquid theory *Int. J. Mod. Phys. B* **7** 3327–51
- [181] Rosch A and Kopp T 1995 Heavy particle in a d -dimensional fermionic bath: a strong coupling approach *Phys. Rev. Lett.* **75** 1988–91
- [182] Jeblick M, Mitrouskas D, Petrat S and Pickl P 2017 Free time evolution of a tracer particle coupled to a Fermi gas in the high-density limit *Commun. Math. Phys.* **356** 143–87
- [183] Scazza F, Hofrichter C, Hofer M, De Groot P C, Bloch I and Fölling S 2014 Observation of two-orbital spin-exchange interactions with ultracold SU(N)-symmetric fermions *Nat. Phys.* **10** 779–84
- [184] Höfer M, Riegger L, Scazza F, Hofrichter C, Fernandes D R, Parish M M, Levinsen J, Bloch I and Fölling S 2015 Observation of an orbital interaction-induced Feshbach resonance in ^{173}Yb *Phys. Rev. Lett.* **115** 265302
- [185] Mathy C J M, Zvonarev M B and Demler E 2012 Quantum flutter of supersonic particles in one-dimensional quantum liquids *Nat. Phys.* **8** 881–6
- [186] Knap M, Mathy C J, Ganahl M, Zvonarev M B and Demler E 2014 Quantum flutter: signatures and robustness *Phys. Rev. Lett.* **112** 015302
- [187] Gamayun O, Pronko A G and Zvonarev M B 2015 Impurity Green’s function of a one-dimensional Fermi gas *Nucl. Phys. B* **892** 83–104
- [188] Gamayun O, Pronko A G and Zvonarev M B 2016 Time and temperature-dependent correlation function of an impurity in one-dimensional Fermi and Tonks–Girardeau gases as a Fredholm determinant *New J. Phys.* **18** 045005
- [189] Meinert F, Knap M, Kirilov E, Jag-Lauber K, Zvonarev M B, Demler E and Nägerl H-C 2017 Bloch oscillations in the absence of a lattice *Science* **356** 945–8
- [190] Gamayun O, Lychkovskiy O, Burovski E, Malcomson M, Cheianov V V and Zvonarev M B 2017 Quench-controlled frictionless motion of an impurity in a quantum medium (arXiv:1708.07665)
- [191] Kitagawa T, Berg E, Rudner M and Demler E 2010 Topological characterization of periodically

- driven quantum systems *Phys. Rev. B* **82** 235114
- [192] Rechtsman M C, Zeuner J M, Plotnik Y, Lumer Y, Podolsky D, Dreisow F, Nolte S, Segev M and Szameit A 2013 Photonic floquet topological insulators *Nature* **496** 196–200
- [193] Knap M, Babadi M, Refael G, Martin I and Demler E 2016 Dynamical cooper pairing in nonequilibrium electron-phonon systems *Phys. Rev. B* **94** 214504
- [194] Bordia P, Luschen H, Schneider U, Knap M and Bloch I 2017 Periodically driving a many-body localized quantum system *Nat. Phys.* **13** 460–4
- [195] Weidinger S A and Knap M 2017 Floquet prethermalization and regimes of heating in a periodically driven, interacting quantum system *Sci. Rep.* **7** 45382
- [196] Orenstein J 2012 Ultrafast spectroscopy of quantum materials *Phys. Today* **65** 44–50
- [197] Fausti D, Tobey R I, Dean N, Kaiser S, Dienst A, Hoffmann M C, Pyon S, Takayama T, Takagi H and Cavalleri A 2011 Light-induced superconductivity in a stripe-ordered cuprate *Science* **331** 189–91
- [198] Polkovnikov A, Sengupta K, Silva A and Vengalattore M 2011 Colloquium: nonequilibrium dynamics of closed interacting quantum systems *Rev. Mod. Phys.* **83** 863–83



Richard Schmidt received his PhD in 2013 from the Technical University in Munich, Germany, working in the group of Prof. Wilhelm Zwerger on the study of the interplay of few- and many-body physics in ultracold atomic systems. As recipient of the independent ITAMP Postdoctoral Fellowship he then moved to Harvard University and the Harvard-Smithsonian Center for Astrophysics in Cambridge, USA. There, he made various contributions to the research on quantum impurity problems far from equilibrium, ranging from Rydberg excitations in Bose gases, to the impurity-induced dephasing dynamics of fermionic systems, and the description of quantum rotors coupled to a many-body environment, such as relevant for molecules immersed in superfluid Helium nanodroplets. Since October 2017 he is working at ETH Zürich, Switzerland, where he continues to study the theory of mesoscopic systems at the boundary from few- and many-body physics.